



DISSERTAÇÃO DE MESTRADO EM ENGENHARIA ELÉTRICA

**Reconfigurable Metasurface Antenna Array
Using Holographic Beamforming**

Matheus Pereira Santana

Brasília, março de 2021

UNIVERSIDADE DE BRASÍLIA

FACULDADE DE TECNOLOGIA

UNIVERSIDADE DE BRASÍLIA
Faculdade de Tecnologia

DISSERTAÇÃO DE MESTRADO EM ENGENHARIA ELÉTRICA

**Reconfigurable Metasurface Antenna Array
Using Holographic Beamforming**

Matheus Pereira Santana

*Dissertação de Mestrado em Engenharia Elétrica submetida ao Departamento de Engenharia
Elétrica como requisito parcial para obtenção
do grau de Mestre em Engenharia Elétrica*

Banca Examinadora

Sébastien Roland Marie Joseph Rondineau, D.Sc., _____
FT/UnB
Orientador

Daniel Costa Araújo, D.Sc., FGA/UnB _____
Examinador Interno

Leonardo Aguayo, D.Sc., FT/UnB _____
Examinador interno

Marcos Tavares de Melo, D.Sc., CTG/DES/UFPE _____
Examinador externo

PUBLICAÇÃO: PPGENE.DM - 766/21
BRASÍLIA/DF: MARÇO - 2021

FICHA CATALOGRÁFICA

SANTANA, MATHEUS PEREIRA

Reconfigurable Metasurface Antenna Array Using Holographic Beamforming [Distrito Federal] 2021. xvi, 107 p., 210 x 297 mm (ENE/FT/UnB, Mestre, Engenharia Elétrica, 2021).

Dissertação de Mestrado em Engenharia Elétrica - Universidade de Brasília, Faculdade de Tecnologia.

Departamento de Engenharia Elétrica

1. Holographic Beamforming

2. Reconfigurable Radiation Pattern

3. Antenna Array

4. Metasurface Antenna

5. PIN diode switch

6. Convex Optimization

I. ENE/FT/UnB

II. Título (série)

BIBLIOGRAPHY

SANTANA, M. P. (2021). *Reconfigurable Metasurface Antenna Array Using Holographic Beamforming*. Dissertação de Mestrado em Engenharia Elétrica, Publicação PPGENE.DM - 766/21, Departamento de Engenharia Elétrica, Universidade de Brasília, Brasília, DF, 107 p.

CESSÃO DE DIREITOS

AUTOR: Matheus Pereira Santana

TÍTULO: Reconfigurable Metasurface Antenna Array Using Holographic Beamforming .

GRAU: Mestre em Engenharia Elétrica ANO: 2021

É concedida à Universidade de Brasília permissão para reproduzir cópias desta Dissertação de Mestrado em Engenharia Elétrica e para emprestar ou vender tais cópias somente para propósitos acadêmicos e científicos. Os autores reservam outros direitos de publicação e nenhuma parte dessa Dissertação de Mestrado em Engenharia Elétrica pode ser reproduzida sem autorização por escrito dos autores.

Matheus Pereira Santana

Depto. de Engenharia Elétrica (ENE) - FT

Universidade de Brasília (UnB)

Campus Darcy Ribeiro

CEP 70919-970 - Brasília - DF - Brasil

Dedico este trabalho a minha família.

AGRADECIMENTOS

Deixo meus agradecimentos...

...ao professor Sébastien, por ter me direcionado na execução deste trabalho e por ser meu mestre no estudo das microondas por tantos anos.

...ao professor Daniel Araújo, por compartilhar seu conhecimento e contribuir para essa dissertação.

...aos colegas do laboratório de telecomunicações da UnB, pelos trabalhos e estudos executados em parceria.

...aos meus avôs, tios e primos, por terem me ajudado nessa jornada a todo instante.

...a minha parceira, Ana Clara, pela companhia e carinho.

...a minha mãe, Érica, que me ensinou a lutar pelos meus objetivos.

Muito obrigado!

ABSTRACT

This work describes the problem of beam-forming using the holographic technique in metasurface antenna arrays at Ku-band. A model of this antenna array is presented. The scattering elements in the metasurface are slot dipole antennas. These elements are placed above a dielectric cavity created using a Parallel-Plate Waveguide (PPW). The metasurface antenna array is proposed to be a reconfigurable antenna array, where its reconfigurability is provided varying the bias state of PIN diodes attached in the metasurface cells.

Due to the PIN diode, an additional bias circuit must be added, which includes some through-hole vias and other details that create complex structures. This detail does not permit the use of common analytical methods and simplifications to compute the hologram. Due to this, in this work, a CAD model is drawn and simulated in full-wave software. The electromagnetic fields are then retrieved at this model and so used to calculate the hologram. This approach allows the implementation of this technique in any type of cavity underneath any type of metasurface.

To verify the procedure, a hologram and its respective array factor are presented. Furthermore, a convex optimization method is presented to enhance the performance of the antenna, reducing the sidelobe level.

Keywords: Antenna array, metasurface antennas, reconfigurable antennas, holographic beam-forming, convex optimization.

RESUMO

Este trabalho trata o problema de formação de feixe usando técnicas de holografia em arranjos de antena sobre meta-superfícies na banda Ku. Um modelo da antena proposta é apresentado. Os elementos irradiantes usados na meta-superfície são antenas dipolo do tipo fenda. Esses elementos são posicionados acima da cavidade dielétrica criada usando-se uma guia de onda de placas paralelas. A antena é concebida para ser reconfigurável, aonde sua reconfigurabilidade é feita variando-se o a polarização de diodos PIN incorporados no desenho da célula da meta-superfície.

Devido a presença do diodo PIN, um circuito de polarização adicional precisou ser adicionado na antena, o qual inclui alguns vias passantes e outros detalhes que criam uma estrutura complexa. Este detalhe não permite que modelos analíticos genéricos e outras simplificações sejam usadas

para calcular o holograma. Por este motivo, este trabalho usa os resultados da simulação eletromagnética de um modelo CAD da antena proposta. Os campos eletromagnéticos resultantes são então extraídos desse modelo e usados para se calcular o holograma. Essa abordagem permite a implementação dessa técnica para diferentes tipos de cavidade abaixo da meta-superfície.

Para validar o procedimento, um holograma e seu respectivo diagrama de radiação são apresentados. Além do mais, uma otimização convexa é apresentada para melhorar a performance da antena, reduzindo o nível dos lóbulos secundários.

Palavras-chave: Arranjo de antenas, antenas de meta-superfície, formador de feixe holográfico, otimização convexa.

TABLE OF CONTENTS

1	INTRODUÇÃO	1
1.1	CONTEXTUALIZAÇÃO	1
1.2	OBJETIVOS DO TRABALHO	2
1.3	ORGANIZAÇÃO DA DISSERTAÇÃO	2
1.4	CONTRIBUIÇÕES	3
2	INTRODUCTION	4
2.1	PREFACE	4
2.2	OBJECTIVES	5
2.3	ORGANIZATION OF THIS DISSERTATION	5
2.4	CONTRIBUTIONS	5
3	FUNDAMENTAL CONCEPTS	7
3.1	ANTENNA CELLS AND ARRAYS	7
3.1.1	ANTENNAS	7
3.1.2	RADIATION PATTERN	7
3.1.3	RADIATED POWER, RADIATION DENSITY, AND RADIATION INTENSITY	8
3.1.4	DIRECTIVITY AND GAIN	9
3.1.5	POLARIZATION	9
3.1.6	ANTENNA ARRAY	10
3.2	SLOT ANTENNAS	12
3.2.1	SLOT DIPOLE ANTENNA	12
3.3	SLOT ANTENNA ARRAY	14
3.4	HOLOGRAPHY	15
3.4.1	THE HOLOGRAPHIC PROCEDURE	15
3.4.2	DESCRIBING HOLOGRAPHY MATHEMATICALLY	16
3.5	SPATIAL BEAMFORMING	21
3.5.1	BEAMFORMING ARCHITECTURES	21
3.6	PIN DIODE	24
3.6.1	PIN DIODE STRUCTURE AND EQUIVALENT MODELS	24
3.6.2	PIN DIODE AS A SWITCH	25
3.7	METASURFACE ANTENNAS	30
3.7.1	EXAMPLES OF COMMERCIAL METASURFACES ANTENNAS	30
3.7.2	DEVELOPING OF METASURFACES ANTENNAS	31
3.8	CONVEX OPTIMIZATION	33
3.8.1	CONVEX OPTIMIZATION BACKGROUND	33
3.8.2	PROBLEM TO BE OPTIMIZED	33

3.9	COUPLED OPEN-LOOP RESONATOR FILTERS	36
3.9.1	COUPLED OPEN-LOOP RESONATOR CELLS	36
3.9.2	COUPLED OPEN-LOOP RESONATOR BAND-PASS FILTER	37
4	DESIGN OF HOLOGRAPHIC METASURFACE ANTENNA	39
4.1	METASURFACE ANTENNA STRUCTURE	39
4.2	HOLOGRAPHIC METASURFACE ANTENNA	39
4.3	HOLOGRAM RECORDING PROCEDURE FOR ARBITRARY GUIDED-MODES	41
4.4	PROPOSED METASURFACE ANTENNA	42
4.4.1	ANTENNA CAVITY	42
4.4.2	COAXIAL MONOPOLE LAUNCHER	42
4.4.3	ANTENNA ELEMENT	43
4.4.4	PIN DIODE BEHAVIOR	45
4.4.5	SPIRAL MICROSTRIP INDUCTOR	46
4.4.6	ANTENNA ARRAY	47
4.4.7	HOLOGRAM GENERATION	48
4.4.8	CONTROL CIRCUIT	49
4.4.9	POWER SUPPLY	53
4.5	COUPLED OPEN-LOOP RESONATOR BAND-PASS FILTER	55
5	IMPLEMENTATION OF HOLOGRAPHY PROCEDURE AND OPTIMIZATION ROUTINES	57
5.1	HOLOGRAPHY PROCEDURE VERIFICATION	57
5.1.1	MULTI-BEAM CAPABILITY	67
5.2	OPTIMIZATION VERIFICATION	68
6	CONCLUSIONS AND FUTURE WORK	73
6.1	FUTURE WORK	73
	BIBLIOGRAPHY	76
	APPENDICES	84
I	16-BIT CONSTANT CURRENT LED SINK DRIVER - CONTROL CIRCUIT	85
I.1	CIRCUITS SCHEMATICS	85
I.2	PCB LAYOUT	88
I.3	CIRCUIT 3D VIEWS	91
II	POWER SUPPLY BOARD	93
II.1	CIRCUITS SCHEMATICS	93
II.2	PCB LAYOUT	95
II.3	CIRCUIT 3D VIEWS	98
III	MATLAB CODES	100

III.1 HOLOGRAPHIC PROCEDURE.....	100
III.2 CONVEX OPTIMIZATION METHOD	103

LIST OF FIGURES

3.1	Representation of a radiation pattern example with its most important definitions drawn.	8
3.2	Excitation of classical dipole and slot dipole antennas. The feed signal is introduced along the length of the classical dipole, and along the width of the slot dipole antenna.	12
3.3	Different views of the same hologram varying the position of observation from the (a) left to the (c) right side, due to the parallax effect.	15
3.4	(a) Experimental setup to perform the holography experiment. (b) Exemplification of the recording process.	16
3.5	Reconstruction holographic process is portrayed where the reference wave impinges in the hologram creating the true image, u_1 , the transmitted reference wave, u_0 and the conjugate image, u_{-1}	17
3.6	Comparison between holographic beam former, phased array and MIMO.	23
3.7	Physical structure of a PIN diode.	24
3.8	PIN diode equivalent models for the forward and reverse bias. In the equivalent models, L_s is the parasitic inductance of the PIN diode package, R_s is series resistance, C_T is the total capacitance and R_p is the parallel resistance when reverse biased.	25
3.9	Magnitude of the complex impedance of the (3.46), (3.47) and (3.48). For these curves were used $R_s = 8 \Omega$, $R_p = 50 k\Omega$, $L_s = 30 \text{ pH}$, $C_T = 0.03 \text{ pF}$ and $Z_0 = 50 \Omega$	26
3.10	PIN diode bias circuit. V_A and V_C are the anode and cathode bias voltages, L_{RF} is the RF choke inductance, C_{DC} is the DC block capacitor and Z_0 is the characteristic impedance of the connected transmission line.	27
3.11	Curve of isolation and insertion loss value of the PIN diode for $R_s = 8 \Omega$, $C_T = 0.03 \text{ pF}$ and $Z_0 = 50 \Omega$	27
3.12	Curve of insertion loss of the forward biased PIN diode for a $C_T = 0.03 \text{ pF}$, $Z_0 = 50 \Omega$ and $f = 12 \text{ GHz}$	28
3.13	Curve of isolation of the reverse biased PIN diode for $R_s = 8 \Omega$, $Z_0 = 50 \Omega$ and $f = 12 \text{ GHz}$	28
3.14	Basic square open-loop resonator microstrip cell. In this cell w is the width of the microstrip line, l is the length of the square side, and g is the gap of the open-loop.	36
3.15	Different coupling mechanisms for different arrangement of square open-loop resonators. (a) Magnetic coupling. (b) Electric coupling. (c) Mixed coupling - Type 1. (d) Mixed coupling - Type 2.	37
3.16	Coupled Open-Loop Resonator Band-Pass Filter arrangement.	38

4.1	Basic structure of a Metasurface Antenna. The main elements of this structure are the antenna cell, the guided propagating medium, the electromagnetic source and a control element. The source illuminates the medium and each antenna scatter to the space a different contribution of this wave, according with its position and the state of the control element.....	39
4.2	Example of how to use the holographic technique in an antenna array. The recording process is performed using the electromagnetic modes created in the cavity by the source (In this case, a coaxial monopole) and the projection of the desired beam over the array. The generated interference pattern is used to change the resonant state of the antennas. The reconstruction process occurs when the reference wave scatters in the recorded hologram in the antenna array.....	40
4.3	Hologram recording over the antenna array. In the example a 15×15 rectangular lattice is used with an arbitrary interference pattern. (a) Interference pattern over the antenna array. (b) Projection of the interference pattern in the array. (c) Recorded hologram in the antenna array.....	41
4.4	S_{11} parameter at the input of the coaxial connector.	43
4.5	Top view of the active slot dipole antenna cell. The PIN diode works like a ON-OFF switch, changing the effective length of the slot. The capacitor acts like DC blocks to isolate the bias signal in the pads.	44
4.6	Side view of the active slot dipole antenna cell. The dielectric number 1 is the medium where the microwave signal propagates and the number 2 is dedicated to draw the bias circuit. The bias through-hole via is used to lead the bias signal from the bottom to the top layer.....	44
4.7	Bottom view of the active slot dipole antenna cell. The bias through-hole via is connected to the octagonal spiral microstrip line inductor.....	45
4.8	PIN diode equivalent slot lengths for both reverse and forward bias state. During the reverse bias state the PIN diode does not create a low path impedance to the surface current, due to this the effective length of the slot is approximately $\lambda_g/2.5$, and then the radiation of the slot is maximized. During the forward bias state the PIN diode conducts the surface current, and then the effective length of the slot downs to $\lambda_g/5$, details that decrease its radiation efficiency	46
4.9	Octagonal spiral microstrip inductor proposed as RF choke.....	47
4.10	Isometric view of the metasurface antenna array.....	48
4.11	16-bit constant current LED sink driver - STP16CPC26 pinout.	50
4.12	Constant current sink drivers connected in Daisy chain configuration.	51
4.13	Current control in Daisy chain configuration.	51
4.14	MA4GP907 PIN diode bias circuit S-parameters simulation in ADS.	51
4.15	MA4GP907 PIN diode switching behavior due to drive voltage sweep. In this figure, it is possible to distinguish the ON and OFF state in S-parameters curves....	52
4.16	Power source map.	54
4.17	Buck converter.....	54

4.18	Final design of the proposed COLF BPF (a) COLR BPF design and its respective area. (b) Photograph of the manufactured COLR BPF.	55
4.19	Comparison between the simulated and measured S-parameter curves of the proposed COLR BPF.....	56
5.1	Hankel function of zeroth order and first kind (a) Magnitude (b) Phase.	58
5.2	Phase of the far-field source projection over the aperture - $(\theta, \varphi) = (20^\circ, 60^\circ)$	59
5.3	Phase of each element in the aperture using the array factor equation - $(\theta, \varphi) = (20^\circ, 60^\circ)$	59
5.4	The phase interference pattern (a) Approach 1 (b) Approach 2 - $(\theta, \varphi, \xi) = (20^\circ, 60^\circ, 50^\circ)$	60
5.5	(a) Phase threshold mask applied over the phase interference pattern created by the 1 st approach. The pixels in black color are the positions where the phase interference is greater than the phase threshold. (b) Hologram - $(\theta, \varphi, \xi) = (20^\circ, 60^\circ, 50^\circ)$	60
5.6	(a) Phase threshold mask applied over the phase interference pattern created by the 2 nd approach. The pixels in black color are the positions where the phase interference is greater than the phase threshold. (b) Hologram - $(\theta, \varphi, \xi) = (20^\circ, 60^\circ, 50^\circ)$	61
5.7	Array factor in sine space - $(\theta, \varphi, \xi) = (20^\circ, 60^\circ, 50^\circ)$	61
5.8	Array factor created by the holograms of the 1 st and 2 nd approaches in sine space - $(\theta, \varphi, \xi) = (20^\circ, 60^\circ, 50^\circ)$	62
5.9	Array factor - $(\theta, \varphi, \xi) = (20^\circ, 60^\circ, 50^\circ)$	62
5.10	Array factor created by the holograms of the 1 st and 2 nd approaches - $(\theta, \varphi, \xi) = (20^\circ, 60^\circ, 50^\circ)$	63
5.11	Phase threshold variation for the first approach: (a) Hologram - $(\theta, \varphi, \xi) = (20^\circ, 60^\circ, 10^\circ)$. (b) Array factor - $(\theta, \varphi, \xi) = (20^\circ, 60^\circ, 10^\circ)$. (c) Hologram - $(\theta, \varphi, \xi) = (20^\circ, 60^\circ, 90^\circ)$. (d) Array factor - $(\theta, \varphi, \xi) = (20^\circ, 60^\circ, 90^\circ)$. (e) Hologram - $(\theta, \varphi, \xi) = (20^\circ, 60^\circ, 180^\circ)$. (f) Array factor - $(\theta, \varphi, \xi) = (20^\circ, 60^\circ, 180^\circ)$	64
5.12	Phase threshold variation for the first approach: (a) Hologram - $(\theta, \varphi, \xi) = (20^\circ, 60^\circ, 10^\circ)$. (b) $(\theta, \varphi, \xi) = (20^\circ, 60^\circ, 10^\circ)$. (c) Hologram - $(\theta, \varphi, \xi) = (20^\circ, 60^\circ, 90^\circ)$. (d) Radiation pattern - $(\theta, \varphi, \xi) = (20^\circ, 60^\circ, 90^\circ)$. (e) Hologram - $(\theta, \varphi, \xi) = (20^\circ, 60^\circ, 180^\circ)$. (f) Radiation pattern - $(\theta, \varphi, \xi) = (20^\circ, 60^\circ, 180^\circ)$	65
5.13	Number of antennas tuned to ON state for different values of phase threshold for both 1 st and 2 nd approaches.	66
5.14	Array factor gain for different values of phase threshold for both 1 st and 2 nd approaches.....	66
5.15	Error between the achieved and desired array factor for different values of phase threshold for both 1 st and 2 nd approaches.	67
5.16	Phase distribution in the aperture used to create the multi-beam radiation pattern (a) $(\theta, \varphi) = (25^\circ, 60^\circ)$. (b) $(\theta, \varphi) = (35^\circ, 170^\circ)$. (c) $(\theta, \varphi) = (15^\circ, 280^\circ)$	68

5.17	Holograms used to create the multi-beam radiation pattern (a) $(\theta, \varphi) = (25^\circ, 60^\circ)$. (b) $(\theta, \varphi) = (35^\circ, 170^\circ)$. (c) $(\theta, \varphi) = (15^\circ, 280^\circ)$. (d) Summation of all holograms.	69
5.18	Array factor of the multi-beam hologram in sine space (a) Ideal array factor. (b) Real array factor.	70
5.19	Array factor of the multi-beam hologram (a) Ideal array factor. (b) Real array factor.	70
5.20	Array factor after the convex optimization process of a beam in $(\theta, \varphi) = (30^\circ, 90^\circ)$ (a) Ideal array factor. (b) Array factor from the holographic procedure. (c) Array factor from the optimization process. (d) Array factor after rounding the optimization mask.	71
5.21	Array factor after the convex optimization process of a beam in $(\theta, \varphi) = (30^\circ, 90^\circ)$ in sine space (a) Ideal array factor. (b) Array factor from the holographic procedure. (c) Array factor from the optimization process. (d) Array factor after rounding the optimization mask.	72
6.1	Top view of the active cross-slot dipole antenna cell. The PIN diode works like a ON-OFF switch, changing the effective length of the slot. The capacitor acts like DC blocks to isolate the bias signal in the pads.	74
6.2	Representation of electric path of the four states of the cross slot dipole antenna (a) Off state. (b) Vertical polarization. (c) Horizontal polarization. (d) Circular polarization.	75
I.1	16-bit constant current LED sink driver control circuit 3D top view.	91
I.2	16-bit constant current LED sink driver control circuit 3D bottom view.	92
II.1	16-bit constant current LED sink driver control circuit 3D top view.	98
II.2	16-bit constant current LED sink driver control circuit 3D bottom view.	99

LIST OF TABLES

4.1	Commercial PIN diodes at the desired frequency.....	46
4.2	Antenna PCB's Layer Stack.	47
4.3	MA4GP907 PIN diode technical specifications.....	50
4.4	ADS PIN diode model.....	52
4.5	Load map.	53
5.1	Design Parameters.....	57

LIST OF SYMBOLS

Latin Symbols

$AF(\theta, \varphi)$	Array factor	
a_{mn}	Antenna excitation amplitude	
A_{mn}	Antenna excitation signal	
C_{DC}	DC block capacitor	[pF]
C_T	Total capacitance junction of the PIN diode	[pF]
d	Radius distance from the antenna	[m]
$D(\theta, \varphi)$	Antenna directivity	
D_f	Desired radiation pattern	
d_x	Inter-spacing in x-axis	[m]
d_y	Inter-spacing in y-axis	[m]
$\vec{e}(\theta, \varphi)$	elementar antenna radiation pattern	
$\vec{E}(\theta, \varphi)$	Radiation pattern	
\vec{E}_a	Aperture electric field	
\vec{E}_{rad}	Electric radiation field	
\vec{H}_a	Aperture magnetic field	
\vec{H}_{rad}	Magnetic radiation field	
H	Cavity phase	[°]
f	frequency	[GHz]
\vec{F}	Radiation vector	
$G(\theta, \varphi)$	Antenna gain	
I_0	Dipole excitation current	[A]
I	Interference pattern	
\vec{J}	Current density	
k	wave number	[rad/m]
L_{RF}	RF choke inductor	[nH]
L_s	Parasitic inductance of the PIN diode	[nH]
O	Object wave	
P_{rad}	Radiated power	[W]
P_{in}	Input power at the antenna	[W]
\hat{r}	Radial component in sphericla coordinate	
R	Reference wave	
R_s	Series resistance of the PIN diode	[Ω]
R_p	Parallel resistance of the PIN diode	[Ω]
$S(\theta, \varphi)$	Radiated power density	[W/m ²]
S_{11}	Input impedance matching	[dB]
T	Transmitted beam over the hologram	
$U(\theta, \varphi)$	Radiation intensity	[W/sr]
u	u component in sine-space	
v	v component in sine-space	
V	Visibility of the hologram	
V_A	Anode bias voltage	[V]
V_C	Cathode bias voltage	[V]
Z	Impedance	[Ω]

Greek Symbols

ϵ_L	Antenna efficiency	
Γ	Reflection Coefficient	
θ	Polar or elevation angle	[°]
φ	Azimuth angle	[°]
ρ_{mn}	Vector position of antenna in the array	[m]
η	Intrinsic impedance of the medium	[Ω]
Φ	Wave phase	[°]
Ψ	Wave phase	[°]
ω	Angular frequency	[rad/s]
λ	Wave-length	[m]
μ	Magnetic permeability	[H/m]
ϵ_r	Electric permissivity	[F/m]

Subscribed

$\hat{0}$	Pointing direction
s	Surface
a	Aperture area

Superscripts

$\hat{}$	Unit base vector
\rightarrow	Vector index

Acronyms

ADC	Analog-to-Digital Converter
AESA	Active Electronically Scanned Array
BPF	Band-Pass Filter
BFN	Beam Forming Network
CDMA	Code Division Multiple Access
COLR	Coupled Open-Loop Resonator
COTS	Commercial of The Shelf
CSDA	Cross-Slot Dipole Antenna
C-SWaP	Cost, Size, Weight and Power
DAC	Digital-to-Analog Converter
DBF	Digital Beam Former
DSP	Digital Signal Processor
ESAA	Electronically Scanned Antenna Array
FDMA	Frequency Division Multiple Access
FEM	Finite Element Method
FR-4	Flame Retardant Epoxy Resin 4
FNBW	First-Null Beamwidth
HBF	Holographic Beam Forming
HPBW	Half-Power Beamwidth
IBC	Impedance Boundary Condition
IL	Insertion Loss
LC	Inductor and Capacitor Circuit
LCD	Liquid Crystal Display
LDO	Low-Dropout Regulator
MIMO	Multiple-Input Multiple-Output
MSA	Metasurface Antenna
MW	Microwave
OBF	Optical Beam Former
PAA	Phased-Array Antenna
PCB	Printed Circuit Board
PD	PIN Diode
PEC	Perfect Electric Conductor
PESA	Passive Electronically Scanned Array
PPW	Parallel-Plate Waveguide
RC	Resistor and Capacitor Circuit
RF	Radio Frequency
RLC	Resistor, Inductor and Capacitor Circuit
RMSA	Reconfigurable MSA

SATCOM	Satelite Communications
SDA	Slot Dipole Antenna
SDMA	Spatial Division Multiple Access
SFIR	Spatial Filtering Interference Rejection
SOLR	Square Open-Loop Resonator
SOTM	SATCOM On-The-Move
SRF	Self-Resonance Frequency
TDMA	Time Division Multiple Access

1 INTRODUÇÃO

1.1 CONTEXTUALIZAÇÃO

Na engenharia de micro-ondas, meta-superfícies são meios que podem apresentar propriedades que não ocorrem comumente em materiais encontrados na natureza, como permissividade elétrica ou permeabilidade magnética negativa. Tais dispositivos são implementações 2-D da tecnologia de meta-materiais, onde um arranjo de estruturas metálicas ressonantes de dimensões inferiores a um comprimento de onda é usado. Esse tipo de superfície pode ser usado para criar uma série de fenômenos eletromagnéticos (LI; SINGH; SIEVENPIPER, 2018; SMITH; PENDRY; WILTSHIRE, 2004).

Antenas baseadas em meta-superfícies vem sido extensivamente implementadas nas últimas décadas, explorando várias técnicas e tecnologias diferentes. (OVEJERO; MACI, 2015; MINATTI et al., 2016; BODEHOU et al., 2019), por exemplo, fazem uso meta-superfícies moduladas, as quais foram introduzidas primeiramente por Oliner e Hessel (1959), usando condições de fronteira de impedância na camada do arranjo de antenas e sua interação com a onda de superfície lançada no alimentador. No trabalho de Faenzi Gabriele Minatti e Maci (2019), uma série de diferentes elementos são tratados, no que tange ao uso arranjo de antenas em meta-superfícies.

Fong et al. (2010) descrevem o método de calcular a varredura do feixe usando superfícies de impedância artificial. Neste trabalho, um padrão de interferência é calculado, padrão este que contém a informação da direção de apontamento do feixe de interesse. Então, a intensidade de interferência é relacionada a uma impedância correspondente. Deste modo, um mapa de impedâncias específico é criado para cada padrão de interferência. Outros autores também tratam o problema de meta-superfícies usando o cálculo de superfícies de impedância artificial (SIEVENPIPER et al., 2002; SIEVENPIPER et al., 2003; ZHANG et al., 2018).

A técnica de holografia pode ser usada como ferramenta na formatação de feixe. Holografia é uma técnica primeiro tratada por Garbor (1948) e comumente usada em engenharia óptica. Nas últimas décadas, essa técnica foi adaptada para criar antenas em meta-superfícies, também conhecida como formadores de feixes holográficos. Meta-superfícies que usam o procedimento de holografia para formatar o diagrama de radiação, usam uma fonte onda eletromagnética conhecida e uma predição do diagrama de radiação desejado para calcular o holograma, o qual espalha o sinal da cavidade para o espaço livre na direção de interesse. Sistemas reconfiguráveis podem ser feitos usando-se alguns dispositivos para alterar o estado de ressonância da célula da meta-superfície. Alguns exemplos de implementações fazem uso de camadas de cristal líquido, diodos PIN, varactors, transistores, MEMS, switches e etc (LIPWORTH et al., 2013; LIPWORTH et al., 2016; STEVENSON et al., 2016; YURDUSEVEN et al., 2017).

Muitas empresas usam e desenvolvem antenas em meta-superfícies para módulos radar ou sistemas de antenas, tais como Kymeta Corp., Pivotal Commware, Alcan Systems, Echodyne,

Paradigm e Metawave, apenas para citar algumas companhias.

1.2 OBJETIVOS DO TRABALHO

O principal objetivo deste trabalho é criar um arranjo de antenas capaz de focalizar a energia eletromagnética propagada em uma dada direção do espaço usando a técnica de holografia. Este problema pode ser melhor descrito dividindo esse objetivo principal nos sub-tópicos a seguir:

1. Revisar os fundamentos das teorias de antenas e arranjos de antenas, antenas de meta-superfície e holografia;
2. Apresentar um procedimento de cálculo computacional de holograma, usando uma linguagem de cálculo numérico;
3. Desenvolver um modelo de um arranjo de antenas que seja capaz de incorporar o holograma proveniente da técnica de holografia em sua superfície e adotar as características do mesmo;
4. Desenvolver um arranjo de antenas reconfigurável que permita a alteração do diagrama de radiação da mesma sem usar técnicas convencionais, tais como lentes, matrizes de componentes passivos, defasadores, amplificadores e etc;
5. Desenvolver uma antena capaz de implementar um diagrama de radiação com múltiplos feixes em diferentes direções de interesse;
6. Desenvolver um método de otimização para ajustar o diagrama de radiação de acordo com os parâmetros de interesse;
7. Desenvolver o hardware capaz de alimentar e controlar o arranjo de antenas proposto.

1.3 ORGANIZAÇÃO DA DISSERTAÇÃO

O presente capítulo é destinado a contextualizar o trabalho proposto e apresentar os objetivos identificados.

O capítulo 3 apresenta os conceitos fundamentais necessários para criar uma base para as ideias propostas. A mesma discorre sobre a teoria de antenas e arranjos de antenas e descreve o funcionamento de antenas do tipo fenda-dipolo. Este capítulo também trata sobre holografia, o dispositivo diodo PIN, antenas de meta-superfície, otimização convexa e filtros de ressonadores acoplados.

O capítulo 4 apresenta a estrutura e o princípio de funcionamento de um arranjo de antenas feito sobre meta-superfície e uso de holografia na formação de feixe. Também apresenta o princípio de reconfigurabilidade da antena. Por fim, o capítulo apresenta circuitos adicionais para o funcionamento correto da antena.

O capítulo 5 apresenta os resultados obtidos no procedimento holográfico e no processo de otimização de convexa.

O capítulo 6 apresenta as considerações finais e discute brevemente sobre possíveis trabalhos futuros.

1.4 CONTRIBUIÇÕES

As seguintes contribuições são destacadas:

- Uso do diodo PIN em célula de meta superfície operando na banda Ku;
- Implementação de técnica de holografia para se configurar o diagrama de radiação da antena usando a ferramenta CVX/MATLAB;
- Uso de otimização convexa aliado a técnica de holografia para se calcular o diagrama de radiação;
- Desenho de rede de controle para antena tipo fenda e diodo PIN inseridos na meta superfície;
- Implementação de filtros de ressonadores de laço aberto acoplados na banda Ku;
- Desenho de circuito de controle para diodo PIN usando controlador de corrente de LED em configuração Daisy chain;
- Comparação da criação da onda objeto usando as técnicas de projeção em campo distante e síntese de fator de arranjo;
- Validação computacional de arranjo de antena reconfigurável para criação de diagramas de radiação com múltiplos feixes.

2 INTRODUCTION

2.1 PREFACE

In microwave engineering, metasurfaces are mediums that can present properties that rarely occur in common materials in nature, like negative electric permittivity or magnetic permeability. Such devices are a 2-D implementation of metamaterials technology, where an array of metallic resonant subwavelength elements is used. This kind of surface can be used to create a series of electromagnetic phenomena (LI; SINGH; SIEVENPIPER, 2018; SMITH; PENDRY; WILTSHIRE, 2004).

Metasurface antennas have been widely implemented in the last decade, exploiting different techniques and technologies. Ovejero e Maci (2015), Minatti et al. (2016), Bodehou et al. (2019), for example, makes use of modulated metasurfaces antennas, which were first introduced by Garbor (1948), using Impedance Boundary Conditions (IBC) on the antenna array layer and its interaction with the surface wave launched by the feeder. In the work of Faenzi Gabriele Minatti e Maci (2019), a novel of different elements is depicted for the metasurface antenna array use.

Fong et al. (2010) describes a method to calculate beam steering using artificial impedance surfaces. In this work, Fong et al. (2010) calculates a field interference pattern, which contains the beam direction information. Then, for any intensity of interference is assigned a correspondent impedance. Thus, a specific impedance map is created for every interference pattern. Other authors also treated the metasurface problem using the artificial impedance surface calculation (SIEVENPIPER et al., 2002; SIEVENPIPER et al., 2003; ZHANG et al., 2018).

The holographic technique can be used as a beamforming tool. Holography is a technique first treated by Garbor (1948) and commonly used in optics engineering. In the last decades, this technique was adapted to create metasurfaces antennas, also known as holographic beamformers. Metasurfaces that use holographic procedures to determine the metasurface pattern, use a known electromagnetic wave source and a prediction of the desired radiation pattern to calculate hologram, which can scatter the feed signal to the space in the desired direction. Reconfigurable systems can be made using elements that can change the resonant state of the metasurface cell. Some examples of implementations makes use of liquid crystal layers, PIN diodes, varactors, transistors, MEMS, switches and etc (LIPWORTH et al., 2013; LIPWORTH et al., 2016; STEVENSON et al., 2016; YURDUSEVEN et al., 2017).

Several companies are using and developing metasurface antennas in their radar modules or antenna systems, such as Kymeta Corp., Pivotal Commware, Alcan System, Echodyne, Paradigm, and Metawave, just to list some corporations.

2.2 OBJECTIVES

1. Review the fundamentals of the antenna and antenna arrays, metasurface antennas, and holography theories;
2. Development of a computational procedure to calculate the hologram, using some numeric computational language;
3. Development of an antenna array model that is able to incorporate the hologram from the holographic procedure at the antenna array surface and adopt its characteristics;
4. Development of reconfigurable antenna array that permits the modification of its radiation pattern, without use lenses, passive beamforming networks, phase shifters, amplifiers, etc;
5. Development of an antenna able to implement multi-beam radiation patterns at different space directions;
6. Development of an optimization method to adjust the radiation pattern according to the user's parameters;
7. Development of the hardware able to feed and control the proposed antenna array.

2.3 ORGANIZATION OF THIS DISSERTATION

The current chapter makes a brief review of the topics discussed in this following work and their presence in the literature and commercial market. Furthermore, this chapter also presents the objectives of this work.

Chapter 3 discuss about the background required to the proposed ideas. This chapter writes about antenna theory, holography, metasurface antennas, convex optimization, PIN diode behavior, and coupled open-loop filters.

Chapter 4 presents the used structure and working principle of metasurface antennas and the use of holography in beamforming application. This section also describes the reconfigurability of the proposed antenna. Moreover, additional circuits that are necessary to the correct operation of the proposed metasurface antenna are also exploited.

Chapter 5 show the results achieved during the holographic procedure and convex optimization routines.

Chapter 6 make the last considerations and present some possible future works.

2.4 CONTRIBUTIONS

The following contributions are highlighted:

- Use of PIN diode in Ku band metasurface cell;

- Implementation of holographic procedure to calculate the radiation pattern of the antenna using CVX/MATLAB;
- Use of convex optimization allied to holographic technique to calculate the radiation pattern;
- Design of metasurface control network cell to slot dipole antennas and PIN diode;
- Implementation of bandpass filters using coupled open-loop resonators in Ku band;
- Design of control circuit for PIN diode using LED current driver in Daisy chain configuration;
- Comparison of object wave using the techniques of back-propagated field and array factor synthesis;
- Computational validation of reconfigurable antenna array to create multi-beam radiation patterns.

3 FUNDAMENTAL CONCEPTS

3.1 ANTENNA CELLS AND ARRAYS

3.1.1 Antennas

An antenna is a transducer that converts electrons into photons and photons in electrons. Typically, an antenna is a conductor device scaling a portion of the wavelength of interest. This device can transmit and receive electromagnetic fields in space in specific directions and for a long distance, in some cases. Consequently, this element is generally used to perform wireless communications, medical applications, to make measurements, imaging, tracking, and is an important device in electronic warfare.

3.1.2 Radiation Pattern

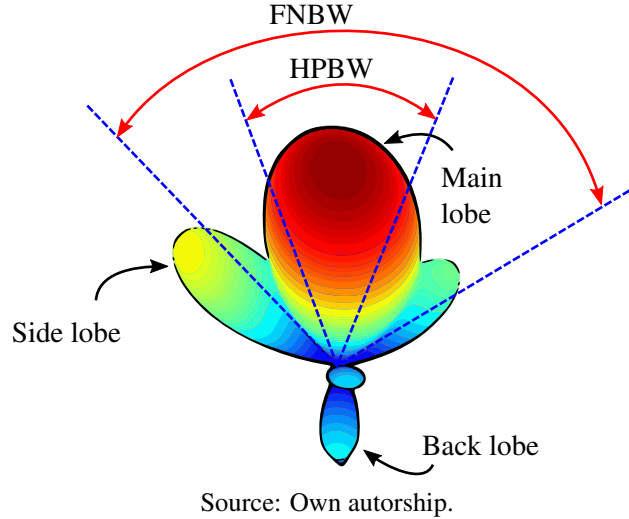
The antenna radiation pattern is a form to represent the radiation capabilities of a resonant radiator in a coordinate system. Usually, this representation can be done using a 2-D graphic, a 3-D surface, a data table, or a mathematical equation. Concerning the correct nomenclature of the radiation pattern, it is called a field pattern, if expressed on a linear scale and power pattern, if expressed on a logarithmic scale. Once the radiation pattern is defined, it is possible to detail the antenna's directivity, polarization, radiation intensity and the radiated power density (BALANIS, 2005). The radiation characteristics of an antenna can be simply summarized as directional, sectorial, or omnidirectional. The first type has the capability to focus the radiated energy on a specific point in the space, the second one mainly radiates the energy in a given angular sector, while the third one radiates constantly in all directions of one of the coordinate directions¹. A representation of a directional radiation pattern is depicted in Figure 3.1.

Figure 3.1 shows the most important definitions of radiation pattern. The lobes, which can be sub-classified as a main, side, or back lobe, are defined by Balanis (2005) as a portion of the radiated field where its borders are surrounded by weak radiation intensity. The main lobe is the greatest of the lobes and, when it exists, it points towards the focus direction of the radiation pattern. The back lobe points to the opposite angle of the main lobe. The side lobes are the portion of the radiated field which concentrates in the other directions in a low level of strength. The side and back lobes are also called minor lobes since their level is expected to be lower than the main lobe. An important metric of quality of a directional antenna is the front-to-back ratio, which quantifies the ratio between the levels of the main and back lobe, a high back lobe evidence that the antenna waste a great portion of radiated energy in the opposite direction of interest.

Other pertinent metrics related to the directional radiation pattern, and measures the beamwidth of the pattern, are the Half-Power Beamwidth (HPBW) and the First-Null Beamwidth (FNBW).

¹One geometry which exhibits its characteristics is the toroid.

Figure 3.1: Representation of a radiation pattern example with its most important definitions drawn.



Both metrics are measured in angles, but the HPBW counts the distance from the angle of maximal radiation to the angle when it decreases to the half, while the FNBW measures the distance from the first two angles of minimum radiation which include the angle of maximal of the diagram.

3.1.3 Radiated power, radiation density, and radiation intensity

The radiated power of an antenna computes all the power that is radiated by the antenna after considering all the losses and is given by

$$P_{rad} = \epsilon_L(1 - |\Gamma|^2)P_{in}, \quad (3.1)$$

where P_{in} is the input power, ϵ_L is efficiency related to the losses and reflections in excitation circuit and Γ is the coefficient reflection at the input port of the antenna (MAILLOUX, 2005).

The radiated power density is given by

$$S = \frac{P_{rad}}{4\pi d^2}, \quad (3.2)$$

where d is the distance between the antenna and the point of observation (MAILLOUX, 2005). The radiation density calculates all the radiated power over a spherical surface of radius d . Equation (3.2) establishes the radiated power density to an omnidirectional antenna. If the antenna under analysis is directional Eq. (3.2) must be corrected by the gain of the antenna, $G(\theta, \varphi)$, given by (MAILLOUX, 2005):

$$S(\theta, \varphi) = \frac{P_{rad}G(\theta, \varphi)}{4\pi d^2}. \quad (3.3)$$

On the other side, the radiation intensity evaluates all the radiated power per unit of solid angle and can be calculated by (BALANIS, 2005):

$$U(\theta, \varphi) = d^2S(\theta, \varphi). \quad (3.4)$$

3.1.4 Directivity and Gain

Directivity is defined as the ratio of the radiation power density to the average radiation power density and is completely determined by the radiation pattern of the antenna. This measure can be computed with Eq. (3.5) (STUTZMAN; THIELE, 2013):

$$D(\theta, \varphi) = 4\pi \frac{S(\theta, \varphi)}{\int_{\Omega} S(\theta, \varphi) d\Omega}. \quad (3.5)$$

In Equation (3.5), Ω can be defined by:

$$\Omega = \{\forall(\theta, \varphi) \in \mathbb{R}^2 | \theta \in [0, \pi], \varphi \in [0, 2\pi)\}. \quad (3.6)$$

The gain of an antenna is a measure of how efficiently the antenna can radiate the input power through space regarding its directivity (STUTZMAN; THIELE, 2013). Due to this, the gain can be related to the directivity by

$$G(\theta, \varphi) = \epsilon_L(1 - |\Gamma|^2)D(\theta, \varphi). \quad (3.7)$$

3.1.5 Polarization

At any point in the space, in the far-field, the polarization of an antenna is the same as the local plane wave observed by a viewer. This is measured using the polarization ellipse. The metric that evaluates this is the axial ratio, which computes the ratio between the major to the minor axis of the polarization ellipse (STUTZMAN; THIELE, 2013). The polarization is always elliptic ranging through the linear to the circular extremes.

An additional definition that must be defined is the concepts of co-polarization and cross-polarization. Co-polarization represents the orientation of the polarization where the field must radiate. On the other hand, the cross-polarization represents the polarization orthogonal to the co-polar one (BALANIS, 2005). Furthermore, when the polarization of the field is circular or elliptic, the field components can rotate clockwise, right-hand polarization, or counterclockwise, left-hand polarization.

3.1.6 Antenna Array

An antenna array is a set of elementary antennas in a specific pattern. Clustering some elementary antennas together affects the radiation pattern and gain of the entire ensemble. Hence, this strategy is commonly used to create a specific radiation pattern shape or improve the gain of the antenna for a particular application. The antenna array is considered an antenna itself.

If one assumes that the radiation pattern is described by the function $\vec{e}(\theta, \varphi)$, so the antenna array radiation pattern must be modified to (BROWN, 2012a):

$$\vec{E}(\theta, \varphi) = \vec{e}(\theta, \varphi)AF(\theta, \varphi). \quad (3.8)$$

In Equation 3.8, $AF(\theta, \varphi)$ is the so called the array factor of the set that is detailed in

$$AF(\theta, \varphi) = \sum_{m=1}^M \left(\sum_{n=1}^N A_{mn} e^{jk\vec{\rho}_{mn} \cdot \hat{r}(\theta, \varphi)} \right). \quad (3.9)$$

Equation (3.9) depicts an array factor of a $M \times N$ array. In its definition k is the wave number, a_{mn} is complex time-delayed excitation of any elementary antenna, \hat{r} is the radial component in a spherical coordinate system and $\vec{\rho}$ is the vector position of each antenna. These terms are expressed in the equations stated below:

$$k = \frac{2\pi}{\lambda}, \quad (3.10)$$

$$\hat{r}(\theta, \varphi) = \sin(\theta) \cos(\varphi) \hat{x} + \sin(\theta) \sin(\varphi) \hat{y} + \cos(\theta) \hat{z}, \quad (3.11)$$

$$\hat{r}_0(\theta_0, \varphi_0) = \sin(\theta_0) \cos(\varphi_0) \hat{x} + \sin(\theta_0) \sin(\varphi_0) \hat{y} + \cos(\theta_0) \hat{z}, \quad (3.12)$$

$$\vec{\rho}_{mn} = md_x \hat{x} + nd_y \hat{y}, \quad (3.13)$$

$$A_{mn} = a_{mn} e^{-jk\vec{\rho}_{mn} \cdot \hat{r}_0(\theta_0, \varphi_0)}. \quad (3.14)$$

In (3.11), d_x and d_y are the space between the antennas. Incorporating the phase of the time-delayed signal into the exponential of the array factor results in

$$AF(\theta, \varphi) = \sum_{m=1}^M \left[\sum_{n=1}^N a_{mn} e^{jk\vec{\rho}_{mn} \cdot (\hat{r}(\theta, \varphi) - \hat{r}_0(\theta_0, \varphi_0))} \right]. \quad (3.15)$$

It is important to emphasize that this formula describes an Electronically Scanned Antenna Array² (ESAA). Normally, Equation (3.15) states the array factor for a true-time delay ESAA. Nevertheless, if the ESAA makes use of phase shifters, that are typically frequency dependent and narrow-band, Eq. (3.16) must be used to compute the array factor (MAILLOUX, 2005):

$$AF(\theta, \varphi) = \sum_{m=1}^M \left[\sum_{n=1}^N a_{mn} e^{jk(md_x u(\theta, \varphi) + nd_y v(\theta, \varphi))} \right], \quad (3.16)$$

$$u(\theta, \varphi) = \frac{f}{f_0} \sin(\theta) \cos(\varphi) - \sin(\theta_0) \cos(\varphi_0), \quad (3.17)$$

$$v(\theta, \varphi) = \frac{f}{f_0} \sin(\theta) \sin(\varphi) - \sin(\theta_0) \sin(\varphi_0). \quad (3.18)$$

In (3.17)-(3.18), f_0 is the center frequency of operation.

These definitions are valid for common antennas and antenna arrays, including the slot antenna and array presented in the next section.

²Also called a phased array.

3.2 SLOT ANTENNAS

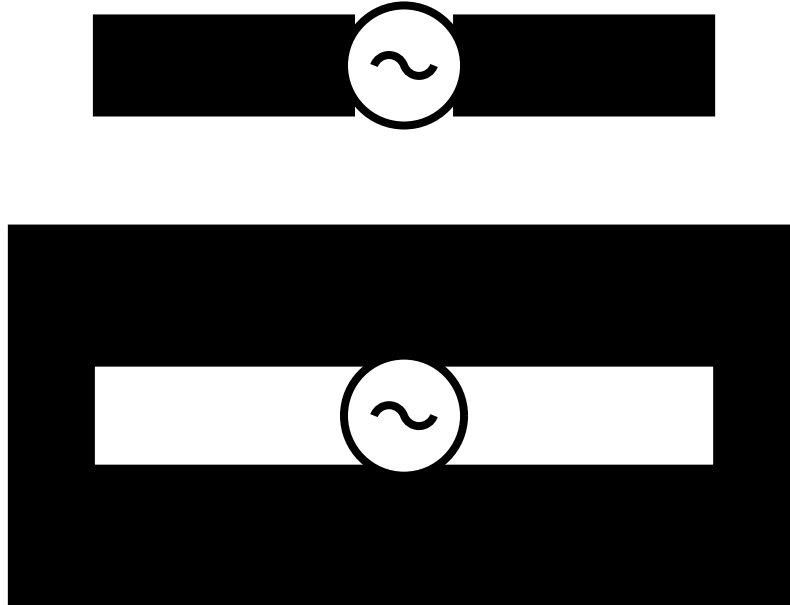
3.2.1 Slot Dipole Antenna

A dipole antenna is a straight wire, or in general a conductor, that is commonly centered feed. The currents flowing in this antenna have a sinusoidal form, along the conductor and can be approximated by (BALANIS, 2005):

$$I(x, y, z) = I_o \sin \left[k \left(\frac{l}{2} \right) - |z| \right], |z| \leq \frac{l}{2}. \quad (3.19)$$

Slot Dipole Antennas (SDA) are complementary to the classical dipole antennas. This type of antenna is some type of slit in metal sheets. The feed of this antenna is different from the typical dipole antenna. The common feed mechanisms in classical and slot dipole antennas are depicted in Fig. 3.2.

Figure 3.2: Excitation of classical dipole and slot dipole antennas. The feed signal is introduced along the length of the classical dipole, and along the width of the slot dipole antenna.



Source: Own autorship.

One way to feed the slot dipole antenna is by creating some surface or guided wave underneath its layer. The path of the surface currents flowing at this layer is interrupted when it impinges the slot. The currents then contour the slot and continue their flow. This current disturbance determines the radiation pattern of the slot dipole antenna. Once these surface current densities \vec{J} are known the radiation vector can be calculating the 2-D spatial Fourier transform of this density using (ORFANIDIS, 2016). In Equation (3.20), A is the area where the charges are accumulated:

$$\vec{F}(\theta, \varphi) = \iint_A \vec{J}(\vec{\rho}_A) e^{jk\vec{\rho}_A \cdot \hat{r}(\theta, \varphi)} dA, \quad (3.20)$$

$$\vec{\rho}_A = x_a \hat{x} + y_a \hat{y}, \quad (3.21)$$

where A is the aperture area and (x_a, y_a) are the points over this area.

The surface current density is also related to the electric and magnetic aperture fields at the slot aperture. If the screen around the aperture is a perfect electric conductor, or in other words obeys a Dirichlet boundary condition, the electric density current vanishes. If the screen is a magnetic perfect conductor, or in other words obeys a Neumann boundary condition, the magnetic current density vanishes (TAI, 1994). These relationships can be expressed in Eqs. (3.22)-(3.23) (ORFANIDIS, 2016), depicted below,

$$\vec{J}_s(\vec{\rho}_A) = 2(\hat{n} \times \vec{H}_a(\vec{\rho}_A)), \quad (3.22)$$

$$\vec{J}_{ms}(\vec{\rho}_A) = -2(\hat{n} \times \vec{E}_a(\vec{\rho}_A)). \quad (3.23)$$

In these equations \hat{n} are the normal vector to the aperture. Afterward, the electric and magnetic radiation fields can be calculated using the radiation vector, using Eqs. (3.24)-(3.25) (ORFANIDIS, 2016):

$$\vec{E}_{rad}(\theta, \varphi) = jk \frac{e^{-jkd}}{4\pi d} \hat{r} \times \vec{F}_{ms}(\theta, \varphi), \quad (3.24)$$

$$\vec{H}_{rad}(\theta, \varphi) = -\frac{jk}{\eta} \frac{e^{-jkd}}{4\pi d} \hat{r} \times (\vec{F}_{ms}(\theta, \varphi) \times \hat{r}), \quad (3.25)$$

$$\eta = \frac{\mu}{\varepsilon}, \quad (3.26)$$

where \vec{F}_{ms} is the radiation vector of Eq. (3.20) using the magnetic surface current density of Eq. (3.23).

The SDA irradiates more than a common strip dipole, once the current spread over the metal sheet is greater. Another tool that can be used to analyze the fields of the SDA is Babinet's principle. This principle states that the radiation patterns of the SDA are the same as the wire dipole antenna. The only difference is that the vibrating directions of the electric and magnetic fields are interchanged (BOOKER, 1946).

The SDA possesses linear polarization, however, the circular polarization can be achieved using a cross-dipole configuration, where two dipoles are placed orthogonally, combining vertical and horizontal polarization.

3.3 SLOT ANTENNA ARRAY

In order for the slot to radiate, it must interrupt the flow of one of the components of the density current. When the slot is placed in the direction of the path of the current, the current must go around the slot, this couples the energy of the cavity to the slot and then in the free space. The currents over the cavity are proportional to the magnetic field. To control the power coupling in the slot, the angle of the slots can be used. Another way is using the natural intensity of the magnetic field in the cavity. This power coupling mechanism must be used to control the amount of energy that leaky along the area of the entire antenna (BALANIS, 2005).

The slots in the medium determine the behavior of the radiation pattern of the antenna. Narrow slots generate a narrow beam, with high cross-polarization rejection at the resonant frequency. Wider slots can have large bandwidth with an appropriate impedance match, but the polarization rejection is decreased (BALANIS, 2005).

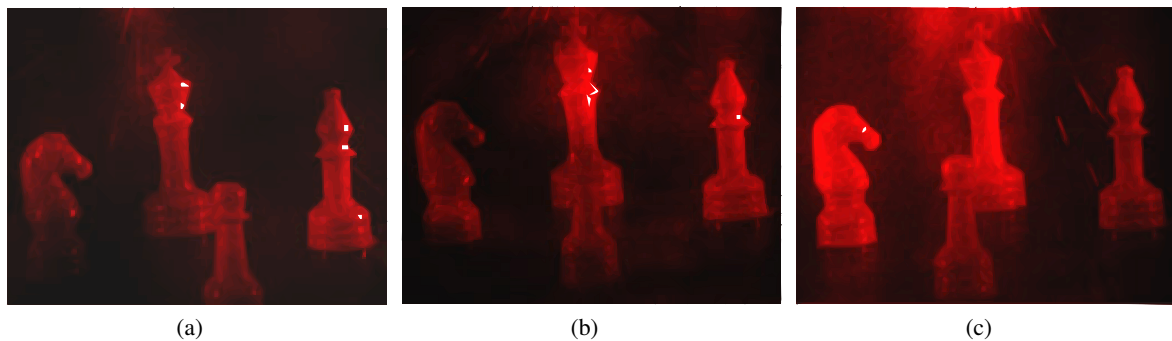
The wave under this medium has a complex wavenumber, with a non-zero real attenuation part. This attenuation is provided by the leakage of microwave power in the slots. These types of antennas typically were designed to leaky at least 90% of the enclosed power, before reach the end of the antenna. The rest of the power can be dissipated in some way, to prevent undesirable effects (STUTZMAN; THIELE, 2013).

This type of antenna and array will be used in the proposed antenna and will be the surface where the radiation pattern will be recorded, using the holographic theory. This theory is more detailed in the next section.

3.4 HOLOGRAPHY

Holography is the procedure used to record three-dimensional scenes in a two-dimensional plane and reconstruct this information without the use of any lens. Different from the photographic procedure, where just the brightness of the scene is recorded, in the holography the phase of light, the variable which contains the information about the shape of the scene, is also recorded. Due to this, in holography, a 3D copy of the scene can be recorded and reconstructed, while in photography just a 2D copy of the scene can be reconstructed (ACKERMANN; EICHLER, 2007). This true three-dimensional reconstruction creates even effects like depth and parallax, as shown in Figure 3.3 (HOLOGRAPHY, 2020).

Figure 3.3: Different views of the same hologram varying the position of observation from the (a) left to the (c) right side, due to the parallax effect.



Source: Reproduced from Georgia State University HyperPhysics website³.

Additionally, in the photography, each point of the photographic film has registered just a piece of the whole information, while in the holography each point of the hologram contains all the information of the scene, which means that it is possible to display the entire scene even with a small part of the created hologram (HOLOGRAPHY, 2020).

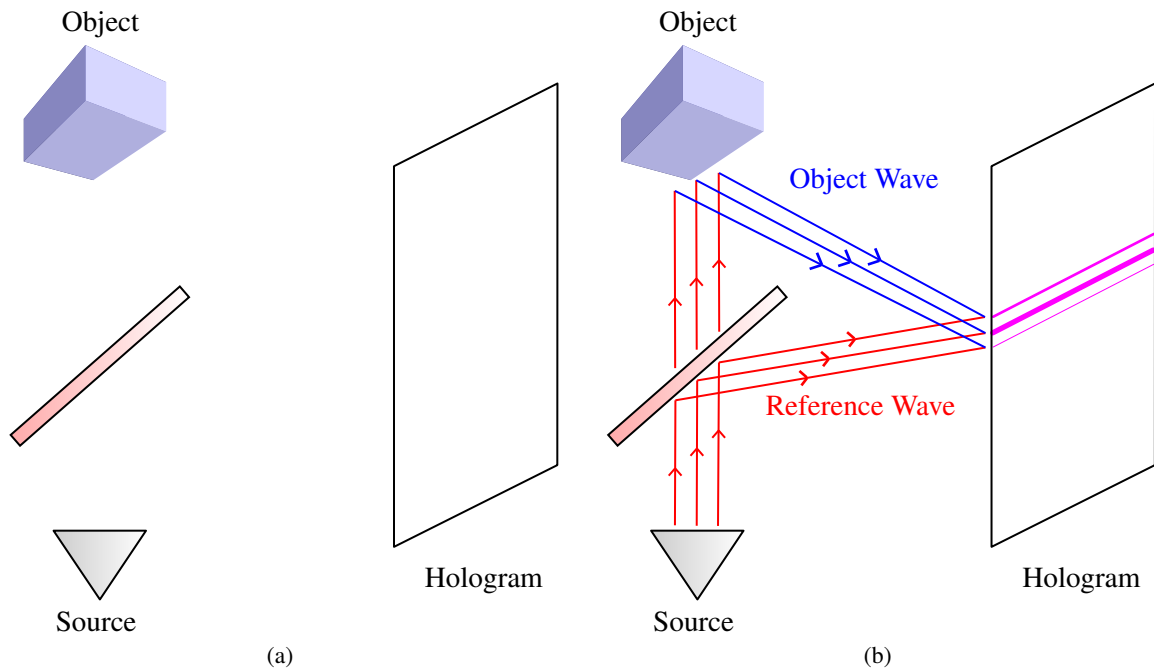
3.4.1 The holographic procedure

This procedure consists of two main processes, the record, and the reconstruction process. The first one, the recording process, consists of register the information about the scene/image in the hologram. To explain this operation it is necessary to use the experimental setup schematically exposed in the Figure 3.4a. This setup contains one layer to record the hologram, a high-frequency wave source, a splitter, and the object/scene to be registered. The splitter is used to divide and diffract part of the rays to the hologram while another portion continues to the object.

To record the information about the image in the hologram it is necessary illumination of a known coherent wave, which is called the reference wave. This wave, on the other hand, scatters in the object and creates another wave, called object wave (HARIHARAN, 2002). This object wave contains all the information of the object resumed in two parameters, the amplitude, which

³Available in: <<http://hyperphysics.phy-astr.gsu.edu/hbase/optmod/holog.html>>. Accessed: 22 June 2020.

Figure 3.4: (a) Experimental setup to perform the holography experiment. (b) Exemplification of the recording process.



Source: Own autorship.

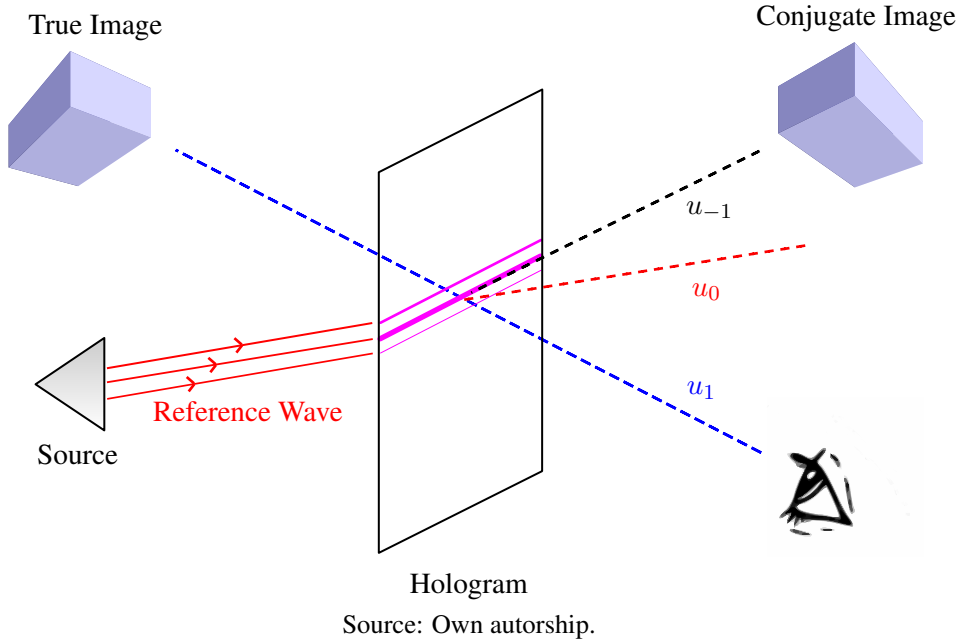
describes the brightness, and the phase, which details the shape of the object (ACKERMANN; EICHLER, 2007). During the recording, the phase of the object is converted light intensity variation (HARIHARAN, 2002). These two waves impinge in the register layer and interfere with each other. This interference pattern is then recorded in the register layer, and the hologram is now created. These steps describe the recording process depicted in Figure 3.4b.

When the reference wave collides with hologram it diffracts in the interference pattern and some of these diverging rays converge to a copy of the object wave, creating a copy of the object. This is the reconstruction of the scene (ACKERMANN; EICHLER, 2007). During the reconstruction, the reference wave can diffract to one of three main beams. The first is the zeroth-order diffraction, which is just the reference wave passing through the hologram plane. The second one, the 1-st order diffraction, is the rays that create a virtual copy of the object. This beam is also called a true image or orthoscopic image. Lastly, the -1-st order diffraction is also created. This beam is a copy of the object with opposite phase information and is called real, conjugate, or pseudoscopic image (LIZUKA, 2008). This process is depicted in Figure 3.5. In the resume, two images are created during the reconstruction process.

3.4.2 Describing holography mathematically

To describes the holographic process mathematically is necessary to define the functions for the reference and object wave. To start, the coherent reference wave can be defined as a plane

Figure 3.5: Reconstruction holographic process is portrayed where the reference wave impinges in the hologram creating the true image, u_1 , the transmitted reference wave, u_0 and the conjugate image, u_{-1} .



wave in (3.27). The time dependence is omitted for simplicity of calculations, but the wave propagates as $+j\omega t$. In (3.27) $r(\mathbf{X})$ is the amplitude and Φ is the phase of the wave:

$$R(\mathbf{X}) = r(\mathbf{X})e^{-j\Phi}, \quad (3.27)$$

where the rectangle \mathbf{X} , of length L and width W , in position h , is the set of coordinate points of the hologram, defined below,

$$\mathbf{X} = \left\{ \forall x \in \mathbb{R}^3 \left| |x_1| \leq \frac{W}{2}, |x_2| \leq \frac{L}{2}, x_3 = h \right. \right\}. \quad (3.28)$$

In Equation (3.28) x_i are the coordinates over the hologram. The object wave does not have an analytical predefined form, once it depends on the form of the object where it is scattering. Due to this, a generic form is defined in

$$O(\mathbf{X}) = o(\mathbf{X})e^{-j\Psi}, \quad (3.29)$$

where $o(\mathbf{X})$ is the amplitude and Ψ is the phase of the wave⁴.

With these two waves defined, the interference of the recording process can be calculated as the superposition of both waves, and its intensity is defined below

⁴The notation used for object wave must not be confounded with the Big and Little-O notation. The input for object wave is a vector, while the input for Big ($O(n)$) and Little-O notation ($o(n^2)$) are scalars.

$$I(\mathbf{X}) = (R(\mathbf{X}) + O(\mathbf{X}))(R(\mathbf{X}) + O(\mathbf{X}))^*, \quad (3.30)$$

$$I(\mathbf{X}) = R(\mathbf{X})R(\mathbf{X})^* + O(\mathbf{X})O(\mathbf{X})^* + R(\mathbf{X})O(\mathbf{X})^* + O(\mathbf{X})R(\mathbf{X})^*, \quad (3.31)$$

$$I(\mathbf{X}) = r^2(\mathbf{X}) + o(\mathbf{X})^2 + r(\mathbf{X})o(\mathbf{X})e^{-j(\Phi-\Psi)} + r(\mathbf{X})o(\mathbf{X})e^{-j(\Psi-\Phi)}, \quad (3.32)$$

where the operator $*$ denotes the complex conjugate of a complex number.

The information of Eq. (3.31) is recorded in the hologram. The resultant hologram consists of a pattern of regular spaced fringes. The amplitude of each term of (3.32), resultant from the interference between the two waves, modulates the intensity of the fringes, while the phase modulates the distance of fringes in the interference pattern (HARIHARAN, 2007).

Using some trigonometric manipulations, Eq. (3.32) can be re-written as

$$I(\mathbf{X}) = r^2(\mathbf{X}) + o(\mathbf{X})^2 + 2r(\mathbf{X})o(\mathbf{X}) \cos(\Phi - \Psi), \quad (3.33)$$

where the phases Φ and Ψ are respectively

$$\Phi = \Phi(\theta_r, \rho) = \delta_r - 2\pi \left(\frac{\sin(\theta_r)}{\lambda} \right) \rho, \quad (3.34)$$

$$\Psi = \Psi(\theta_o, \rho) = \delta_o - 2\pi \left(\frac{\sin(\theta_o)}{\lambda} \right) \rho. \quad (3.35)$$

In Equation (3.34) and Eq. (3.35), λ is the wavelength, $\delta_{(r,o)}$ are the initial phases of the reference and object wave, $\theta_{(r,o)}$ are the angle of incidence in the hologram and ρ is the radius from the center of the hologram, given by

$$\rho = \sqrt{x_1^2 + x_2^2}. \quad (3.36)$$

Using Equations (3.34) and (3.35) in Eq. (3.33) results in

$$I(\mathbf{X}) = r^2(\mathbf{X}) + o(\mathbf{X})^2 + 2r(\mathbf{X})o(\mathbf{X}) \cos \left(\delta - \left(\frac{2\pi}{\lambda} \right) (\sin(\theta_r) - \sin(\theta_o)) \rho \right). \quad (3.37)$$

The last term of the right side of Eq. (3.37), where δ is the difference of the starting phases, is called interference term. To the interference occurs this term must not vanish. To satisfy this requirement δ must be constant since if it varies randomly it would result in a zero average. In

other words, to satisfy this criterion, the two waves must be coherent (ACKERMANN; EICHLER, 2007).

Another factor that can disappear with the interference term is the polarization of one wave according to the other. In (3.37) the polarizations of the two waves are assumed to be parallel. However, if this affirmative is not true, (3.37) must be re-written to

$$I(\mathbf{X}) = r^2(\mathbf{X}) + o(\mathbf{X})^2 + 2r(\mathbf{X})o(\mathbf{X}) \cos \left(\delta - \left(\frac{2\pi}{\lambda} \right) (\sin(\theta_r) - \sin(\theta_o)) \rho \right) \cos(\zeta), \quad (3.38)$$

where ζ is the angle between the polarizations of the two waves.

One metric of the quality of the hologram, which can be calculated from (3.39), is the visibility of the hologram (ACKERMANN; EICHLER, 2007):

$$V = \frac{\max I(\mathbf{X}) - \min I(\mathbf{X})}{\max I(\mathbf{X}) + \min I(\mathbf{X})}. \quad (3.39)$$

If $V = 0$, no interference pattern is recorded.

During the reconstruction process, when the hologram is impinged by the reference wave, the transmitted beam is equal to

$$T(\mathbf{X}) = R(\mathbf{X})I(\mathbf{X}), \quad (3.40)$$

$$T(\mathbf{X}) = r^3(\mathbf{X})e^{-j\Phi} + r(\mathbf{X})o(\mathbf{X})^2e^{-j\Phi} + r^2(\mathbf{X})o(\mathbf{X})e^{-j(2\Phi-\Psi)} + r^2(\mathbf{X})o(\mathbf{X})e^{-j\Psi}. \quad (3.41)$$

Equation (3.41) represents the wave displayed by the hologram when illuminated by the reference wave. The first term of the right side of (3.41) is the reference beam transmitted through the hologram and the second term is called the halo around the transmitted reference wave (HAR-IHARAN, 2002). These two contributions propagate in the same direction. The third term is the conjugate image of the record object, while the fourth term is the virtual image. Looking the definitions shown in Figure 3.5, the transmitted wave can be written as

$$T(\mathbf{X}) = u_0 + u_{-1} + u_1, \quad (3.42)$$

and the terms in Eq. (3.42) are presented below:

$$u_0(\mathbf{X}) = r^3(\mathbf{X})e^{-j\Phi} + r(\mathbf{X})o(\mathbf{X})^2e^{-j\Phi}, \quad (3.43)$$

$$u_{-1}(\mathbf{X}) = r^2(\mathbf{X})o(\mathbf{X})e^{-j(2\Phi-\Psi)}, \quad (3.44)$$

$$u_1(\mathbf{X}) = r^2(\mathbf{X})o(\mathbf{X})e^{-j\Psi}. \quad (3.45)$$

This formulation of the holographic theory can be used to enhance spatial beamforming applications, which are discussed in the next section.

3.5 SPATIAL BEAMFORMING

A reconfigurable antenna is any device that can change its resonant state, varying any of its parameters: beam shaping, pointing direction, polarization, sidelobe level, number of beams, gain, or impedance. This change can be achieved by several manners, like a change in the effective dielectric constant, in its physical dimensions or shape, in its impedance, or some alteration in the surface current path over the antenna.

The capability to adjust any of these parameters is a great tool to enhance the performance of the antenna, for a different set of applications, such as electronically scanning, Spatial Filtering Interference Rejection (SFIR), or Spatial Division Multiple Access (SDMA) (FENN, 2008).

SDMA is consequently the next evolution from the Time, Frequency, and Code Division Multiple Access (T/F/C-DMA). Multibeam antenna systems that use SDMA permits the separation of radiated signals to different users. This action allows the reuse of the channel resources, once each network subscriber can use the same time slot, frequency or code, concurrently, due to the spatial division and isolation between two adjacent channels (FENN, 2008).

SFIR antennas are generally used as spatial filters to reduce the interference level from the other users, or transmitters. Due to this, these systems increase their network capacity by limiting the interfere, the noise capture area, and multipath effects. The use of this technique reduces the frequency reuse spacing (FENN, 2008).

A electronically scanned antenna is a system able to perform beamforming without use mechanical parts, creating a directive beam in the desired direction. This characteristic is useful in tracking systems, mobile communication systems, Satellite Communications (SATCOM) On-The-Move (SOTM) (LESUR et al., 2018; FERRANDO-ROCHER et al., 2016; ETTORRE et al., 2015; MATOS et al., 2017; CHALOUN; ZIEGLER; MENZEL, 2016; SINGH et al., 2020), surface radar systems (WANG; CALOZ, 2021; LIU et al., 2021; RAHMAT-SAMII et al., 2005), missile seekers (VERMA, 2017; MARTIN et al., 1992), imaging (LIPWORTH et al., 2013), detection of arrival (ZHENG et al., 2021; YUAN; CHEN; SAWAYA, 2005; KIM et al., 2015), microwave repeaters, and autonomous driving (YU et al., 2020; CHIPENGO; SLIGAR; CARPENTER, 2020; ZHENG; LYU; WU, 2020).

3.5.1 Beamforming Architectures

Multiple-Input Multiple-Output (MIMO) is a system that is composed of a baseband radio, multiple antennas, Analog-to-Digital Converters (ADC), Digital-to-Analog Converters (DAC), and, sometimes, an external RF mixer. This technique of digital signal processing is used as a wireless technology to improve the communication link throughput. To do this, instead, send the signal through a single antenna, the signal is radiated by multiple antennas, where each excitation signal is created in the digital domain. MIMO permits to send and receive redundant signals in multiple antennas in the different spatial path, which improve the reliability. Furthermore, spatial

multiplexing can also be implemented, to increase the data rate. For these reasons, turns the multipath problem into an advantage (BLACK, 2017).

Another consolidated beamforming architecture is the Phased-Array Antenna (PAA). The PAA is an array of stationary antennas in which the feeding signal is used to control the beam scanning capability of the antenna. The coherence between the feeding signals at the antennas, from a variation in phase, time-delay, and/or amplitude, is used to define the region in the space where the energy will be focused (MAILLOUX, 2005).

PAA can be passive or active, and they can be called Passive Electronically Scanned Array (PESA), and Active Electronically Scanned Array (AESA), respectively.

The first type of PAA, PESA, is composed of an antenna array, a Beam Forming Network (BFN), a feed system, and a control system. The BFN subsystem is responsible to provide the beam steering ability in PESA. This element can be divided into four classes, the phase shifters networks, quasi-optical lenses, Digital Beam Former (DBF), and Optical Beam Former (OBF) (HANSEN, 2001).

Comprising the class of phase shifters networks, are the Butler (BUTLER; LOWE, 1961; BUTLER, 1966; ELMANSOURI; BOSKOVIC; FILIPOVIC, 2021; PALAZZI et al., 2021), Blass (BLASS, 1960; TSOKOS et al., 2018; LIM; CHAN, 2009), Nolen matrices (NOLEN, 1965; REN et al., 2019; DJERAFI; FONSECA; WU, 2010). These elements use an array of transmission lines phase shifters to create a coherent phase variation between the output ports.

In the class of quasi-optical lenses are the Rotman, and Bootlace lenses (ROTMAN; TURNER, 1963; GENT, 1957; TOLIN; LITSCHKE; BRUNI, 2019; CHOU; CHANG, 2019; WU; CHENG; HUANG, 2018). These lenses consist of a cavity formed by two surfaces, where the input and output ports of the BFN stay (BHATTACHARYYA, 2006). The signal from one input port travels through the cavity, and due to the different electric lengths of each travel path, each output port will present a different phase.

The DBF is a BFN where the phase shift is performed in the digital domain. This operation is typically achieved with a digital filter using a Hilbert transform. Moreover, this BFN requires a filter and ADC/DAC for each antenna element (BHATTACHARYYA, 2006).

In OBF the electrical signals from the antenna are transduced to optical signals through a photodiode. This signal then travels in fiber optics cables, where the length of the cable determines the time delay suffered by the signal. For this reason, this system is true-time delay BFN and can be used in wideband applications (FRANKEL; ESMAN, 1995; ESMAN; FRANKEL; PARENT, 1995; FRANKEL; ESMAN, 1995).

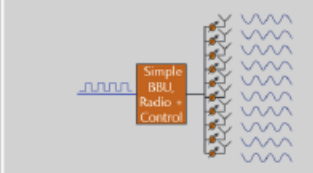
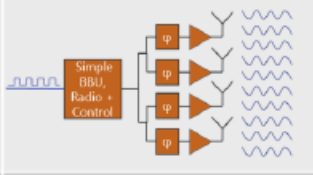
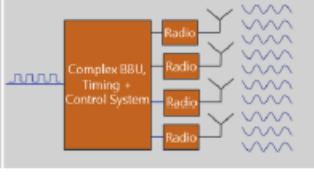
AESA systems use common passive BFN with amplifiers. The amplifier is used to adjust the amplitude of the signal, incorporating an additional variable to control the beam shaping. The freedom to adjust the amplitude of the excitation of each antenna permits implement more complex algorithms of beamforming techniques (MAILLOUX, 2007; BROWN, 2012b).

Holographic Beam Forming (HBF) systems are a type of PESA BFN, however, this system

does not use phase shifters to steer the beam, instead, uses a hologram to scatter the energy in the desired direction. The general structure of the HBF is detailed in (BILY et al., 2014), and consists of a guided-medium, a feed system, a control system, and scatter elements. This structure transforms the reference wave into the desired object wave through the hologram (BLACK, 2017).

Figure 3.6 depicts a comparison between MIMO, PAA and HBF systems. In this comparison, it is possible to notice that HBF is the lowest Cost, Size, Weight, and Power system between all the three.

Figure 3.6: Comparison between holographic beam former, phased array and MIMO.

Architecture	Block Diagram	Cost	Size	Challenges
Holographic Beam Former		Super-sampled COTS design enables low price	Thin, Conformable	Single beam per polarization per sub-aperture.
Phased Array		Distributed phase shifters and amplifiers pushes moderate price	Trades cost for thickness. Thin is very expensive	Thermal challenges difficult due to distributed amplification. Multi-beam significantly increases cost (more phase shifters, distribution layers)
MIMO		Radios behind every element and complex BBU drives high price and power consumption	Usually thick but antenna thickness can be reduced by hiding BBU in baseband cabinet	No FDD Unworkable at mmW Spectral Efficiency vs. cost scales poorly

Source: (BLACK, 2017).

In this work, to create a reconfigurable antenna, the PIN diode is used. This device can be incorporated to variate the resonance state of the antenna and described in the next section.

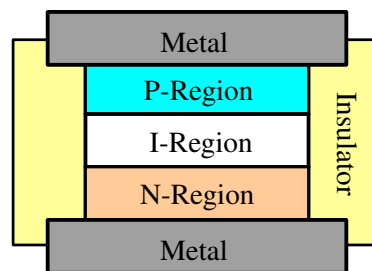
3.6 PIN DIODE

A PIN Diode is a semiconductor that is current-controlled. This device works as a variable resistor at RF and MW frequencies. The PIN Diode (PD) can be used in a variety of applications, depending on how its current is controlled. If the current is varied continuously, the PD works as an attenuator or a modulator device. On the other side, if the current is discretely switched, the PD operates as a phase shifter or a switch (DOHERTY; JOOS, 1998).

3.6.1 Pin Diode Structure and equivalent models

The structure of PD is presented in Figure 3.7. Its structure is composed of two highly doped p^+ and n^+ layers with an intrinsic lightly doped semiconductor inner layer. The structure have also two metallic contacts where the bias signal is applied. Additionally, some technologies use some type of insulator at the borders to reduce fringing capacitance (LUDWIG; BRETCHKO, 2000).

Figure 3.7: Physical structure of a PIN diode.



Source: Own autorship.

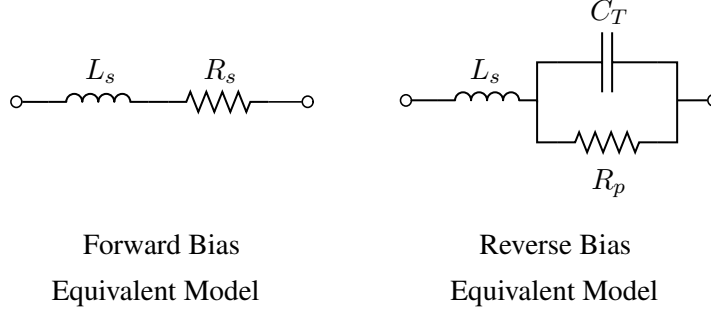
When the junction is forward biased the holes and electrons are injected into the intrinsic layer. These holes and electrons will recombine just after a finite lifetime, and until this, the stored charge will create a low-impedance path to the current flow. However, when the device is reverse biased, there is no injection of charge carriers in the intrinsic region and the PD appears as a capacitor shunted by a parallel resistance (DOHERTY; JOOS, 1998).

Thus, the PD can be described using an RLC equivalent model. The equivalent model for the forward and reverse biased condition is shown in Figure 3.8. R_s is the series resistance and forward biased and C_T is total junction capacitance. These two parameters depend on the width and area of the intrinsic junction, the mobility of the carriers, and the dielectric constant of the semiconductor (MACOM-TECHNOLOGIES-SOLUTIONS,). R_p is the parallel resistance when forward biased and depends on the wafer processing steps. L_s is the parasitic inductance added by the package geometrical properties (DOHERTY; JOOS, 1998).

Although the equivalent model of Figure 3.8 describes well the behavior of the reverse-biased state, Doherty e Joos (1998) affirms that when well passivated the parameter R_p , which represents the loss of capacitor, exhibits a value around 50 k Ω . Due to this, its value is higher than the

capacitance reactance and can be ignored, for practical purposes. Additionally, the R_s and R_p are inversely proportional to the reverse voltage bias and forward current bias.

Figure 3.8: PIN diode equivalent models for the forward and reverse bias. In the equivalent models, L_s is the parasitic inductance of the PIN diode package, R_s is series resistance, C_T is the total capacitance and R_p is the parallel resistance when reverse biased.



Source: Own autorship.

Moreover, to the reverse bias equivalent model be valid the operation frequency must be greater than the dielectric relaxation frequency of the intrinsic layer. According to [White \(1982\)](#), the dielectric relation frequency is usually equal to 1-2 GHz, and therefore, the model of [Figure 3.8](#) can be securely applied for frequencies greater than 5 GHz.

3.6.2 PIN diode as a switch

Analyzing [Figure 3.8](#) it is possible to observe that the PD provides a low-impedance path when forward biased, or in other words when the anode voltage is greater than the cathode voltage and provides a high-impedance path when reverse biased, or in other words when the anode voltage is lowest or equals to the cathode voltage. This statement stays more clear analyzing the complex impedance equations of the equivalent models, provided below

$$Z(j\omega) = R_s + j\omega L_s, \quad (3.46)$$

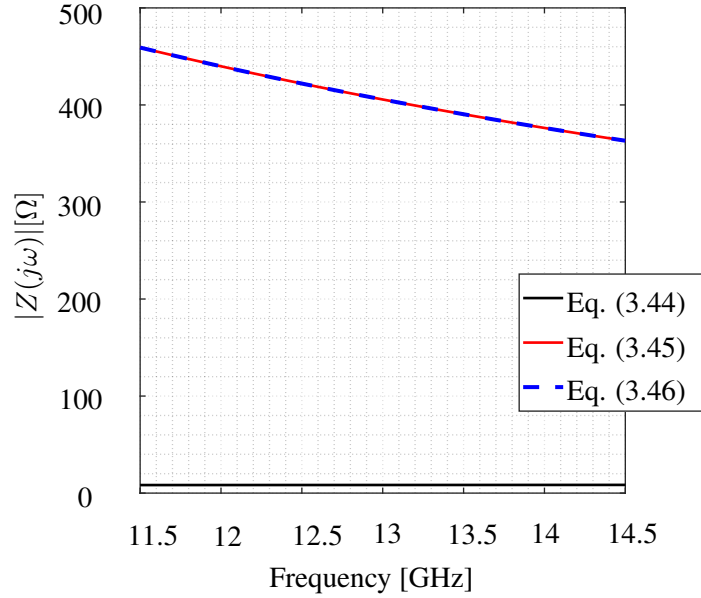
$$Z(j\omega) = \frac{R_p}{[1 + (\omega R_p C)^2]} + j \left\{ \frac{\omega^3 R_p^2 L_s C_T^3 + \omega(L_s + R_p C_T)}{[1 + (\omega R_p C_T)^2]} \right\}. \quad (3.47)$$

For values of R_p greater than some $k\Omega$, (3.47) can be simplified to

$$Z(j\omega) = j \left(\frac{\omega^2 L_s C_T - 1}{\omega C_T} \right). \quad (3.48)$$

The Equations (3.46), (3.47) and (3.48) have their curves plotted in [Figure 3.9](#). In this image it is distinctly evident the similarity of (3.47) and (3.48) and, more than this, observe the low-impedance achieved during the forward biasing, in (3.46), and the high-impedance reached during

Figure 3.9: Magnitude of the complex impedance of the (3.46), (3.47) and (3.48). For these curves were used $R_s = 8 \Omega$, $R_p = 50 k\Omega$, $L_s = 30 \text{ pH}$, $C_T = 0.03 \text{ pF}$ and $Z_0 = 50 \Omega$.



Source: Own autorship.

the reverse biasing, in (3.47). Therefore, regarding these characteristics, it is proved that the PD can be used as a switch device controllable by its biasing.

To apply the correct bias signal in its terminals is necessary to use the circuit presented in Figure 3.10. This setup is a classical circuit, where the inductors, L_{RF} , are used as RF chokes to the DC bias voltage source and the capacitors, C_{DC} , are used as DC blocks to the microwave source. The transmission lines of characteristic impedance Z_0 are the terminals where the PD is connected to act as a switch.

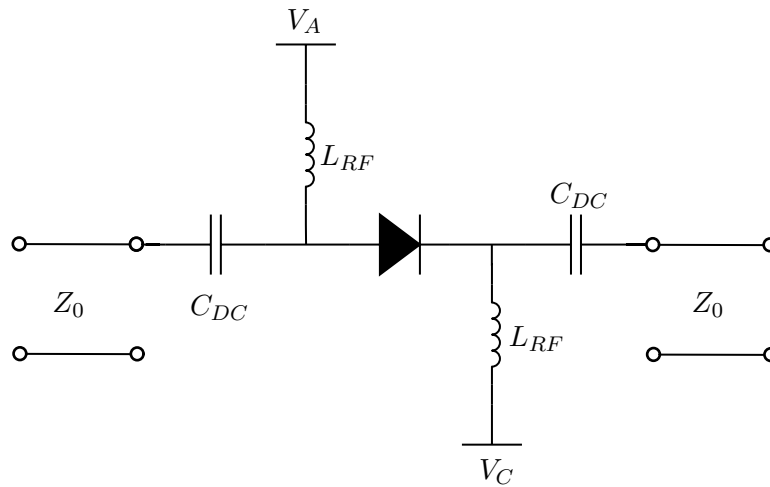
In the Figure 3.10 the PD is connected in series with the transmission lines, and the insertion loss and isolation can be calculated using the following equations, respectively (MACOM-TECHNOLOGIES-SOLUTIONS,):

$$\text{IL}(R_s, Z_0) = 20 \log_{10} \left(1 + \frac{R_s}{2Z_0} \right), \quad (3.49)$$

$$\text{Isolation}(f, C_T, Z_0) = 10 \log_{10} [1 + (4\pi f C_T + Z_0)^2]. \quad (3.50)$$

Figure 3.11 shows the results for these measures. In this figure, just the isolation is expressed in a curve, since the insertion loss does not depend on frequency. The insertion loss of the PD,

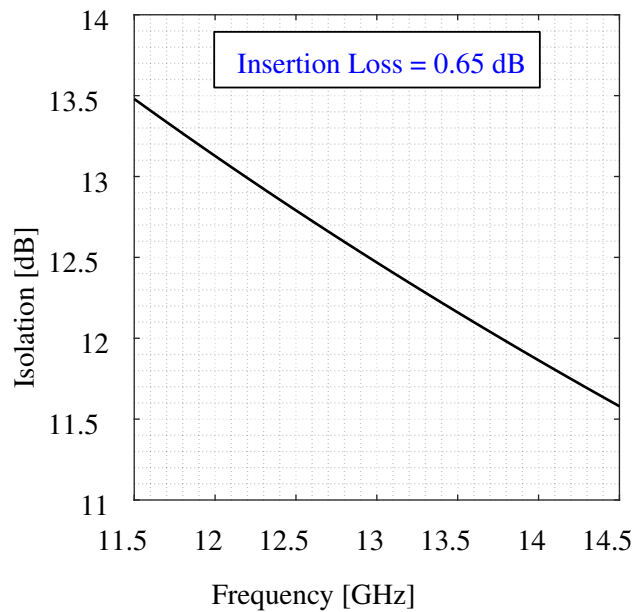
Figure 3.10: PIN diode bias circuit. V_A and V_C are the anode and cathode bias voltages, L_{RF} is the RF choke inductance, C_{DC} is the DC block capacitor and Z_0 is the characteristic impedance of the connected transmission line.



Source: Own autorship.

when forward biased, depends just on the characteristic impedance of where it is connected and the series resistance and tends to grow with this last one, as exemplified, for practical values, in Figure 3.12.

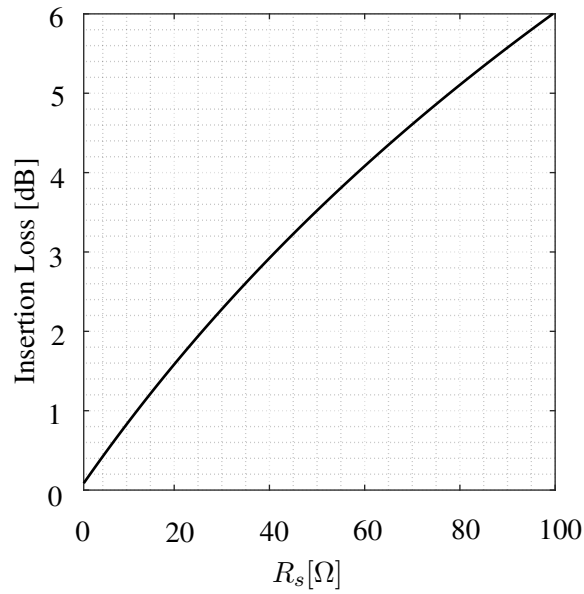
Figure 3.11: Curve of isolation and insertion loss value of the PIN diode for $R_s = 8 \Omega$, $C_T = 0.03 \text{ pF}$ and $Z_0 = 50 \Omega$.



Source: Own autorship.

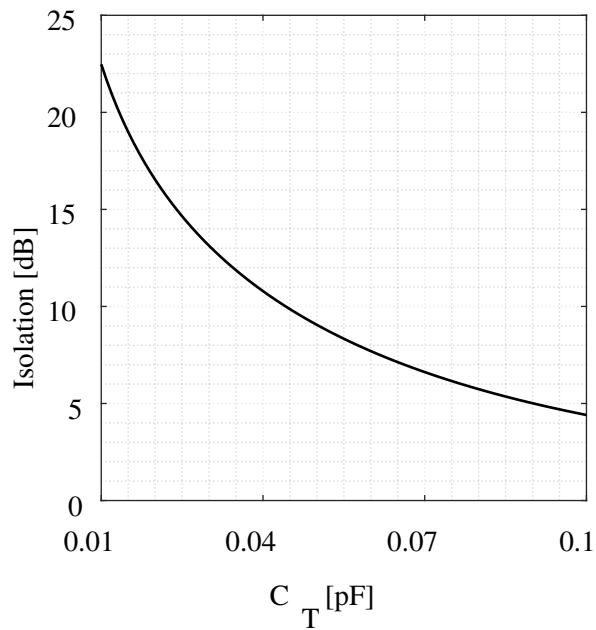
The isolation relies on frequency, the characteristic impedance, and the total capacitance, when reversely biased, and tends to decrease when this last one increases. Figure 3.13 displays the achieved isolation when the total capacitance is varied.

Figure 3.12: Curve of insertion loss of the forward biased PIN diode for a $C_T = 0.03$ pF, $Z_0 = 50 \Omega$ and $f = 12$ GHz.



Source: Own autorship.

Figure 3.13: Curve of isolation of the reverse biased PIN diode for $R_s = 8 \Omega$, $Z_0 = 50 \Omega$ and $f = 12$ GHz.



Source: Own autorship.

Allied to the slot dipole antenna, this element is used to create to construct a metasurface antenna, to implement beamforming using the holographic technique.

3.7 METASURFACE ANTENNAS

Metamaterials are composite materials manufactured to provide unconventional electromagnetic properties, such as artificial magnetism and negative refractive index (SMITH; PENDRY; WILTSHIRE, 2004). In these materials, the electric permittivity and magnetic permeability are determined by the periodic distribution of resonant elements smaller than one wavelength (KYMETA, 2019). Metasurfaces are 2D metamaterials, which are simpler to manufacture, due to the small dimensions of these structures. These metasurfaces have the ability for blocking, absorbing, concentrating, dispersing and guiding waves, by controlling the surface wave with an appropriate cell design. The effective surface refractive index can be adjusted by controlling the size and shape of the metasurface cells (LI; SINGH; SIEVENPIPER, 2018). In literature, these metasurfaces find place in applications such as impedance surfaces (SIEVENPIPER et al., 1999; FERESIDIS et al., 2005; HASHEMI et al., 2013), absorbers (CHENG; YANG; XIAO, 2011; ZHU et al., 2010; RADI; SIMOVSKI; TRETYAKOV, 2015), wavefront engineering (EPSTEIN; WONG; ELEFThERIADES, 2016; LEE; SIEVENPIPER, 2016), Metasurface Antennas (MSA) (SIEVENPIPER, 2005; CALOZ; ITOH; RENNINGS, 2008; MOROTE; DIAZ; CARRIER, 2014), modulators and polarizers, (PFEIFFER; GRBIC, 2013b; PFEIFFER; GRBIC, 2013a; CHEN et al., 2009), cloaking and stealthing (FLEURY; MONTICONE; ALÙ, 2015; SOUNAS; FLEURY, 2015), plasma generation (SINGH; HOPWOOD; SONKUSALE, 2014), planar lenses (BOSILJEVAC et al., 2012; KHORASANINEJAD et al., 2016), and imaging (LIPWORTH et al., 2013; HUNT et al., 2014).

3.7.1 Examples of Commercial Metasurfaces Antennas

Currently, exists a great number of companies working with holography, and more in general, with reconfigurable MSA as Commercial of The Shelf (COTS) products. Just to name a few, one can list Pivotal Commware and Kymeta.

Pivotal Commware uses HBF in its products, using a MSA with resonant elements adjusted by varactors. In its products are including indoor and outdoor 5G repeaters, drone beamforming antenna systems, and beamformers, using customizable antennas from 1 to 70 GHz. The manufacturers state that its electronically scanned array technology is the most C-SWaP. Its antenna works like a Software-Defined Antenna, controlling the beam shaping adjusting the impedance pattern of the array, through the varactor biasing, and then creating an appropriate hologram related to the desired object wave. The varactor controls how much energy leaks from the transmission line to the free space, using a DC bias signal. Pivotal replaces phase shifters, amplifiers, ADC/DAC, and DSPs used in PAA and MIMO by one varactor per antenna element, optimizing the C-SWaP of the antenna.

Kymeta uses a diffractive MSA allied to the holographic procedure to create the electromagnetic beam. The reconfigurability of this antenna is achieved by tuning the resonance of the scattering elements. In its technology, the elements that are in phase with the desired scan angle

wavefront are tuned to scatter the guided mode strongly, in the free space. Nonetheless, those that are out of phase are detuned (KYMETA, 2019).

To tune the scatter elements, a Liquid Crystal Display (LCD) material is used. This material can be manufactured by LCB industries established in the fabrication of televisions and smart-phones (KYMETA, 2019). The scatter elements are placed above this LCD. Electrodes connected in the LCD structure are destined to as conductor medium to an AC signal that creates an electric field over the LCD. These electric fields change the molecular orientation of the LCD, thus, modifying the relative permittivity of the LCD, changing its resonance point (STEVENSON et al., 2016).

Another company that uses LCD permittivity control in its antennas is Alcan Systems. Alcan achieves a cost reduction greater than 100 times from the conventional phased array.

3.7.2 Developing of Metasurfaces Antennas

YURDUSEVEN et al. (2017) presents a reconfigurable MSA for near-field focusing using PD. In its antenna, the radiating elements are slots antenna, and the feed system is a coaxial monopole. In his works the holographic procedure is used to define desired radiation pattern, the Hankel function is used as an estimation for the reference wave. Additionally, a phase threshold is used to calculate the hologram. In (YURDUSEVEN; SMITH, 2017) a dual-polarization printed MSA is designed and measured. In its work two types of slots are superposed, the vertical and the horizontal, to hold on to the two polarizations. The holographic procedure is used to calculate the positions where the slots will be, in the cavity, according to a phase threshold. In this work, the Hankel function is used as a guided-mode reference. Moreover, a multi-beam capability is also exploited, superposing the three different holograms to create three different beams simultaneously in the space. Other works that deal with holographic procedure are (CERVENY; FORD; TENNANT, 2017; ZHANG et al., 2019; LI; CUI, 2015; EBADI; DRISCOLL; SMITH, 2013; RAMALINGAM; BALANIS; BIRTCHER, 2018; YURDUSEVEN et al., 2017; RUSCH et al., 2015)

Another way to calculate the shape and direction of the beam is by calculating the artificial impedance of the array surface. Fong et al. (2010) presents a procedure to calculate scalar and tensor surface impedances. In this work, the impedance is adjusted by changing the area of the patch at the surface. To analyze the possible impedance values a patch cell is simulated using a FEM solver and high-order Nystrom discretization frequency-domain integral equation solver, varying the gap between the patches. These values are then registered in a possible impedance lookup-table. To calculate the desired impedance surface is defined as the real part of the interference between the surface wave under the array and the desired radiation pattern. Furthermore, a modulation index and an average constant are incorporated in the artificial impedance surface equation to tailor the beam according to the antenna size. Then, these impedance values are confronted in the lookup-table to define the gap for each patch in the antenna array, to assign the desired artificial impedance at the surface antenna. This procedure is used for the scalar case. In the ten-

sor case, a slice with a variable angle is tailored. All these procedures are performed in X-band. Many other references use this approach also to exploit beam shaping in metasurfaces, discussing about multi-beam capability, polarization control, wavefront control, reconfigurable antennas, metasurface lenses and more (PANDI; BIRTCHEV, 2015; PANDI; BALANIS, 2014; LI; CAI; CUI, 2014; LI et al., 2016; ZHANG et al., 2018; LI et al., 2014; MOVAHHEDI; KARIMIPOUR; KOMJANI, 2019; TAN; JI; LI, 2015). Lipworth et al. (2016) uses a similar procedure in W-band. Lipworth et al. (2016) uses a set of complementary meander lines with different lengths, where each length has a specific resonant value associated, to create a hologram to scatter complex beam shaping waves.

Some references make beamforming in modulated MSA calculating the interaction between the reference surface wave and the impedance boundary condition (FAENZI GABRIELE MINATTI; MACI, 2019; BODEHOU et al., 2019; MINATTI et al., 2015; MINATTI et al., 2016; MACI et al., 2011; OVEJERO; MACI, 2015). These structures are modulated to be locally periodic, and when the reference surface scatter at this lattice it radiates to the free space due to the leaky wave effect (FAENZI GABRIELE MINATTI; MACI, 2019). This technique consists of varying the size of the cell changes its resonance, but now modeling the surface like a sheet anisotropic impedance boundary condition. In these applications, a common way to feed the MSA is by using a coaxial monopole launcher.

Other approaches lead with tunable impedance surfaces, using the lumped LC circuit models of the tuning elements or the geometry and physical placement of the conductors to estimate the impedance of the surface (SIEVENPIPER et al., 2002; SIEVENPIPER et al., 2003; VIGANO et al., 2014; YU et al., 2018; LIM; CALOZ; ITOH, 2015).

This structure permits the creation of antennas that can modify their radiation pattern. However, an additional method can be used to enhance the performance of this antenna. Convex optimization can be an ideal tool for this purpose, as explained in the next section.

3.8 CONVEX OPTIMIZATION

3.8.1 Convex Optimization Background

The optimization procedure searches for an optimal solution to correct the undesired characteristics of the radiation pattern achieved with the holographic procedure.

The general formulation of an optimization problem is described below

$$\text{minimize } f_0(x) \quad (3.51a)$$

$$\text{subject to } f_i(x) \leq b_i, \quad i = 1, \dots, m. \quad (3.51b)$$

In this formulation, $x \in \mathbb{R}^n$ is the variable under optimization, $f_0 : \mathbb{R}^n \rightarrow \mathbb{R}$ is the objective function, $f_i : \mathbb{R}^n \rightarrow \mathbb{R}$ are the constraint functions, and b_i are the bounds for these constraints (BOYD; VANDENBERGHE, 2004). m is the number of constraints and n is the number of variables to be optimized. A convex optimization problem is a set of problems where the objective and constraint functions are convex, i.e., all functions in the formulation of the problem satisfies the following condition:

$$f_i(\alpha x + \beta y) \leq \alpha f_i(x) + \beta f_i(y), \quad i = 0, \dots, m, \quad \alpha + \beta = 1, (\alpha, \beta) \geq 0. \quad (3.52)$$

Once the problem is written as a convex one, it will always achieve the global minimum.

3.8.2 Problem To Be Optimized

The phenomenon to be optimized is the shape of the desired radiation pattern. A description of this phenomenon is expressed in

$$AF(\theta, \varphi) = \sum_{m=1}^M \left[\sum_{n=1}^N X_{N \times M} e^{j\vec{H}(\vec{\rho})} e^{jk\vec{\rho}_{mn} \cdot \hat{r}(\theta, \varphi)} \right], \quad (3.53)$$

$$\forall (\theta, \varphi) \in \mathbb{R}^2 | \theta \in [0, \pi], \varphi \in [0, 2\pi), \quad (3.54)$$

where $X_{N \times M}$ is the mask array and it is a sparse matrix by nature, and $H(\vec{\rho}_{mn})$ is the array of phases in the cavity. Once each element in $X_{N \times M}$ represents a state of one antenna in the array, the elements can assume 0 or 1, as values.

In other words, the optimization procedure will discover which element can contribute to the desired field, considering the position of the element and its associated cavity phase.

A conventional approach for this type of formulation is minimize ℓ_p norm⁵ of this mask $X_{M \times N}$, to optimize the array factor of the antenna. Usually the ℓ_0 norm is the preferred, once its minimization brings sparse solutions. However, the ℓ_0 norm is non-convex. Hence, this formulation can not be used. For this reason, the objective function is reformulated using the ℓ_1 norm, for matrices, (FUCHS, 2012). Observing these considerations, the optimization problem can be written as below:

$$\text{minimize} \quad \|X_{N \times M}\|_1 \quad (3.55a)$$

$$\text{subject to} \quad |AF(\theta, \varphi) - D_f(\theta, \varphi)| \leq \varepsilon(\theta, \varphi), \quad (3.55b)$$

where $D_f(\theta, \varphi)$ is the expression for the desired far-field and $\varepsilon(\theta, \varphi)$ is the acceptable error. Minimize ℓ_1 also generates sparse solutions, as described in (FUCHS, 2012), but does not restrict the solutions to be a binary array. For this reason, a convex optimization of binary variables must be used, to ensure an ON-OFF functionality. Some commercial solvers such as Gurobi, Mosek, GLPK, CPLEX can handle binary variables naturally, just to name a few (GUROBI, 2021; JUPYTER, 2021; GNU, 2012; MAKHORIN, 2016; IBM, 2019).

To solve this restriction an approach as used by Fuchs e Rondineau (2016) can be used. In this formulation, a combination of ℓ_1 and ℓ_∞ norms, for matrices, are used. The minimization of ℓ_∞ norm limits the range of values of the objective function. The formulation used by Fuchs e Rondineau (2016) is presented in

$$\text{minimize} \quad \|X_{N \times M}\|_1 + \gamma \|X_{N \times M} - \alpha\|_\infty \quad (3.56a)$$

$$\text{subject to} \quad |AF(\theta, \varphi) - D_f(\theta, \varphi)| \leq \varepsilon(\theta, \varphi). \quad (3.56b)$$

The scalar α is used to force the range of possible values. If α os equals 0.5, lead the solutions to be between 0 and 1. The parameter γ is used to define the reason between sparsity and binary and must be adjusted.

The shape of this field has as a first approximation the outcome of the holographic procedure. For this reason, instead of optimizing $X_{N \times M}$, the auxiliary variable $A_{N \times M}$ will be used, to incorporate this approximation:

$$A_{N \times M} = M_{N \times M} + |(M_{N \times M} - \mathbb{1}_{N \times M})| \circ X_{N \times M}, \quad (3.57)$$

where, $A_{N \times M}$ is the auxiliary variable, $\mathbb{1}$ is a matrix where all the elements are equals to 1, \circ is the Hadamard product, and $M_{N \times M}$ is the mask resultant from the holographic procedure, that can assume just binary values.

⁵In this case, the ℓ_p norms are matrix norms.

Thus, the resulting expression for the far field is presented below

$$AF(\theta, \varphi) = \sum_{m=1}^M \left[\sum_{n=1}^N A_{N \times M} e^{j\vec{H}(\vec{\rho}_{mn})} e^{jk\vec{\rho}_{mn} \cdot \hat{r}(\theta, \varphi)} \right]. \quad (3.58)$$

One more technique that can be used to enhance the performance of the antenna is the use of a bandpass filter at the antenna input, to limit the noise at the system.

3.9 COUPLED OPEN-LOOP RESONATOR FILTERS

A Band Pass Filter (BPF) must be added to avoid out-of-band signals to be received by the MSA. This BPF must exhibit a high-quality factor, to attenuate efficiently the non-desirable signals. The implementation of this filter can be made over microstrip technology, over PCB technology.

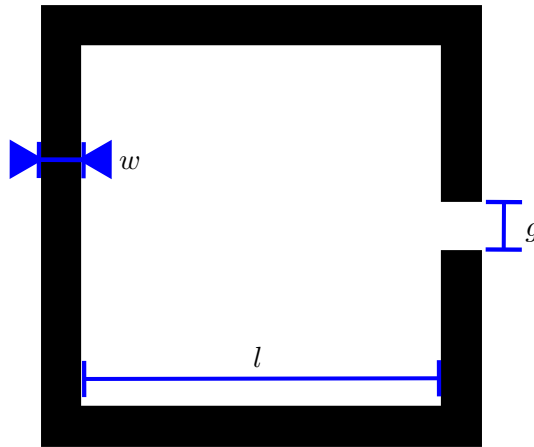
The filter topology to be exploited here is the Coupled Open-Loop Resonator (COLR) BPF.

3.9.1 Coupled Open-Loop Resonator Cells

A resonator is a device that has the capability to store electric and magnetic energy at the same quantity, in a resonant frequency (KUESTER, 2021). The quality factor is the quantity that measures the ratio between the stored to lost energy, and due to the low loss of these resonators, they possess a high-quality factor required to the proposed filter (RIZZI, 1987).

The resonator generally has half-wavelength and can be made over different geometries. In this work, the Square Open-Loop Resonator (SOLR) is employed, once its geometry is easy to adjust and its calculation is well established in the literature (HONG; LANCASTER, 1995). Figure 3.14 shown the proposed geometry.

Figure 3.14: Basic square open-loop resonator microstrip cell. In this cell w is the width of the microstrip line, l is the length of the square side, and g is the gap of the open-loop.



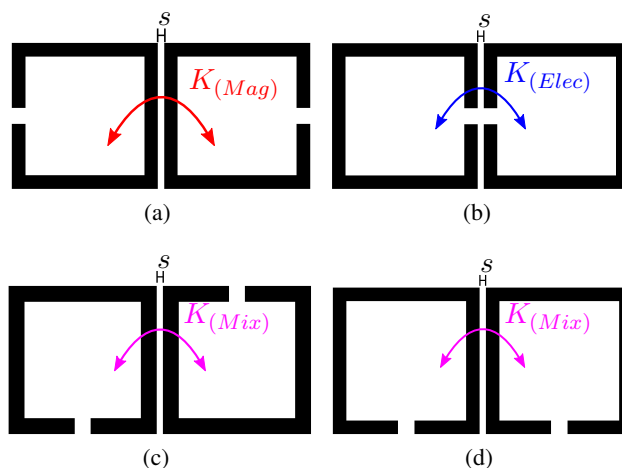
Source: Reproduced from (SANTANA; BARBOSA; RONDINEAU, 2020).

To construct COLR BPF using the SOLR cell, these cells must be arranged in different configurations. When a pair of resonators are placed together their fringing fields get coupled. This coupling between the pair of resonators works as the path to microwave signal travel, in a specific resonant frequency. The intensity of this fringing field coupling can be measured by the coupling coefficient, which is a ratio between the coupled to the stored energy (HONG, 2000).

For the SOLR the main coupling configurations are depicted in Fig. 3.15. The main coupling

mechanisms are electric, magnetic, and mixed-coupling. Figure 3.15a depicts the configuration where the coupling density is mainly composed of magnetic fringing fields. On the other side, the configuration presented in Fig. 3.15b shows when the electric field is the principal component of the coupling. The other two configurations are called mixed-coupling because the magnetic and electric fringing field contributions are at the same level (HONG; LANCASTER, 1995).

Figure 3.15: Different coupling mechanisms for different arrangement of square open-loop resonators. (a) Magnetic coupling. (b) Electric coupling. (c) Mixed coupling - Type 1. (d) Mixed coupling - Type 2.



Source: Reproduced from (SANTANA; BARBOSA; RONDINEAU, 2020).

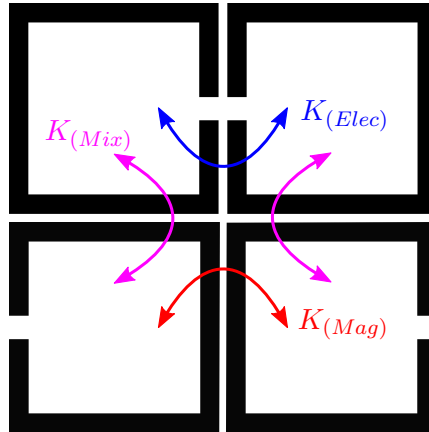
3.9.2 Coupled Open-Loop Resonator Band-Pass Filter

To construct a BPF using the SOLR cell is necessary to use an array with three different coupling mechanisms. Hong e Lancaster (1995) presents an COLR array configuration using SOLR that is presented in Fig. 3.16. This configuration uses electric, magnetic, and mixed-coupling of the first type.

The routine to design this filter is stated in Hong e Lancaster (2001) and briefly summarized in Santana, Barbosa e Rondineau (2020). The procedure is presented in the following topics:

- Calculate lowpass prototype impedances of the filter;
- Calculate the external quality factor according to the lowpass prototype impedances;
- Calculate the coupling coefficient matrix according to the lowpass prototype impedances to each pair of resonators;
- Extract the distance between the coupled resonators related to each coupling coefficient using electromagnetic software simulator. This task is performed doing a parametric simulation over the gap between the two coupled resonators;
- Design the COLR filter array.

Figure 3.16: Coupled Open-Loop Resonator Band-Pass Filter arrangement.



Source: Reproduced from (SANTANA; BARBOSA; RONDINEAU, 2020), using the filter architecture presented in (HONG; LANCASTER, 1995).

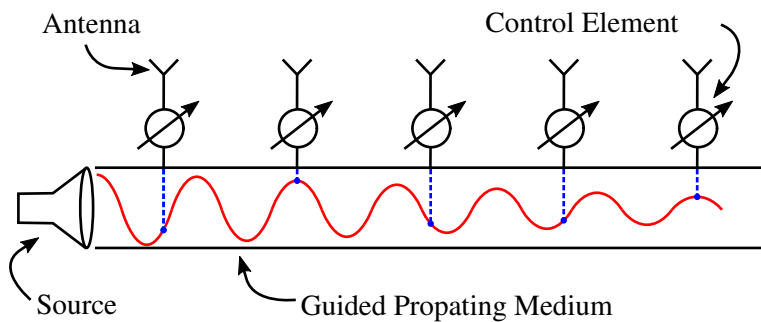
Finally, all the elements and techniques required to present the proposed antenna are already shown, and the result is summarized in the next chapter.

4 DESIGN OF HOLOGRAPHIC METASURFACE ANTENNA

4.1 METASURFACE ANTENNA STRUCTURE

The basic structure of a MSA is depicted in Fig. 4.1. The structure contains an electromagnetic source, a propagating medium, an antenna cell and a, non-mandatory, control element, which can change the resonant state, impedance, or, more generally, the radiation capability of the antenna cell.

Figure 4.1: Basic structure of a Metasurface Antenna. The main elements of this structure are the antenna cell, the guided propagating medium, the electromagnetic source and a control element. The source illuminates the medium and each antenna scatter to the space a different contribution of this wave, according with its position and the state of the control element.



Source: Own autorship.

However, if the MSA contains a control element it can work as a Reconfigurable MSA (RMSA), without the use of one radio, phase shifter, or amplifier for each antenna. The source illuminates the propagating medium with a specific and known electromagnetic field, this field is then scattered by the antenna elements to space. Each antenna samples a different point of the electromagnetic field, with a distinct phase, amplitude, and position, and then irradiating a particular wave-front to space. With the control element, the MSA can manipulate the contribution of each antenna, decreasing the scattering level, changing the phase, or even avoiding the antenna to irradiate with the others.

An MSA can make use of any technique of array factor synthesis, and then controls beam direction, beamwidth, polarization, sidelobe level, phase, or, more generally, the shape of the radiated wave.

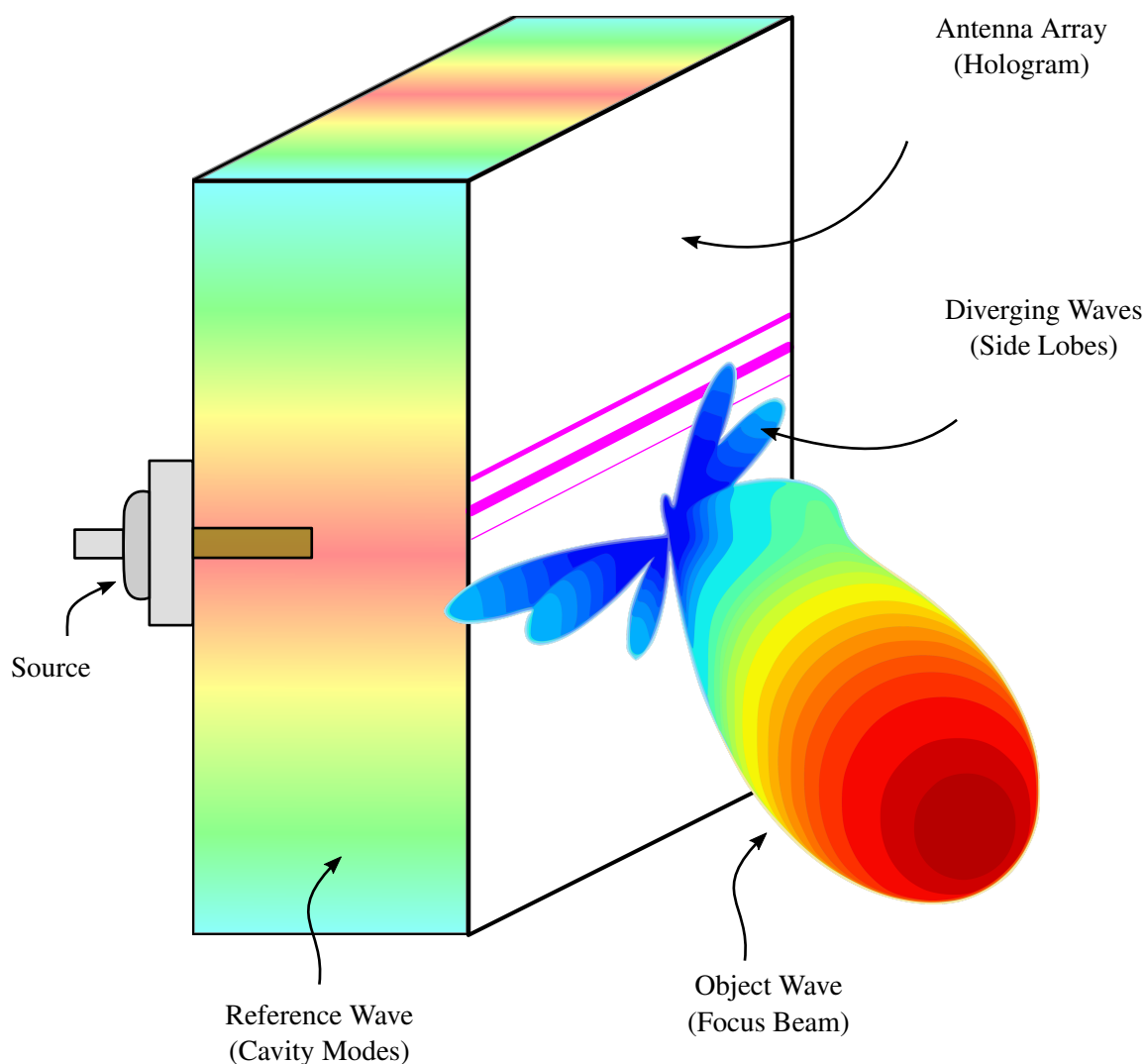
4.2 HOLOGRAPHIC METASURFACE ANTENNA

To use the holographic procedure in an antenna this one must be able to record the hologram on its surface. Considering the MSA structure presented previously, the hologram can be recorded

over the antenna array adjusting the radiation level of the cell. In this way, each antenna works as a pixel of the hologram.

Figure 4.2 shows the implementation of the holographic procedure in an MSA for a beam direction application. In this example, the propagating medium is a parallel plate dielectric, the electromagnetic source is a coaxial probe, which is essentially a monopole launcher, and the recording layer is the antenna array. In this case of application, the reference wave is the guided-mode in the cavity created by the monopole launcher. On the other side, the object wave can be achieved by projecting the desired focus beam over the aperture. The interference pattern can then be calculated with these two surface waves.

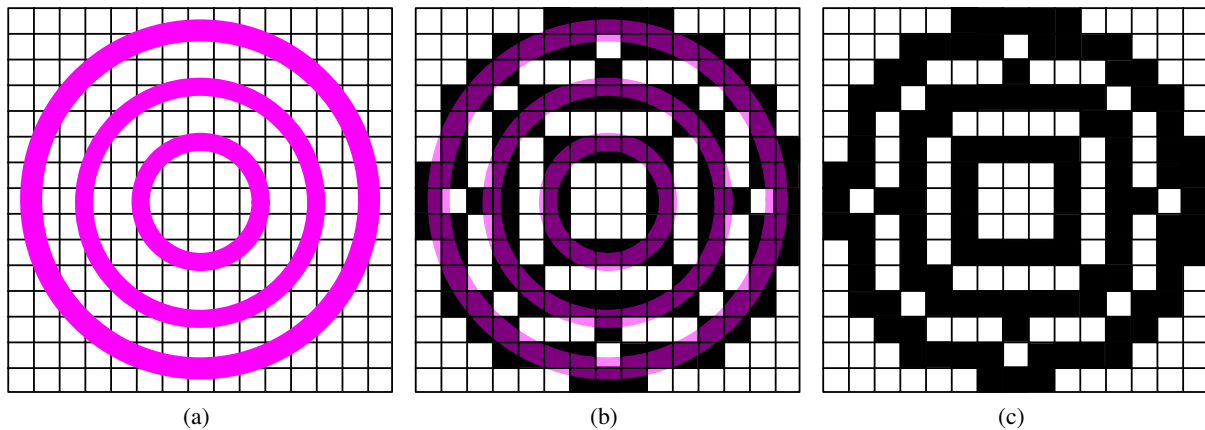
Figure 4.2: Example of how to use the holographic technique in an antenna array. The recording process is performed using the electromagnetic modes created in the cavity by the source (In this case, a coaxial monopole) and the projection of the desired beam over the array. The generated interference pattern is used to change the resonant state of the antennas. The reconstruction process occurs when the reference wave scatters in the recorded hologram in the antenna array.



Source: Own authorship.

To turn this structure into a RMSA is necessary to add some control element to manipulate the resonant point of each antenna. This element can act over the cell discretely, like an ON-OFF, or continuously, changing gradually the intensity of radiation of its attached antenna. Figure 4.3 consider a binary control, where the cell irradiates or no, and depicts the process to record the hologram in the antenna array.

Figure 4.3: Hologram recording over the antenna array. In the example a 15×15 rectangular lattice is used with an arbitrary interference pattern. (a) Interference pattern over the antenna array. (b) Projection of the interference pattern in the array. (c) Recorded hologram in the antenna array.



Source: Own authorship.

In Figure 4.3a, an arbitrary binary interference pattern is projected over the antenna array. The magenta circles illustrate the fringes of the interference pattern. In figure 4.3b, each square represents an antenna or pixel of the hologram, that is black colored when the cell is radiating, and white, when not. Thus, when the antenna is over the fringe, it is set to radiate and so can scatter the reference wave to space. In Figure 4.3c the hologram is already recorded in the RMSA. Immediately, is possible to notice that the length of the array impacts the resolution of the hologram and, hence, the quality of the reconstruction.

4.3 HOLOGRAM RECORDING PROCEDURE FOR ARBITRARY GUIDED-MODES

A simple procedure that can be carried out to acquire the reference wave is to simulate the structure of Fig. 4.2 in a Full-Wave electromagnetic software. Despite being a procedure that demands a high level of computational resources and takes a long time of simulation, if, in comparison with analytical methods, this procedure can work for any shape of the cavity, and even if containing field disturbing elements, such as through-hole vias, mechanical holes or slots in the conductor layers. Additionally, this procedure must be performed just one time. Then, the fields over the antenna array are extracted and recorded to be later used as a reference wave.

YURDUSEVEN et al. (2017) presents a procedure to calculate the object wave putting a point source in far-field, in the desired direction and then projecting its fields over the antenna array. Another way to calculate this wave is by using the equation of array factor synthesis for the

desired pointing direction.

Smith presents a procedure to calculate the hologram using just the phase of the magnetic field, once this parameter primarily governs the shape of the beam. Anymore, the author demonstrates that calculating the hologram, in this case, is enough to establish a phase difference threshold. Using this procedure, when the object and reference wave differ in a level below the phase threshold, the antenna under this point is allowed to irradiate. Notwithstanding, if this level is greater than the antenna is adjusted to the OFF state. In other words, if the phase of the reference wave is similar to the object wave at some point, the antenna in this position is permitted to influence the creation of the radiation pattern.

4.4 PROPOSED METASURFACE ANTENNA

The proposed RMSA uses a Parallel-Plate Waveguide (PPW), as a guided-medium, slot antenna as radiating cell, PIN diode, as control elements, and coaxial monopole connector as an electromagnetic source. Each part of the RMSA is detailed in the next sections

4.4.1 Antenna cavity

The cavity consists of a Parallel Plate Waveguide (PPW), which is a double copper layer dielectric laminate. To optimize the radiated power efficiency a short circuit is placed at the limits of the PPW, using metallic through-hole vias. If the distance of the vias is smaller than $\lambda_0/12$, as used in grid-wire corner reflectors (BALANIS, 2005), the wall of vias behaves like a PEC wall. Due to this, all the walls of the PPW acts like PEC. This type of PPW can be entirely manufactured using PCB techniques under common manufacturing standards tolerances (IPC STANDARDS, 2016). The dielectric laminate must have a small loss tangent, to diminish the losses over the cavity and permits that the signal can travel through all PPW dimensions and scatter in all slots. The dielectric constant must be as lower as possible, once it affects the guided wavelength. If the wavelength were too much small, fabricate $\lambda_g/2$ slots could be a problem due to the manufacturing resolution tolerances, even more for high frequencies. Additionally, the laminate thickness must be lower than 70 % $\lambda_g/2$, as a conservative choice, to avoid the creation of modes in this dimension, ensuring the creation of a transverse magnetic mode in the array plane at cavity (BALANIS, 2012). Finally, this PPW is the medium where the guided-wave must travel and must have an area with dimension such creates a great phase distribution, to improve the scanning capability of the system.

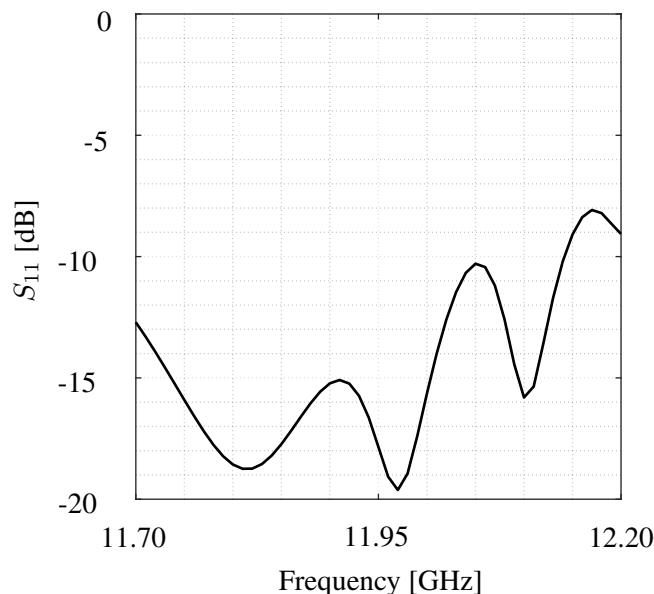
4.4.2 Coaxial Monopole Launcher

The excitation of the cavity is composed of a coaxial monopole antenna, approximately $\lambda_0/4$, and a SMP connector. This coaxial-feed is placed at the center of the PPW in the bottom layer. This monopole is responsible to launch the reference wave into the PPW, as guided-

mode (PANDI; BIRTCHEV, 2015; FAENZI GABRIELE MINATTI; MACI, 2019; MACI G. MINATTI; BOSILJEVAC, 2011). Due to the symmetries and boundaries of the PPW, the phase of the magnetic field created by this launcher will be symmetric in the x,y components of the magnetic field. This launcher inserts the power in the PPW that will scatter at the slots and radiate in free space creating the desired radiation pattern.

The impedance matching of the probe feed is depicted by the S_{11} parameter, depicted in Fig. 4.4.

Figure 4.4: S_{11} parameter at the input of the coaxial connector.



Source: Own authorship.

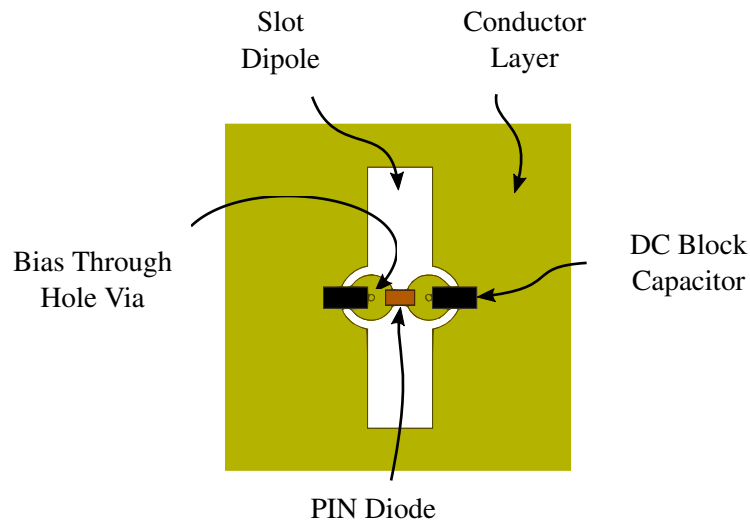
4.4.3 Antenna Element

This manuscript uses a Slot Dipole Antenna (SDA) cell as a basic element, very similar to the one used by (YURDUSEVEN et al., 2017). An antenna cell contains two capacitors, one PIN diode, two through-hole vias, one SDA, and two octagonal spiral microstrip lines inductors. Figure 4.5 shows the top view of the antenna cell. The length of the slot dipole measures $\lambda_g/2.5$ and its width is $\lambda_g/24$.

In the middle of the antenna cell a PIN diode, the control device, is placed. The two pads in the middle of the are provided to receive the bias signal from the bottom layer passing by the through-hole vias. The capacitors act like DC blocks, avoid the DC bias signal to short circuit with the other biasing signals.

Figure 4.6 shows the side view of the SDA cell. In this figure, it is possible to see the stack-up of the antenna, which uses 3 conductors layers and 2 dielectric cores. The first dielectric core is where the RF signal propagates and the second is used to draw the biasing elements. The top

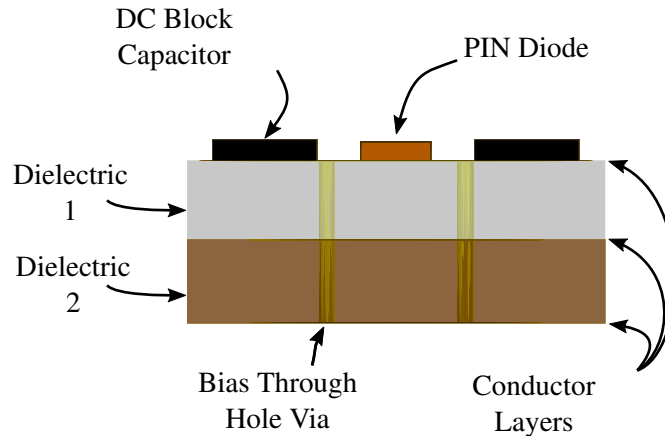
Figure 4.5: Top view of the active slot dipole antenna cell. The PIN diode works like a ON-OFF switch, changing the effective length of the slot. The capacitor acts like DC blocks to isolate the bias signal in the pads.



Source: Own autorship.

conductor is where the SDA is placed, the middle one is the GND plane, and the bottom is where the biasing elements are placed.

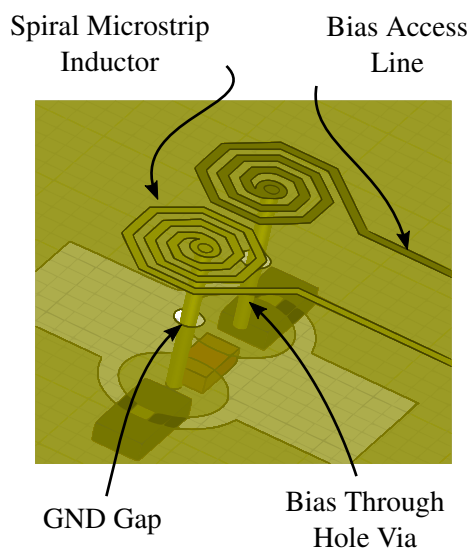
Figure 4.6: Side view of the active slot dipole antenna cell. The dielectric number 1 is the medium where the microwave signal propagates and the number 2 is dedicated to draw the bias circuit. The bias through-hole via is used to lead the bias signal from the bottom to the top layer.



Source: Own autorship.

Finally, Figure 4.7 presents a bottom view of the SDA cell. In this last layer, two octagonal spiral microstrip line inductors are used to reduce the microwave signal that could flow to the bias access line, working as an RF choke. In this picture is also possible to see the gap in the GND to the bias through-hole via pass without causing a short circuit in the GND.

Figure 4.7: Bottom view of the active slot dipole antenna cell. The bias through-hole via is connected to the octagonal spiral microstrip line inductor.



Source: Own autorship.

4.4.4 PIN Diode Behavior

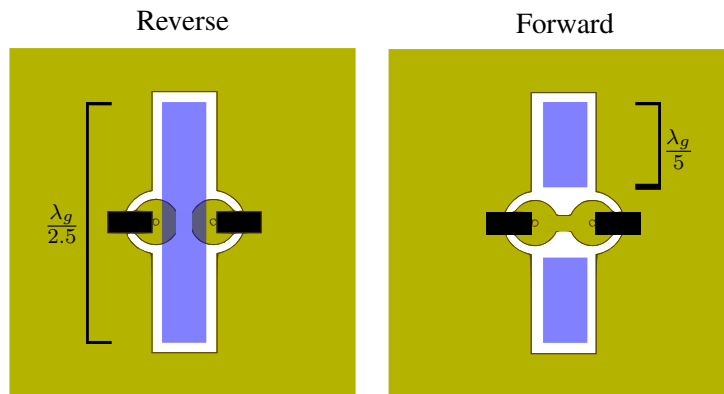
The PIN diode used as a control element work as an ON-OFF switch to the slot aperture. The PD changes its behavior depending on its biasing state. When the PD is forward biased, it can be modeled as a small resistance in series with a parasitic inductance. However, when reverse biased the PD equivalent impedance can be seen as a shunt RC in series with a parasitic inductance. Due to this, when forward biased the PD presents a low-impedance path to microwave signals, while when reverse biased presents a high-impedance path to this same signal.

Proceeding with this idea, the high-impedance state block the microwave signal to pass through the PD. This signal is a surface current in the PPW due to the guided mode. On the other side, the low-impedance state permits that microwave AC current flows through the PD.

Thus, the high-impedance slightly interferes with the scattering properties of the slot, which can be seen as an ON state. Nonetheless, the current flowing through the SDA decreases the radiation capability of the cell and, in a simplified manner, the SDA can be considered in an OFF state, once its effect in the final radiation pattern is considerably attenuated. The effects of the current flowing in the slot are such that the SDA works as two sub-slots, measuring $\lambda_g/5$, a length that provides a poorly radiation efficiency. Figure 4.8 depicts a representation of this behavior.

In practical implementations, the PD must have small series resistance, to provide a low insertion loss to the surface microwave current at the forward state, and a small junction capacitance, to create high isolation between the slot aperture sides at the reverse state. For the desired frequency of application, a small value of series resistance is until 5 or 10 Ω , and acceptable junction capacitance values are around 0.03 pF. Moreover, the PD must also have a small dimension, to fit correctly the slot aperture, some length between $\lambda_g/12$ and $\lambda_g/24$.

Figure 4.8: PIN diode equivalent slot lengths for both reverse and forward bias state. During the reverse bias state the PIN diode does not create a low path impedance to the surface current, due to this the effective length of the slot is approximately $\lambda_g/2.5$, and then the radiation of the slot is maximized. During the forward bias state the PIN diode conducts the surface current, and then the effective length of the slot downs to $\lambda_g/5$, details that decrease its radiation efficiency



Source: Own autorship.

Table 4.1 presents some commercial PIN diodes part numbers and their respective parameters, at the desired frequency.

Table 4.1: Commercial PIN diodes at the desired frequency.

Part Number	Total Capacitance [pF]	Series Resistance [Ω]
MA4GP907	0.025	5.2
MA4FCP200	0.020	2.4
GC4800A	0.016	4.5
MA4AGBLP912	0.026	4

Source: Own authorship.

4.4.5 Spiral Microstrip Inductor

To solve the requirement of discrete inductors, which add costs, and the manufacturing process in antenna fabrication, a PCB microstrip inductor is proposed to be used as an RF choke at the PD bias line. To optimize the use of the antenna area, a spiral microstrip inductor is used around the bias vias. This element cannot cut the GND layer, consequently, a second laminate core must be added to the design to support a third copper layer. This will hold the bias signals, which are DC, essentially.

The function of the RF choke inductors is to attenuate the leakage of RF signals at the bias network terminals. For this reason, this second core can be a FR-4 laminate, which possesses a high loss at microwave frequencies, but is cheap and easy to process. Table 4.2 presents the layer stack of the antenna PCB.

Continuing with the RF choke design, the spiral type is chosen to be octagonal. The width of

Table 4.2: Antenna PCB's Layer Stack.

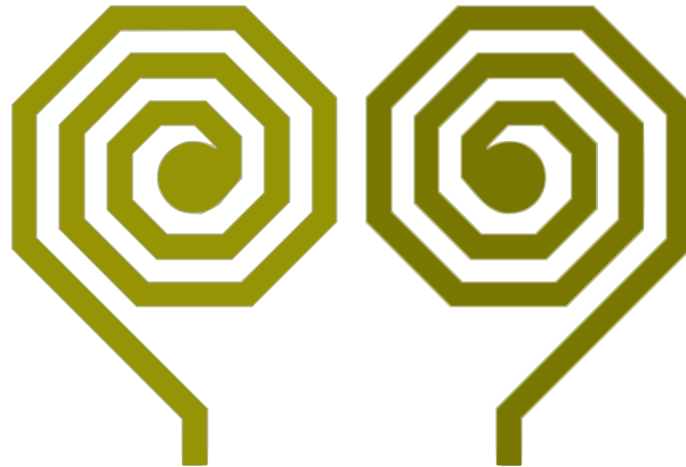
Layer	Type	Material	Thickness [μm]
1	Signal - RF	Copper	18
-	Core	AD450	3175
2	Signal - GND	Copper	18
-	Prepreg	Prepreg	-
-	Core	FR-4	800
3	Signal - Control	Copper	18

Source: Own authorship.

the inductor lines is defined by the manufacturing tolerances, and the number of turns is limited by the half distance between the anode and cathode bias vias. The octagonal microstrip inductor has a higher Self-Resonance Frequency (SRF) if compared to the rectangular and circular one. A great SRF creates a high impedance at high frequencies, which is useful to attenuate microwave frequencies (BAHL, 2003).

Mohan et al. (1999) presents some formulations to estimate the inductance of the octagonal spiral inductor, which is around 13 nH, for the proposed inductor. Figure 4.9 presents the design of the spiral microstrip inductor. This spiral inductor creates isolation greater than 15 dB, in the desired band.

Figure 4.9: Octagonal spiral microstrip inductor proposed as RF choke.



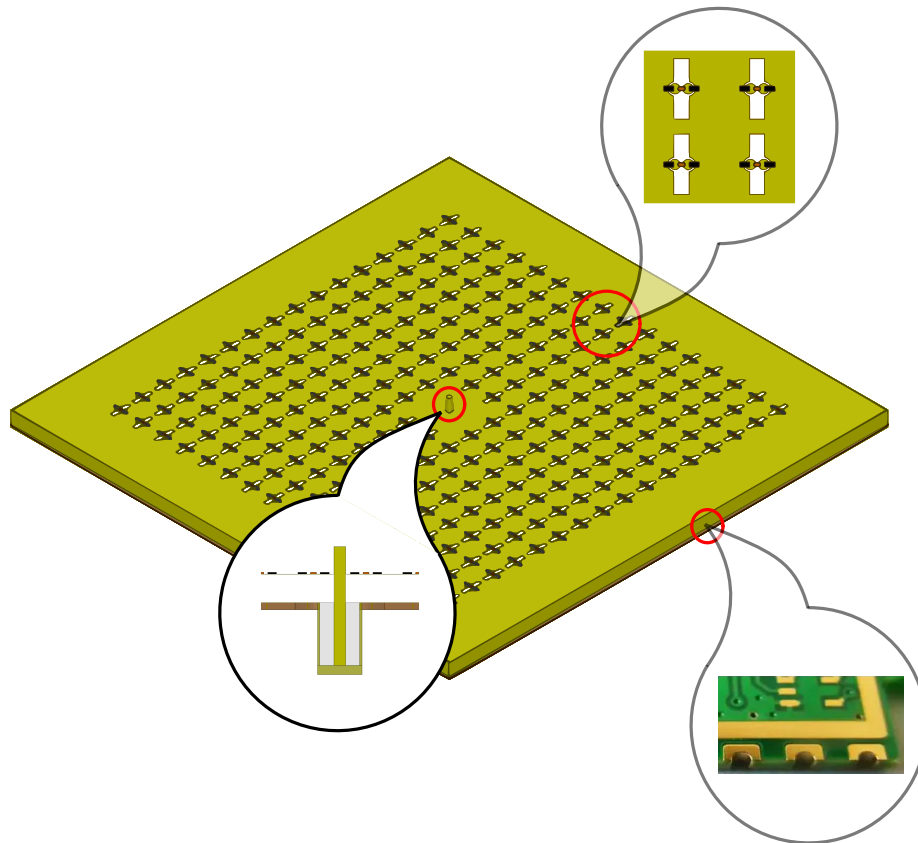
Source: Own autorship.

4.4.6 Antenna Array

The antenna array is 16×16 square lattices with a periodicity of $\lambda_g/2$. The cavity below the array measures $10 \lambda_g \times 10 \lambda_g$. The dielectric of the cavity is a 3.175 mm thickness AD450, $\epsilon_r = 4.5$ and $\tan(\delta) = 0.0035$, from Rogers Corp. The second core is FR4, once it is used to DC signals. This structure was simulated in HFSS to extract its fields, and its representation is

depicted in Fig. 4.10.

Figure 4.10: Isometric view of the metasurface antenna array.



Source: Own autorship.

4.4.7 Hologram Generation

A simple procedure that can be carried out to acquire the reference wave is to simulate the PPW model in Full-Wave electromagnetic software. Despite being a procedure that demands a high level of computational resources and takes a long time of simulation, if, in comparison with analytical methods, this procedure can work for any shape of the cavity, and even if containing field disturbing elements, such as through-hole vias, mechanical holes or slots in the conductor layers.

Additionally, this procedure must be performed just one time. Then, the fields over the antenna array are extracted and recorded to be later used as a reference wave.

[Yurduseven e Smith \(2017\)](#) presents a procedure to calculate the object wave putting a point source in far-field, in the desired direction and then projecting its fields over the antenna array. Another way to calculate this wave is by using the equation of array factor synthesis for the desired pointing direction. Smith presents a procedure to calculate the hologram using just the phase of the magnetic field, once this parameter primarily governs the shape of the beam. Anymore, the

author demonstrates that calculating the hologram, in this case, is enough to establish a phase difference threshold. Using this procedure, when the object and reference wave differ in a level below the phase threshold, the antenna under this point is allowed to irradiate. Notwithstanding, if this level is greater than the antenna is adjusted to the OFF state. In other words, if the phase of the reference wave is similar to the object wave at some point, the antenna in this position is permitted to influence the creation of the radiation pattern. This is summarized by the following equation, where ξ is the phase threshold:

$$\text{Pixel State} = \begin{cases} 1 \text{ (ON)}, & \text{if } \angle I \leq \xi \\ 0 \text{ (OFF)}, & \text{if } \angle I \geq \xi. \end{cases} \quad (4.1)$$

The structure was modeled in HFSS, using Finite Element Methods (FEM). An analysis in 12 GHz is used to evaluate the antenna pattern and cavity modes, a sweep frequency from 11.7 GHz to 12.2 GHz is also led to verify the impedance matching at the coaxial SMP connector.

4.4.8 Control Circuit

As a current-controlled device, the PIN diode must be biased with a controllable sink driver, to switch between the states of the ON-OFF states. The voltage between the anode and cathode terminals controls the state of the PIN diode and the DC current flowing in its body controls the insertion loss and isolation level. Typically, the higher the DC current the higher the isolation and lower the insertion loss.

To perform this operation the STP16CPC26 was used. This device is a 16-bit constant current LED sink driver, with a 16-bit shift register that converts serial input into a parallel output.

The current at the output ports can be adjusted using an external resistor. This current is the same for all the 16 ports of the device. Each output can be controlled individually, and for this reason, one device can be used to bias 16 PIN diodes. The sink driver footprint is depicted in Fig. 4.11.

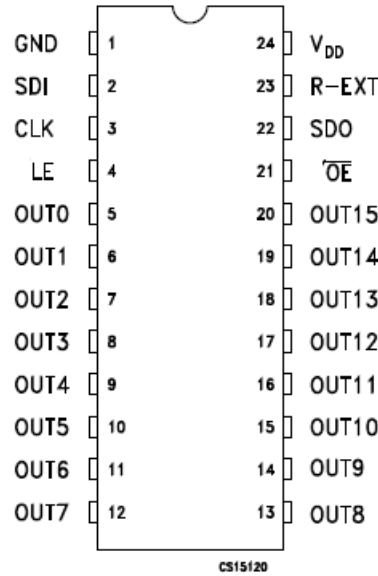
However, 16 ports are not enough to control a high-resolution antenna array. Therefore, more than one sink driver must be used simultaneously. This operation can be achieved using the Daisy chain configuration, as depicted in Fig. 4.12.

In this configuration, the current can be adjusted using the power divider of Fig. 4.13. The current in each channel can be calculated using

$$I_{CH}(n, R_{REG}, R_{SET}) = \left(1.25 - \frac{1.25 \cdot n \cdot R_{REG}}{n \cdot R_{REG} + R_{SET}} \right) \frac{16}{R_{SET}} \quad (4.2)$$

where I_{CH} is the channel current, n is the number of devices connected in Daisy chain configuration, R_{SET} and R_{REG} are the control resistances.

Figure 4.11: 16-bit constant current LED sink driver - STP16CPC26 pinout.



Source: (STMICROELECTRONICS, 2017).

The voltage at the output ports can be varied from -0.5 V to 20 V. An S-parameters simulation was performed in ADS to verify the switching behavior of the PIN diode. For this simulation, the PIN diode MA4GP907 of MACOM was used (MACOM, 2020). Its technical specifications and ADS model are described in Tabs. 4.3-4.4, respectively.

Table 4.3: MA4GP907 PIN diode technical specifications.

Parameter	Value
Total capacitance	0.025-0.030 F
Series resistance	5.2-7 Ω
Forward voltage	1.33-1.45 V
Switching Speed	2 ns

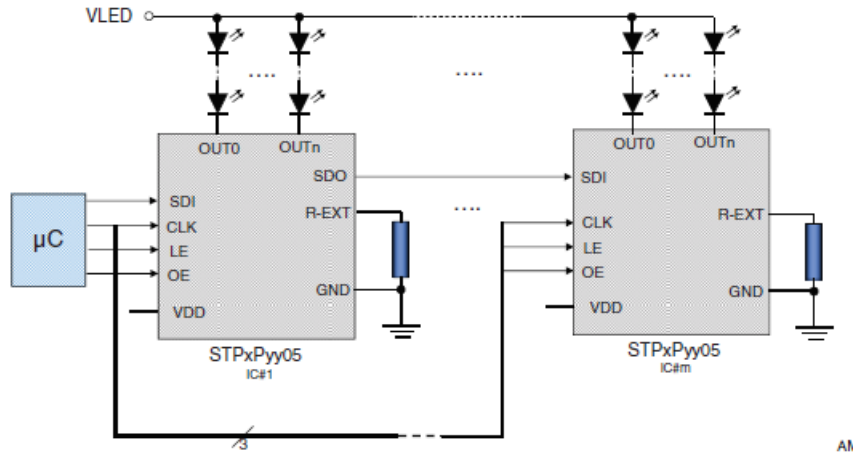
Source: Own authorship.

The circuit simulated is depicted in Fig. 4.14. In this circuit, a bias voltage of 5 V is connected at the anode of the PIN diode, and the drive voltage is connected at the cathode terminal. In the setup of the drive voltage, a sweep from -0.5 V to 20 V is performed, with the proper bias network.

The resultant S-parameter curves are shown in Fig. 4.15. In this curve, it is possible to notice that for drive voltages below 5 V the insertion loss is approximately zero, and after this limit, the isolation between the PIN diode terminals is greater than 15 dB. So, for a drive voltage below 5 V, the PD is forward biased and the SDA is at an OFF state. For values greater than 5 V, the PD is reverse biased and the SDA is at ON state.

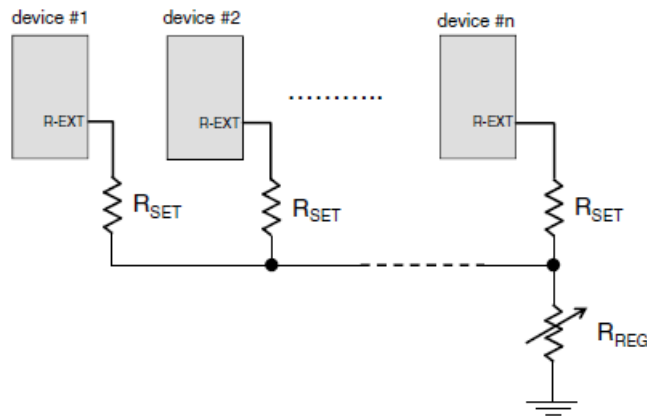
After this verification, a control circuit for 16×16 PIN diodes was designed, with 16 constant-current LED sink driver devices connected in Daisy chain configuration. The schematic, the PCB

Figure 4.12: Constant current sink drivers connected in Daisy chain configuration.



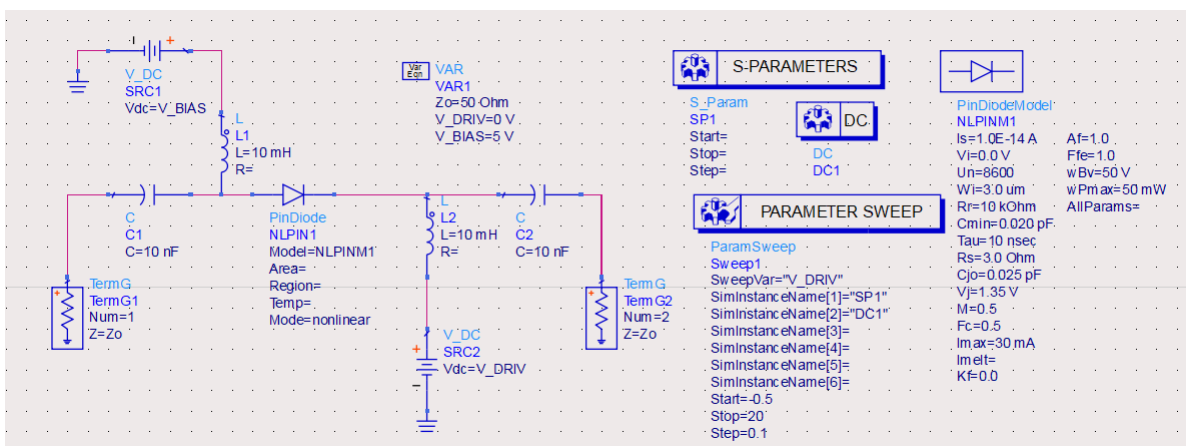
Source: (STMICROELECTRONICS, 2012).

Figure 4.13: Current control in Daisy chain configuration.



Source: (STMICROELECTRONICS, 2012).

Figure 4.14: MA4GP907 PIN diode bias circuit S-parameters simulation in ADS.



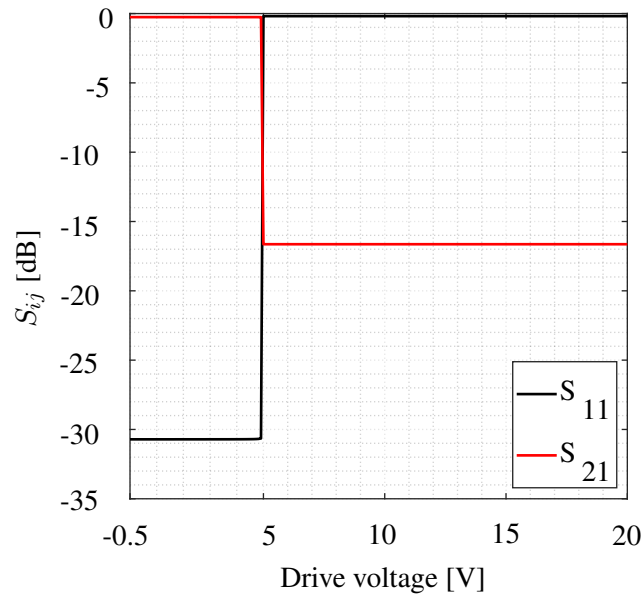
Source: Own authorship.

Table 4.4: ADS PIN diode model.

Parameter	Value
Saturation current	10^{-14} A
Electron mobility	$8600 \text{ cm}^2/(\text{V}\cdot\text{s})$
I-region width	$3 \mu\text{m}$
I-region reverse bias resistance	$10 \text{ k}\Omega$
P-I-N punchthrough capacitance	0.20 pF
Ambipolar lifetime within I-region	10 ns
Ohmic resistance	3Ω
Zero-bias junction capacitance	0.25 pF
Junction potential	1.35 V
Grading coefficient	0.5
Forward-bias depletion capacitance coefficient	0.5
Explosion current	30 mA
Diode reverse breakdown voltage	50 V
Maximum power dissipation	50 mW

Source: Own authorship.

Figure 4.15: MA4GP907 PIN diode switching behavior due to drive voltage sweep. In this figure, it is possible to distinguish the ON and OFF state in S-parameters curves.



Source: Own authorship.

layout, and the 3D view of this circuit is depicted in Ap. I.

Each device has an enable button to active just the necessary drivers to the antenna array. The R_{SET} and R_{REG} are a $1000\text{ k}\Omega$ resistor and a $200\ \Omega$ potentiometer. Thus, the output current can be adjusted between 4.7-20 mA. The tuning of the bias current can be used to control the insertion loss and isolation levels.

In the PCB layout design, the clock signal is adjusted to have the same length for all the drivers, to provide the same delay.

4.4.9 Power Supply

The main sources of power consumption are the PD biasing and the PD drivers. The sources to feed these systems are both 5 V. Additionally, an extra source of 3.3 V is also provided to be used, if necessary. The load map of the power supply is depicted in Tab. 4.5. The PD biasing consumes 3.84 A, considering an array of 16×16 elements. The PD drivers consume 240 mA, also for an array of 16×16 elements. The estimated current for general usage in 3.3 V is 300 mA. For all these sources, the total power consumption is about 21.39 W.

Table 4.5: Load map.

Load	Quantity	Typ. current	Max. current	Total current	Voltage	Total Power
PIN diode	256	10 mA	15 mA	3.840 A	5 V	19.2 W
Drivers	16	11 mA	15 mA	240 mA	5 V	1.2 W
General use	-	-	-	300 mA	3.3 V	990 mW
Total usage	-	-	-	4.38 A	-	21.39 W

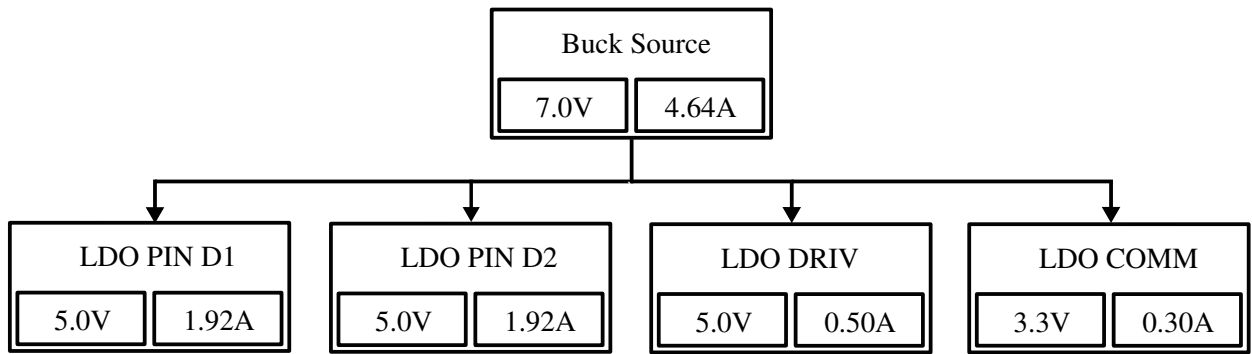
Source: Own authorship.

The power source map is depicted in Fig. 4.16. The main source is a buck converter, which is a step-down DC-DC converter. This circuit is more complex than a simple Low-DropOut regulator (LDO) but presents a high-efficiency behavior, which is necessary due to the high current value. The basic circuit of a buck converter is shown in Figure 4.17. The commutation between the ON-OFF states of the transistor determines the operation of the converter. During the ON state, the current passes through the inductor and the diode becomes reverse biased. During the OFF state, the current in the inductor can not change instantaneously, so the current continues to flow, decreasing its value, and the diode becomes forward biased (PRESSMAN, 1998).

The buck converter converts the input voltage from 12 to 7 V. This converter feeds the other four LDOs regulators. Due to the high current consumption of the PDs biasing two LDOs are necessary to divide this demand, since commercial LDOs regulators of reasonable price can not achieve high current values, as necessary for this application. The other two LDOs regulators are for the PD drivers and 3.3 V source.

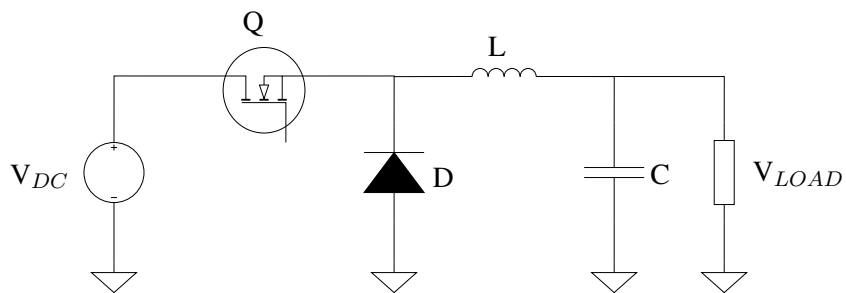
The schematic and PCB layout of these circuits is illustrated in Ap. II. The 3D view of the circuit is detailed in Figures II.1-II.2

Figure 4.16: Power source map.



Source: Own autorship.

Figure 4.17: Buck converter.



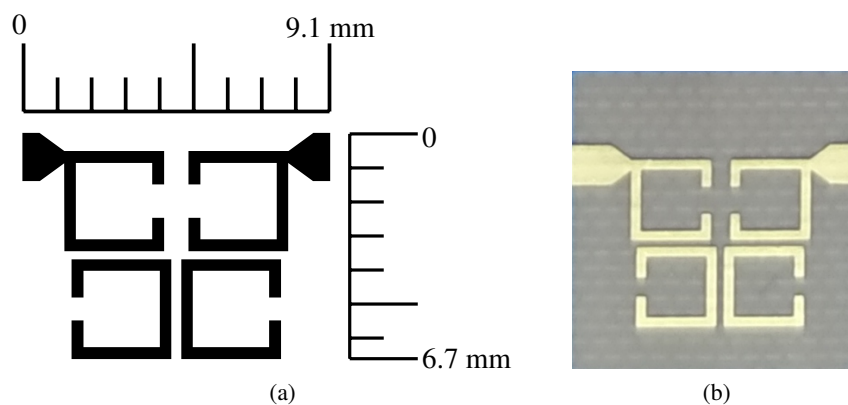
Source: Own autorship.

4.5 COUPLED OPEN-LOOP RESONATOR BAND-PASS FILTER

The Advanced Design System (ADS) was used to design the COLR BPF. The length of the SOLR was designed to be equal to half-wavelength at 11.95 GHz. The width of the transmission lines and the gap of the open-loop were chosen to be $200\ \mu\text{m}$, exhibiting a $130\ \Omega$ impedance. This width creates a better aspect ratio, at this frequency.

The parametric simulation was performed using the sweep parameter simulation at ADS. From this procedure, the gap between the coupled open-loop resonators is calculated. Then, the last optimization was done to improve the final performance of the filter. The final geometry and the filter area are depicted in Fig. 4.18a, the manufactured filter is shown in Fig. 4.18b. The dielectric laminate used was a 0.508 mm AD250C, from Rogers Corp. The total area of the filter is lower than $1\ \text{cm}^2$.

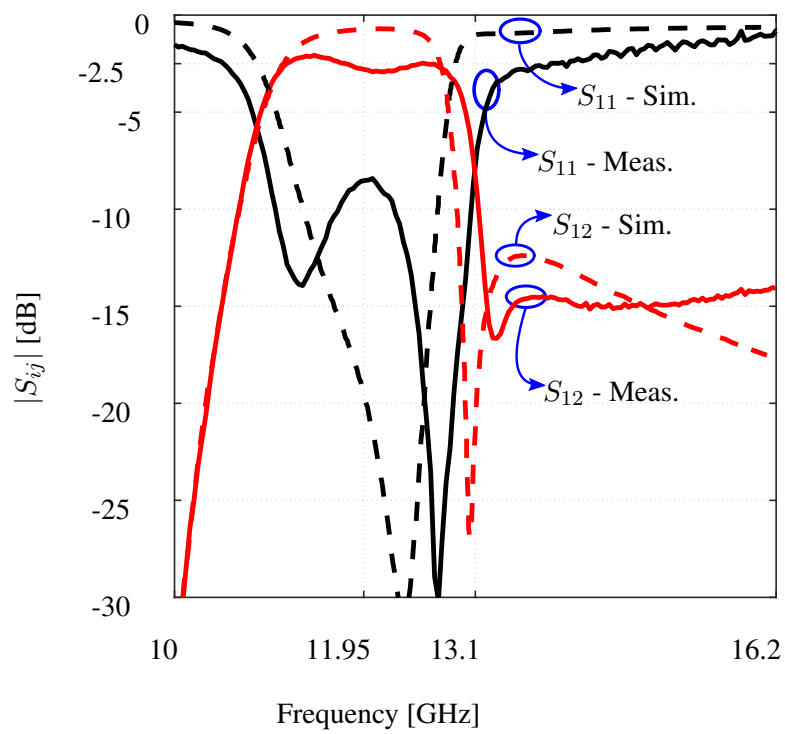
Figure 4.18: Final design of the proposed COLF BPF (a) COLR BPF design and its respective area. (b) Photograph of the manufactured COLR BPF.



Source: Reproduced from (SANTANA; BARBOSA; RONDINEAU, 2020).

Finally, Figure 4.19 shows a comparison between the results simulated in ADS and the measured COLR BPF S-parameter curves. The BPF exhibit a high-quality factor. The S_{11} of the filter is lower than $-8.7\ \text{dB}$, for all the bandwidth, in the worst case. The measured insertion loss differs from $1.5\ \text{dB}$, in the worst case.

Figure 4.19: Comparison between the simulated and measured S-parameter curves of the proposed COLR BPF.



Source: Reproduced from (SANTANA; BARBOSA; RONDINEAU, 2020).

5 IMPLEMENTATION OF HOLOGRAPHY PROCEDURE AND OPTIMIZATION ROUTINES

5.1 HOLOGRAPHY PROCEDURE VERIFICATION

To verify the holography procedure, a routine was performed in Matlab. The parameters used during the simulation are depicted in Tab. 5.1.

Table 5.1: Design Parameters.

Parameter	Value
Number of elements per row	18
Number of elements per column	18
Frequency	12 GHz
ε_r	4.5
d_x	$\lambda_g/2$
d_y	$\lambda_g/2$

Source: Own authorship.

The first field that must be defined is the reference wave. In this simulation, the excitation is considered to be a cylindrical transverse magnetic mode in the normal direction to the antenna array. For practical implementations, the magnetic field of this excitation can be modeled as the Hankel function of zeroth order and first kind (YURDUSEVEN et al., 2017), as presented below

$$H_x(\rho, \varphi) = H_0^1(k_g \rho) \cos(\phi), \quad (5.1)$$

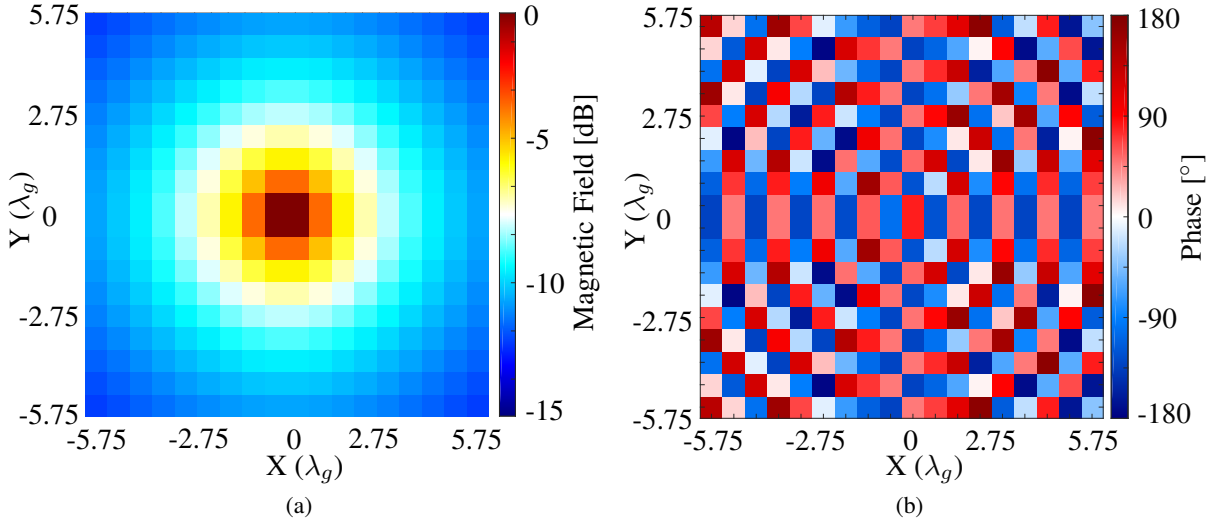
$$H_y(\rho, \phi) = H_0^1(k_g \rho) \sin(\phi). \quad (5.2)$$

In Eq. 5.1-5.2, ρ is the radial distance from the center of the array, ϕ is the polar angle, and k_g is guided wavenumber.

The magnitude and phase of this Hankel function are depicted in Fig. 5.1. Each tile, that will be called pixel henceforth, in the figures are antenna elements over the aperture. The axis is measured by guided wavelengths.

The next step is to define the object wave. This work explores two approaches. The first one is based on the work of YURDUSEVEN et al. (2017). In this approach, a point source is positioned in the far-field, in the desired direction and the field of this source is propagated in the aperture direction. This is written as

Figure 5.1: Hankel function of zeroth order and first kind (a) Magnitude (b) Phase.



Source: Own authorship.

$$O(\vec{\rho}_{mn}) = \frac{e^{-jk(|\vec{\rho}_{mn} - r'|)}}{|\vec{\rho}_{mn} - r'|}, \quad (5.3)$$

r' is the position in the far-field where the point source is placed and can be calculated by Eq. (5.4), where l is the maximum dimension of the antenna.

$$r' \geq \frac{2l^2}{\lambda_0}. \quad (5.4)$$

The projection of the far-field source over the antenna array is shown in Fig. 5.2. Once the phase contains much of the information about the shape of the beam, hereinafter the phase pattern information will be used. This projection is for a point in the lower limit of the far-field condition, pointing to 20 degrees in elevation and 60 degrees in azimuth.

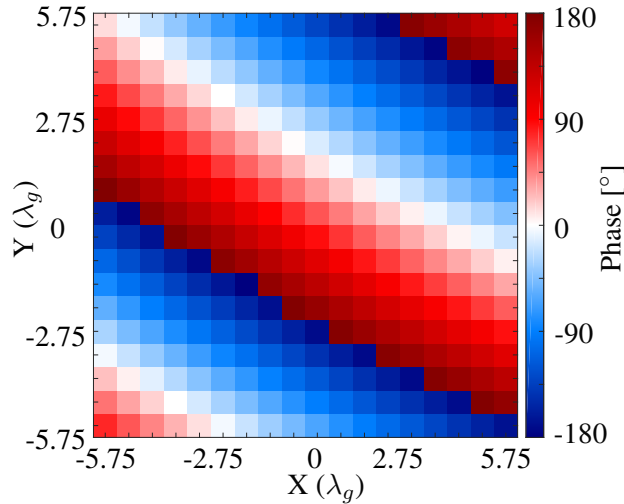
The second approach can be lead by using the phase of the complex exponential in the array factor equation (Eq. 3.16), for each element. This phase pattern is in Fig. 5.3.

Now that the reference and object waves are defined, the interference between them can be calculated. Once the phase of these waves has been used, a simple way to calculate this interference is by subtracting them, as did in Yurduseven e Smith (2017), and depicted below

$$\underline{I} = \underline{O} - \underline{H}. \quad (5.5)$$

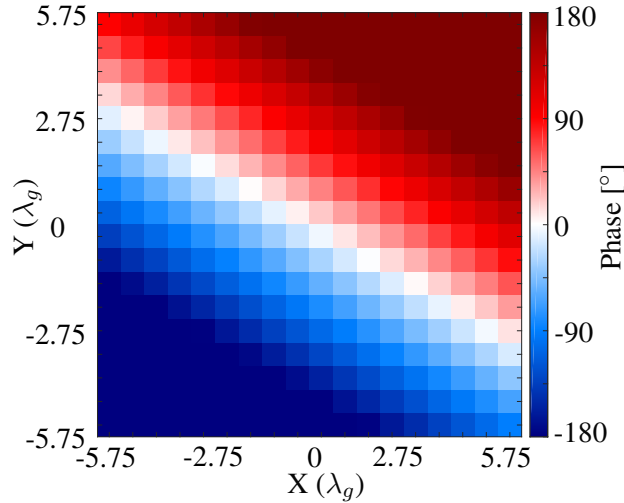
Equation (5.5) is related to the phase of the last term of Eq. (3.33). The array \underline{I} now has the information about the interference between the object and reference wave. One way to interpret this array is that it measures the difference of the available to the desired phase pattern. Thus,

Figure 5.2: Phase of the far-field source projection over the aperture - $(\theta, \varphi) = (20^\circ, 60^\circ)$.



Source: Own autorship.

Figure 5.3: Phase of each element in the aperture using the array factor equation - $(\theta, \varphi) = (20^\circ, 60^\circ)$.



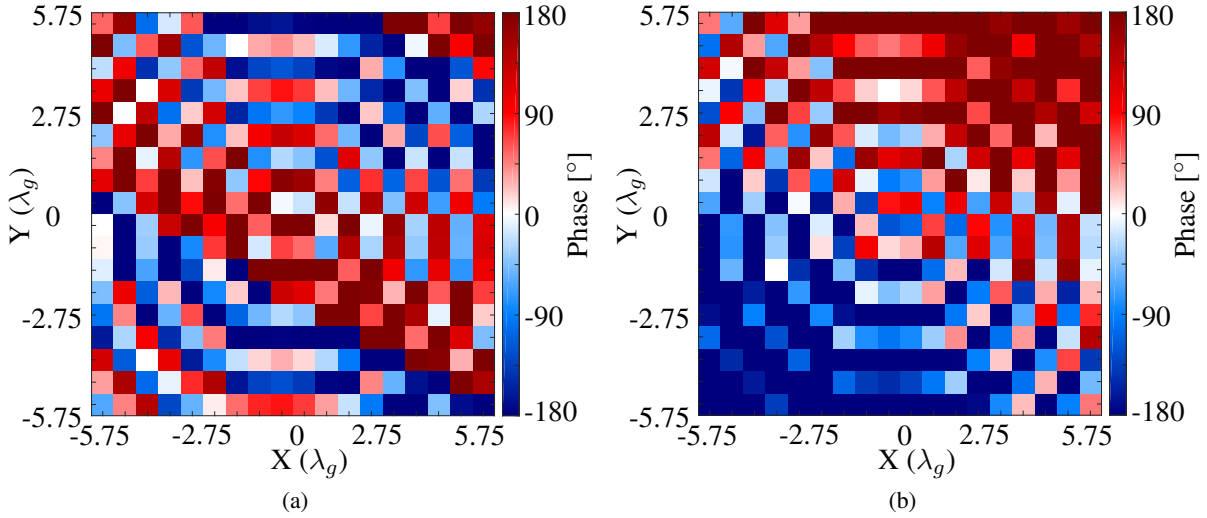
Source: Own autorship.

if an element in \underline{I} has a great value, the available phase in the reference wave for this element diverges a lot from that needed to create the desired radiation pattern. On the other side, if this value is small, the phase in this pixel is near to the desired phase. For this reason, a threshold (ξ) must be used to define when the difference is acceptable and when not. Following this argument, when the phase value is greater than the threshold, the antenna element in this place possesses a phase that does not contribute to the desired radiation pattern, and must not radiate in the free space. However, if lower, the phase of this antenna contributes to the construction of the desired radiation pattern. So, this antenna must radiate.

The phase interference pattern for the approach 1 and 2 are depicted in Fig. 5.4.

Over these interference patterns, the phase threshold must be applied. Figures 5.5-5.6 displays

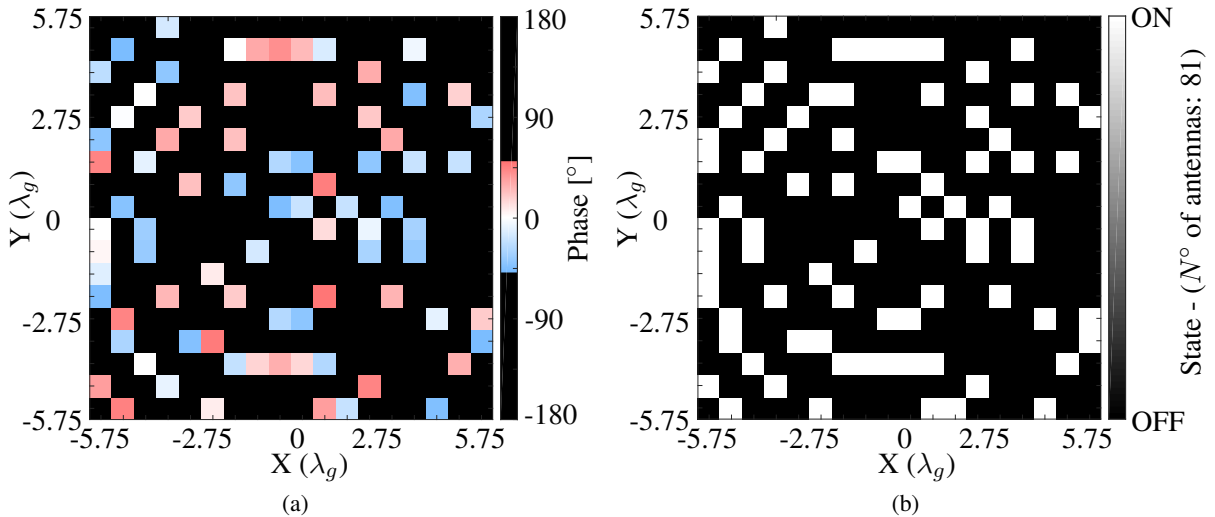
Figure 5.4: The phase interference pattern (a) Approach 1 (b) Approach 2 - $(\theta, \varphi, \xi) = (20^\circ, 60^\circ, 50^\circ)$.



Source: Own authorship.

these procedure. In Figures 5.5a-5.6a a phase threshold mask is applied over the phase interference pattern. In this case, a phase threshold $\xi = 50^\circ$ is used. The mask turns all the pixels with phases greater than ξ in black color. The pixels that remain colored agree with the phase threshold, and are allowed to radiate in the free space. Figures 5.5b-5.6b depicts the final hologram generated.

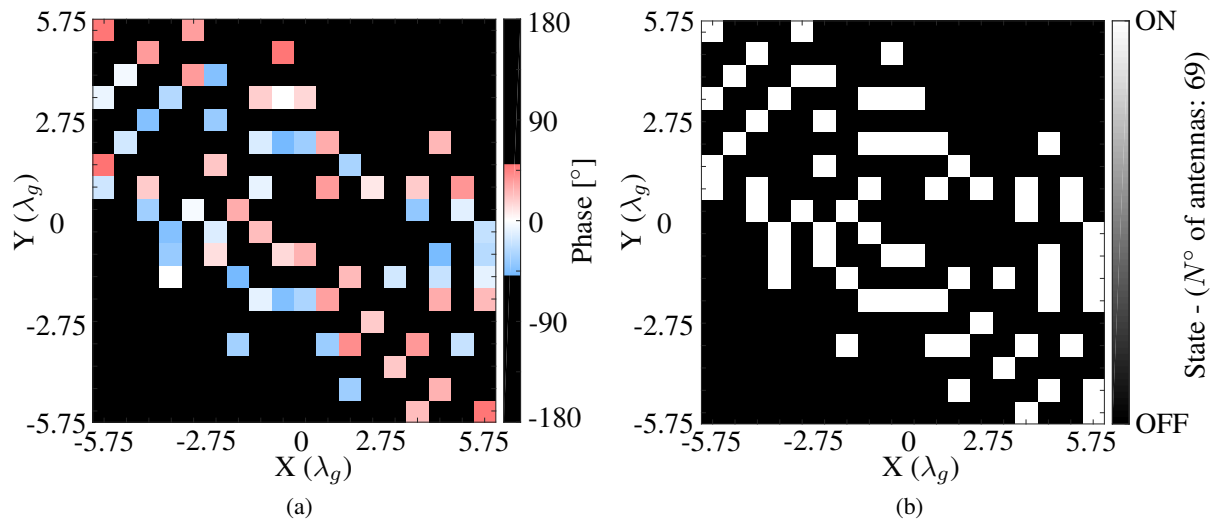
Figure 5.5: (a) Phase threshold mask applied over the phase interference pattern created by the 1st approach. The pixels in black color are the positions where the phase interference is greater that the phase threshold. (b) Hologram - $(\theta, \varphi, \xi) = (20^\circ, 60^\circ, 50^\circ)$.



Source: Own authorship.

Figure 5.7 depicts the ideal radiation pattern, with a beam focusing in $(\theta, \varphi) = (20^\circ, 60^\circ)$. On the other hand, Fig. 5.8 shows the reconstructed array factors using the holographic procedure

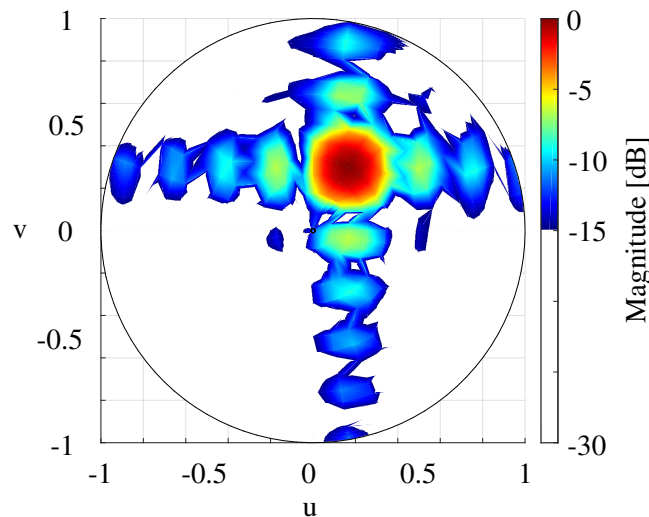
Figure 5.6: (a) Phase threshold mask applied over the phase interference pattern created by the 2nd approach. The pixels in black color are the positions where the phase interference is greater that the phase threshold. (b) Hologram - $(\theta, \varphi, \xi) = (20^\circ, 60^\circ, 50^\circ)$.



Source: Own authorship.

for the first and second approaches. These figures displays the radiation patterns in sine-space ([BROWN, 2012b](#)).

Figure 5.7: Array factor in sine space - $(\theta, \varphi, \xi) = (20^\circ, 60^\circ, 50^\circ)$.

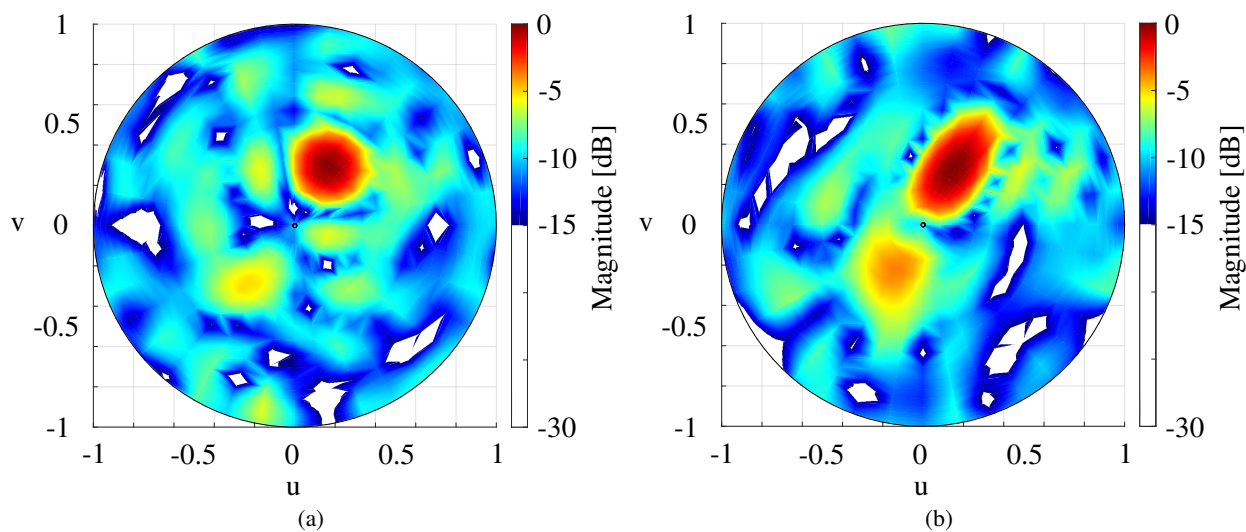


Source: Own authorship.

These same data can be displayed in the cartesian coordinates, which is also called radar coordinates, and is plotted in Fig. 5.9-5.10 ([BROWN, 2012b](#)). In both spaces, the array factors are normalized. The color gradient of the magnitude cut all levels lowest than -15 dB in white color, to emphasize the side lobes.

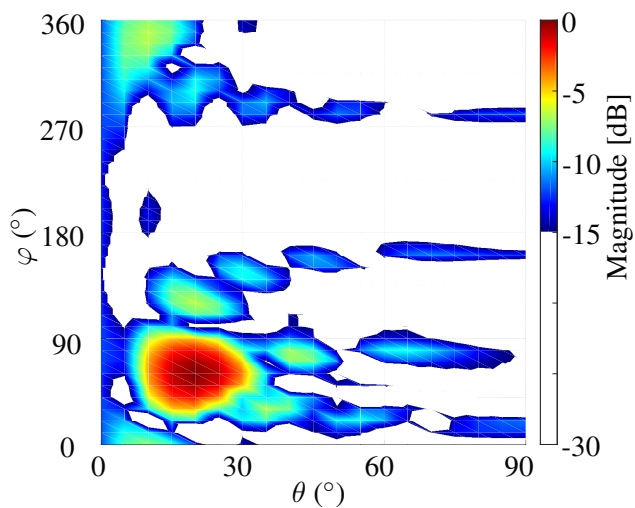
One can notice that the second approach exhibits a large beamwidth in the θ direction. Addi-

Figure 5.8: Array factor created by the holograms of the 1st and 2nd approaches in sine space - $(\theta, \varphi, \xi) = (20^\circ, 60^\circ, 50^\circ)$.



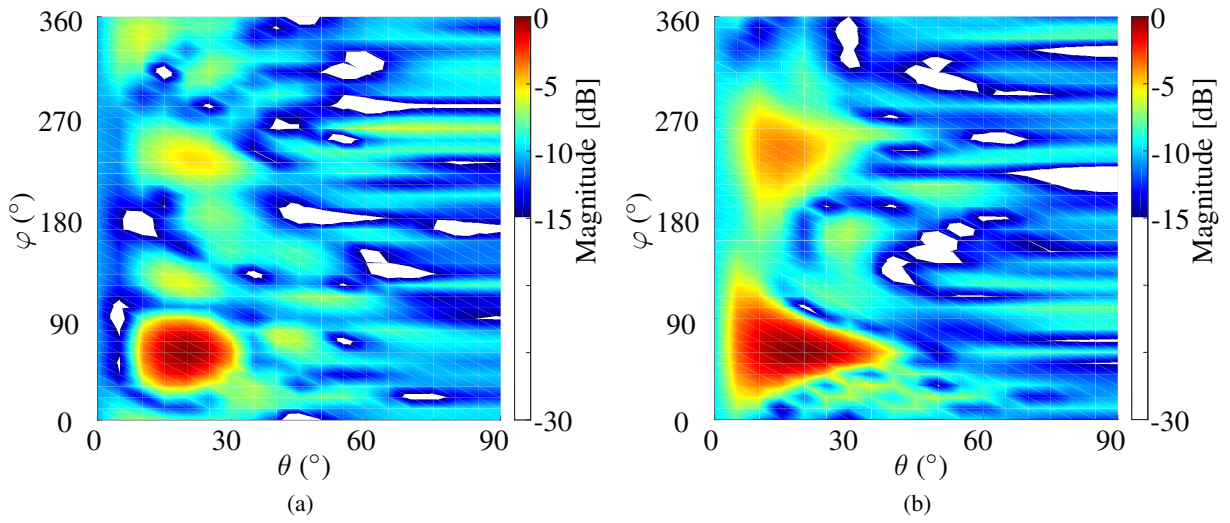
Source: Own authorship.

Figure 5.9: Array factor - $(\theta, \varphi, \xi) = (20^\circ, 60^\circ, 50^\circ)$.



Source: Own autorship.

Figure 5.10: Array factor created by the holograms of the 1st and 2nd approaches - $(\theta, \varphi, \xi) = (20^\circ, 60^\circ, 50^\circ)$



Source: Own authorship.

tionally, this approach displays a greater side lobe in the direction 180° opposite to θ . Contrary to the ideal radiation pattern, the reconstructions present side lobe levels between -5 and -15 dB, in all space.

The phase threshold controls the number of antennas that contribute to the radiation pattern. Figures 5.11-5.12 shows the holograms and its respective radiation patterns for the first and second approach, to a phase threshold of 10° , 90° and 180° .

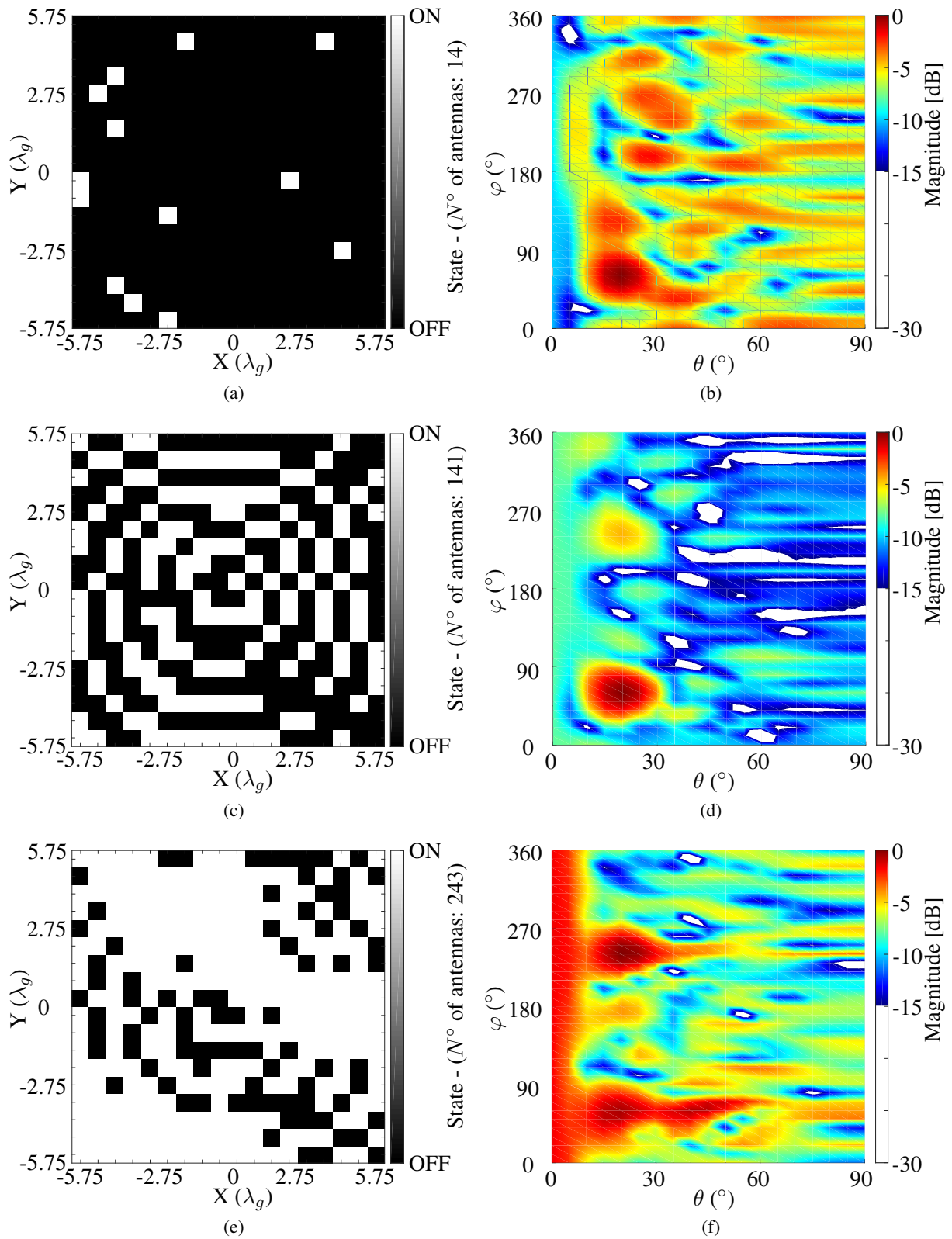
As the phase threshold increases the number of antennas radiating increases. This fact can be observed in Figs. 5.11-5.12, where the white pixel density increases as the phase threshold increases. This relation is depicted in Fig. 5.13. The gain of the array factor is another parameter that variates with the phase threshold and is depicted in Fig. 5.14.

Analyzing the results exhibited in 5.11-5.12, one can notice that the error between the desired and achieved array factor, presented in Fig. 5.9, starts high, decreases around 90° and returns to increase one more time. Finally, the error between the achieved and the desired array factor is shown in Fig. 5.15. The error was calculated using

$$\text{Error} = \frac{\|AF(\theta, \varphi) - D_f(\theta, \varphi)\|_2}{\|AF(\theta, \varphi)\|_2}. \quad (5.6)$$

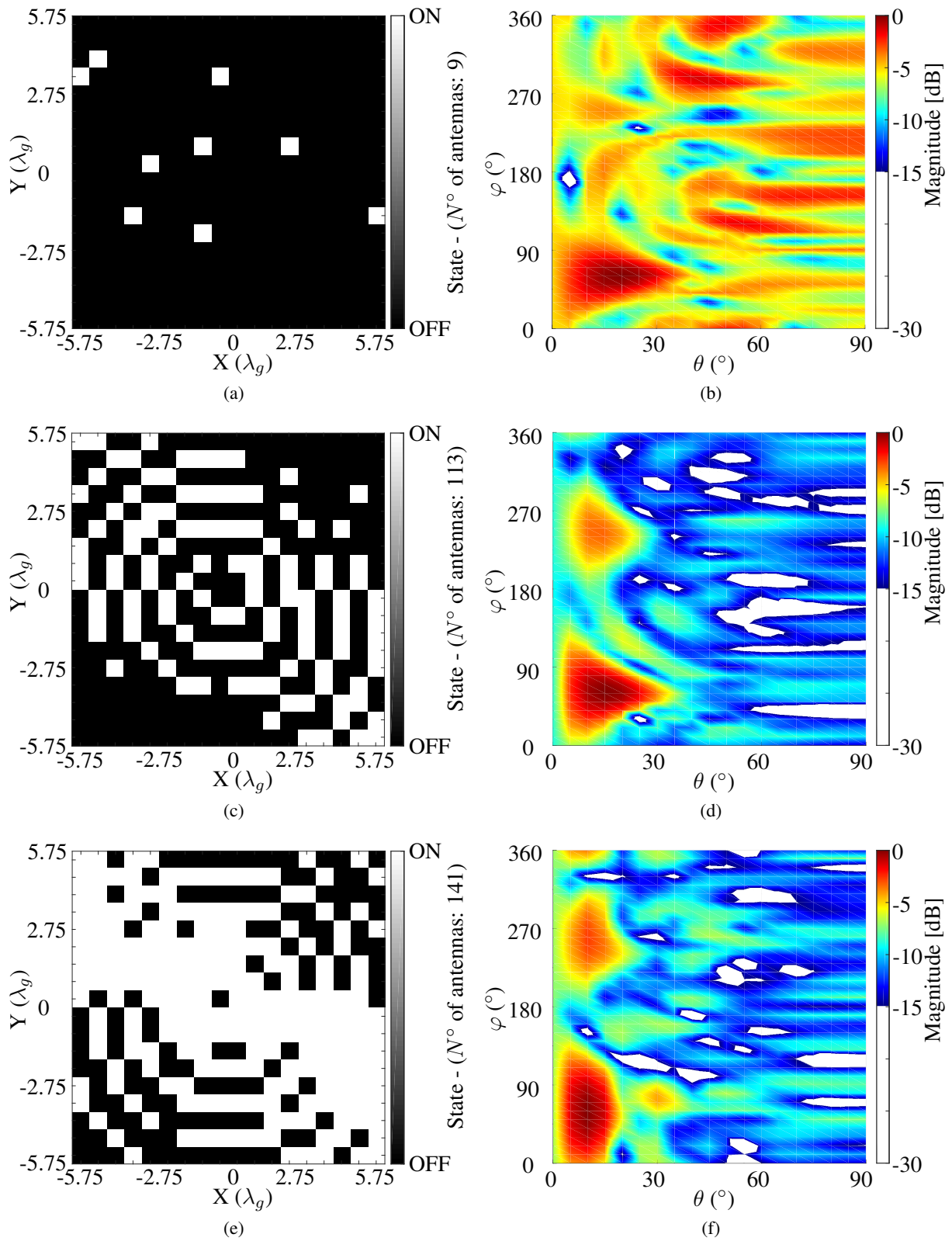
These results show that a phase threshold ξ equals 90° reaches the highest gain with the lowest error.

Figure 5.11: Phase threshold variation for the first approach: (a) Hologram - $(\theta, \varphi, \xi) = (20^\circ, 60^\circ, 10^\circ)$. (b) Array factor - $(\theta, \varphi, \xi) = (20^\circ, 60^\circ, 10^\circ)$. (c) Hologram - $(\theta, \varphi, \xi) = (20^\circ, 60^\circ, 90^\circ)$. (d) Array factor - $(\theta, \varphi, \xi) = (20^\circ, 60^\circ, 90^\circ)$. (e) Hologram - $(\theta, \varphi, \xi) = (20^\circ, 60^\circ, 180^\circ)$. (f) Array factor - $(\theta, \varphi, \xi) = (20^\circ, 60^\circ, 180^\circ)$.



Source: Own authorship.

Figure 5.12: Phase threshold variation for the first approach: (a) Hologram - $(\theta, \varphi, \xi) = (20^\circ, 60^\circ, 10^\circ)$. (b) $(\theta, \varphi, \xi) = (20^\circ, 60^\circ, 10^\circ)$. (c) Hologram - $(\theta, \varphi, \xi) = (20^\circ, 60^\circ, 90^\circ)$. (d) Radiation pattern - $(\theta, \varphi, \xi) = (20^\circ, 60^\circ, 90^\circ)$. (e) Hologram - $(\theta, \varphi, \xi) = (20^\circ, 60^\circ, 180^\circ)$. (f) Radiation pattern - $(\theta, \varphi, \xi) = (20^\circ, 60^\circ, 180^\circ)$.



Source: Own authorship.

Figure 5.13: Number of antennas tuned to ON state for different values of phase threshold for both 1st and 2nd approaches.

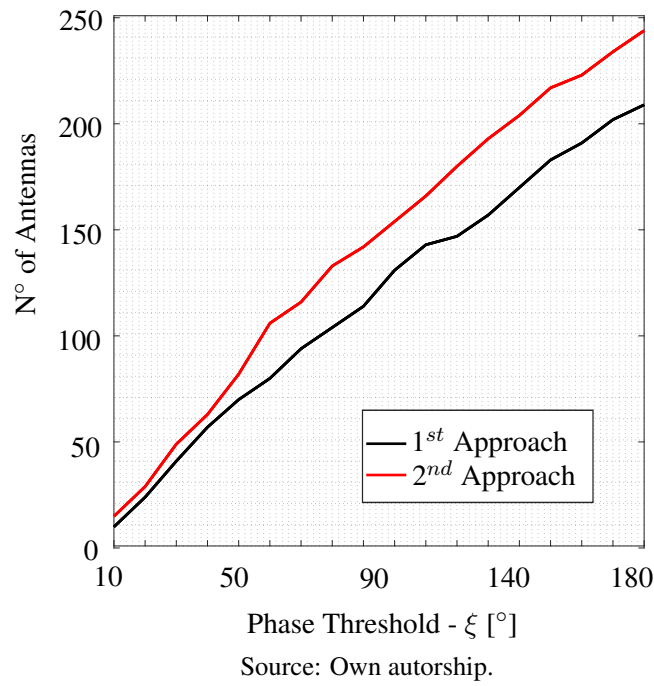


Figure 5.14: Array factor gain for different values of phase threshold for both 1st and 2nd approaches.

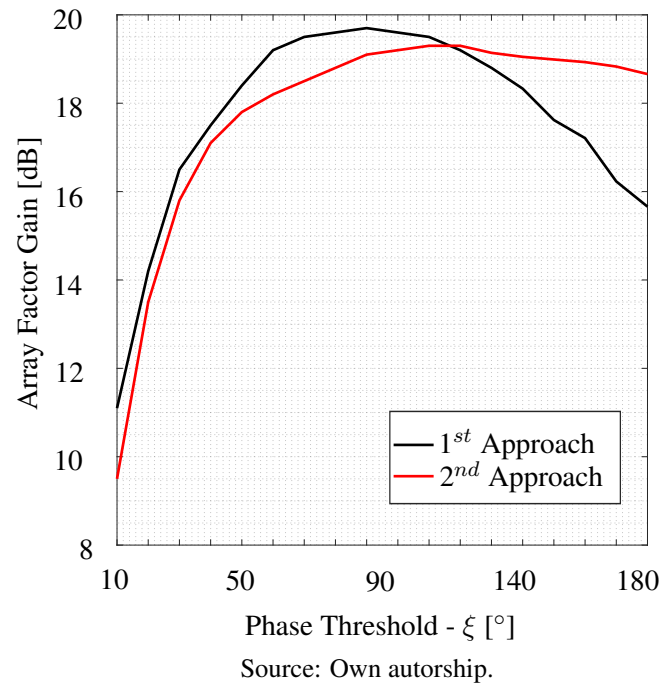
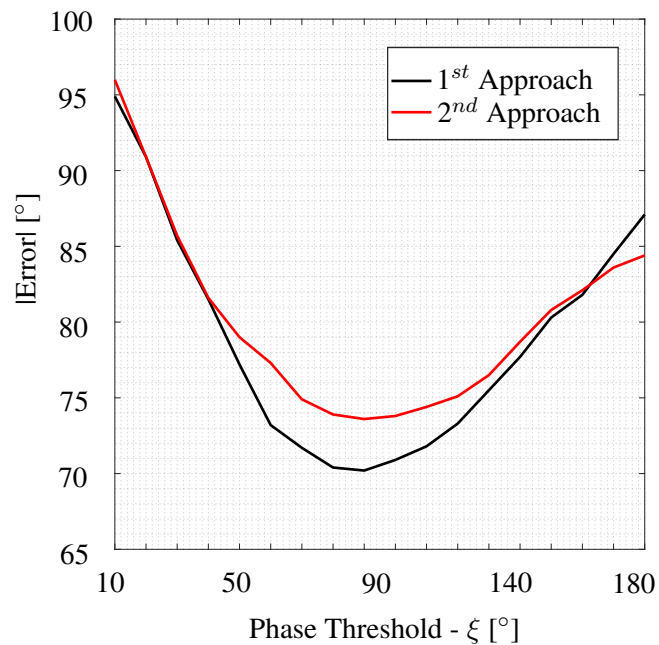


Figure 5.15: Error between the achieved and desired array factor for different values of phase threshold for both 1st and 2nd approaches.



Source: Own autorship.

5.1.1 Multi-beam Capability

Creating a multi-beam radiation pattern is a simple and natural extension of the radiation pattern synthesis, using the holographic procedure. To create a multi-beam radiation pattern is necessary to calculate one hologram for each beam, and then sum all the holograms.

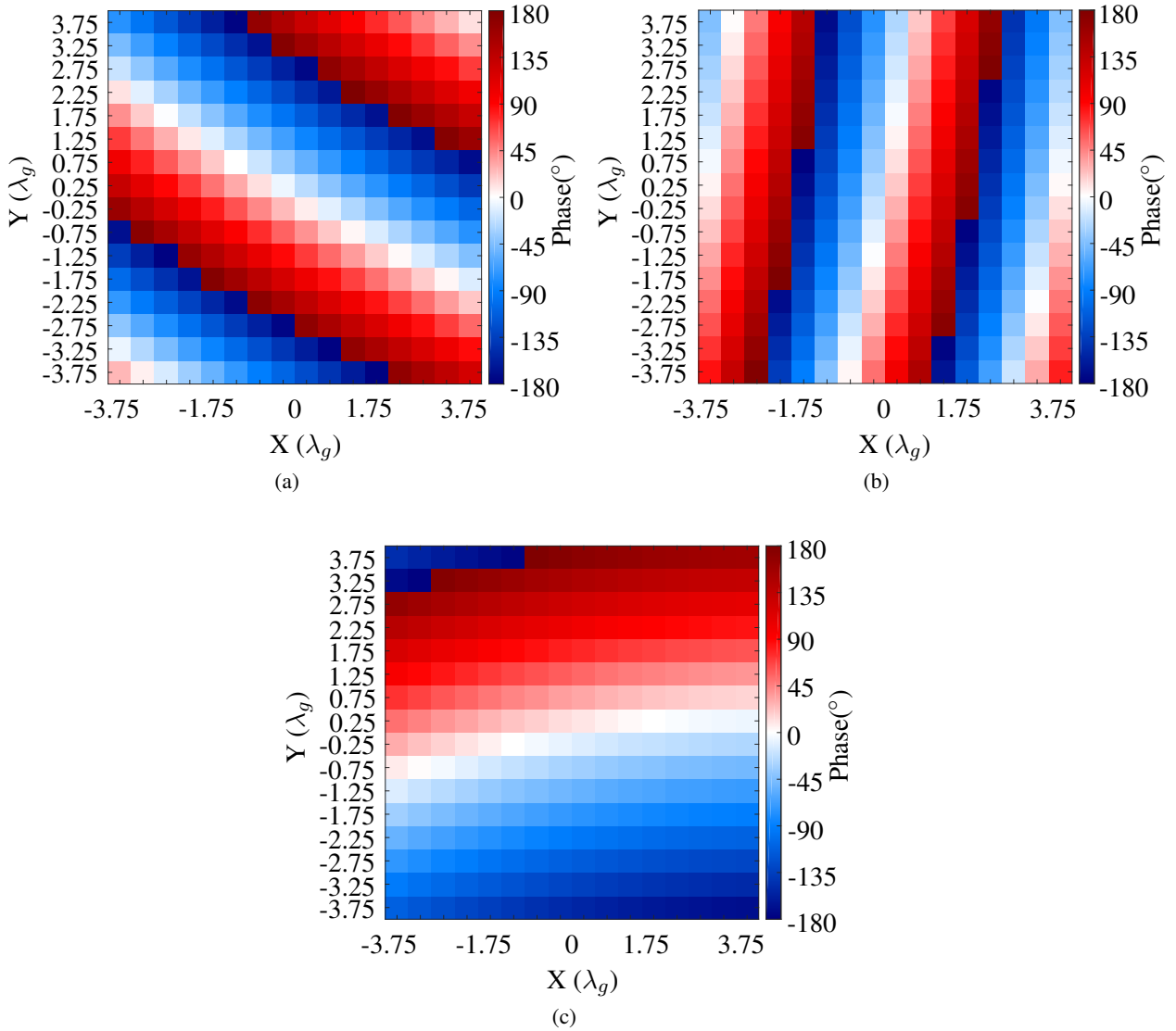
Indeed, each hologram is related to one specific radiation pattern, and sum all of them will cause interference and radiation spur in a non-desirable region. However, the premise used here is that hologram focuses the main part of the energy in a specific beam direction, radiating low sidelobes in the other directions. Thus, the interference can't interfere with the main beam of the other hologram.

As the number of pixels are finite, a common consequence is that different holograms will share the same pixel for different radiation patterns. Another relevant detail is that the phase threshold must be diminished. If a great value was assigned to the phase threshold, the sum of all holograms will create a hologram crowded of pixels in ON state, a fact that will degrade, and in the worst-case vanish, the identity of each hologram.

Consequently, a phase threshold lower than the optimum value observed in Figs. 5.13-5.15 must be selected. In the following example, a phase threshold of 50° was chosen. For this example, three holograms are summed to create a three-beam radiation pattern. The phase distribution used to create the three holograms are depicted in Fig. 5.16, and the respective holograms are in Fig. 5.17. The aperture has 16×16 pixels. Each hologram has an average of 64 pixels in the ON

state, the final hologram assigned 150 pixels in the ON state. In this case, more than 100 pixels remaining in the OFF state, permitting the array to radiate properly in the desired regions.

Figure 5.16: Phase distribution in the aperture used to create the multi-beam radiation pattern (a) $(\theta, \varphi) = (25^\circ, 60^\circ)$. (b) $(\theta, \varphi) = (35^\circ, 170^\circ)$. (c) $(\theta, \varphi) = (15^\circ, 280^\circ)$.



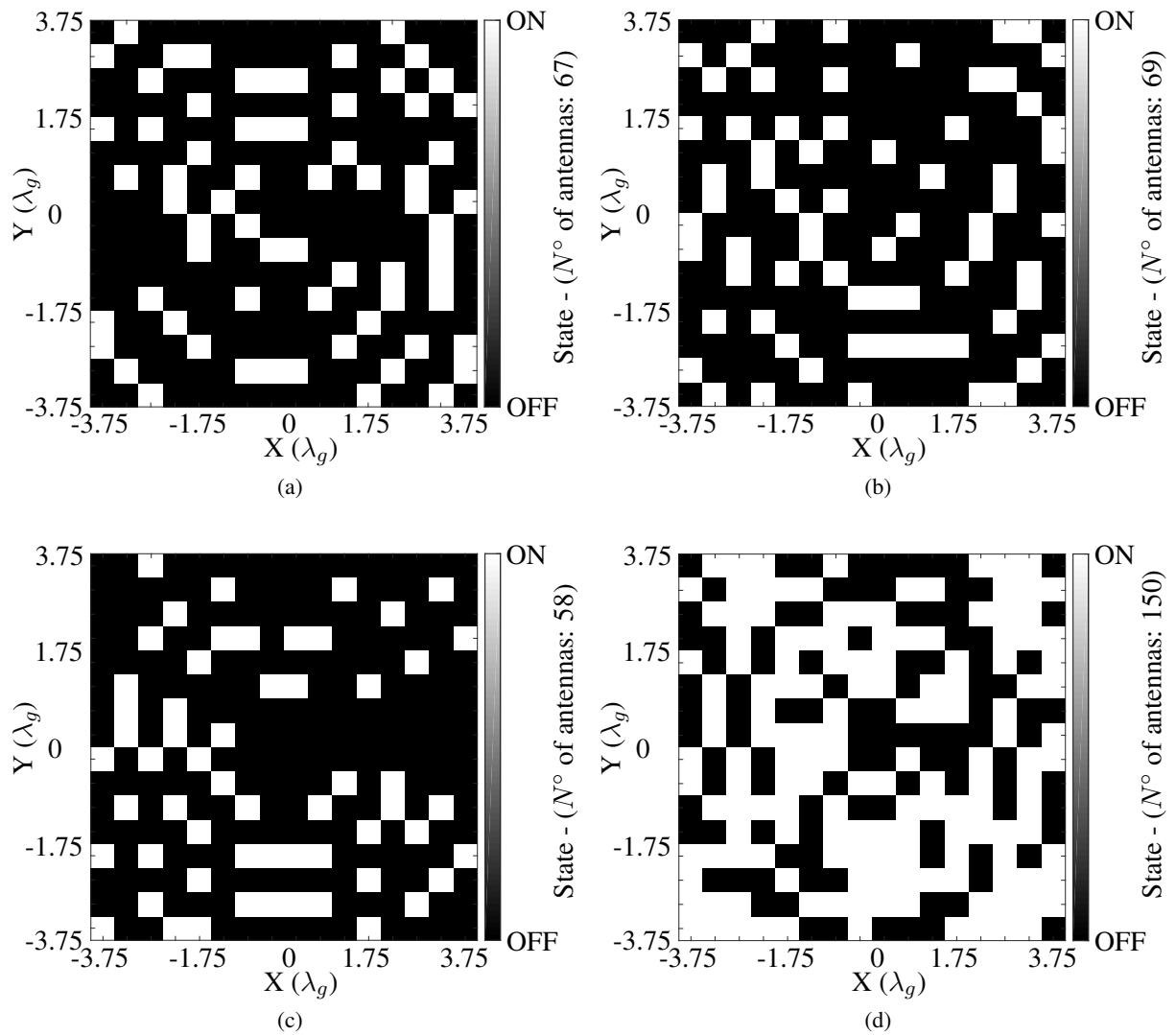
Source: Own authorship.

A comparison between the ideal and real radiation pattern is shown in Figs. 5.18-5.19. In these patterns is possible to notice that the pointing direction is obeyed and the sidelobe level is increased, as observed in the mono-beam case.

5.2 OPTIMIZATION VERIFICATION

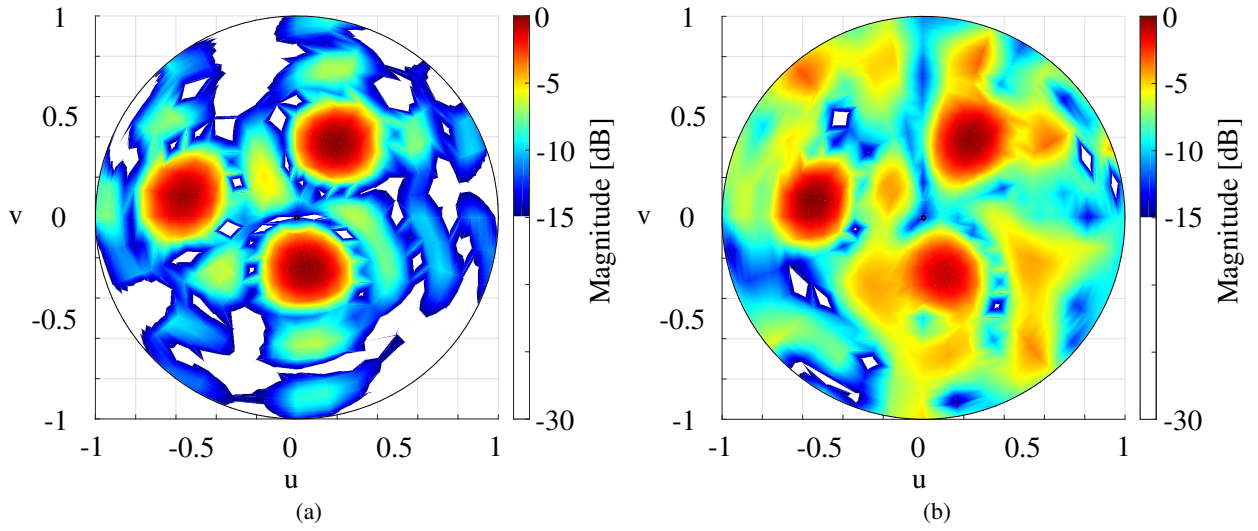
To verify the optimization procedure a routine is implemented in MATLAB, using CVX package (GRANT; BOYD, 2014). This routine implements the Eq. 3.56. The use of the auxiliary

Figure 5.17: Holograms used to create the multi-beam radiation pattern (a) $(\theta, \varphi) = (25^\circ, 60^\circ)$. (b) $(\theta, \varphi) = (35^\circ, 170^\circ)$. (c) $(\theta, \varphi) = (15^\circ, 280^\circ)$. (d) Summation of all holograms.



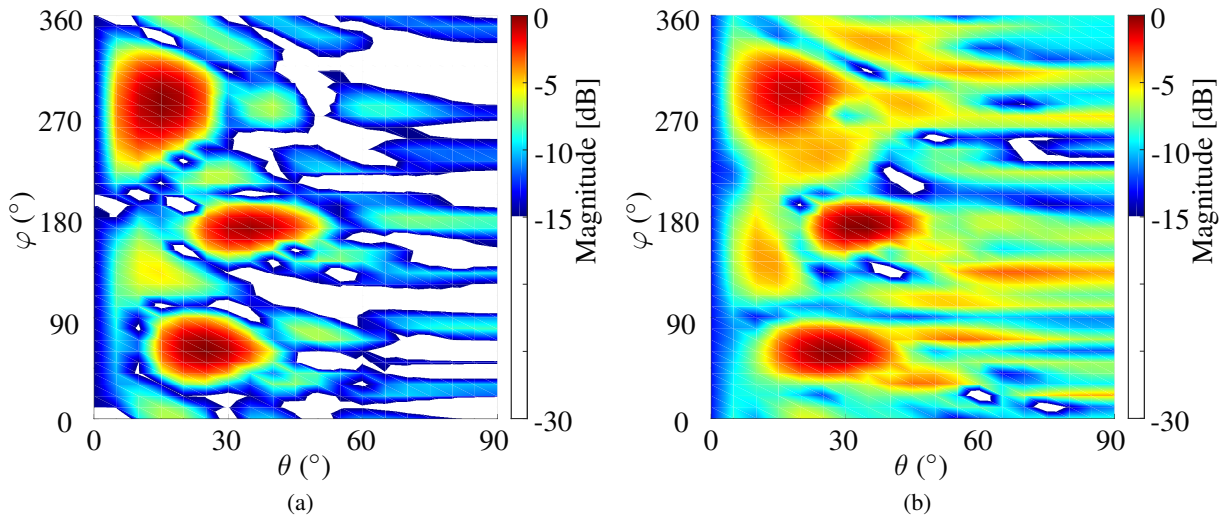
Source: Own authorship.

Figure 5.18: Array factor of the multi-beam hologram in sine space (a) Ideal array factor. (b) Real array factor.



Source: Own authorship.

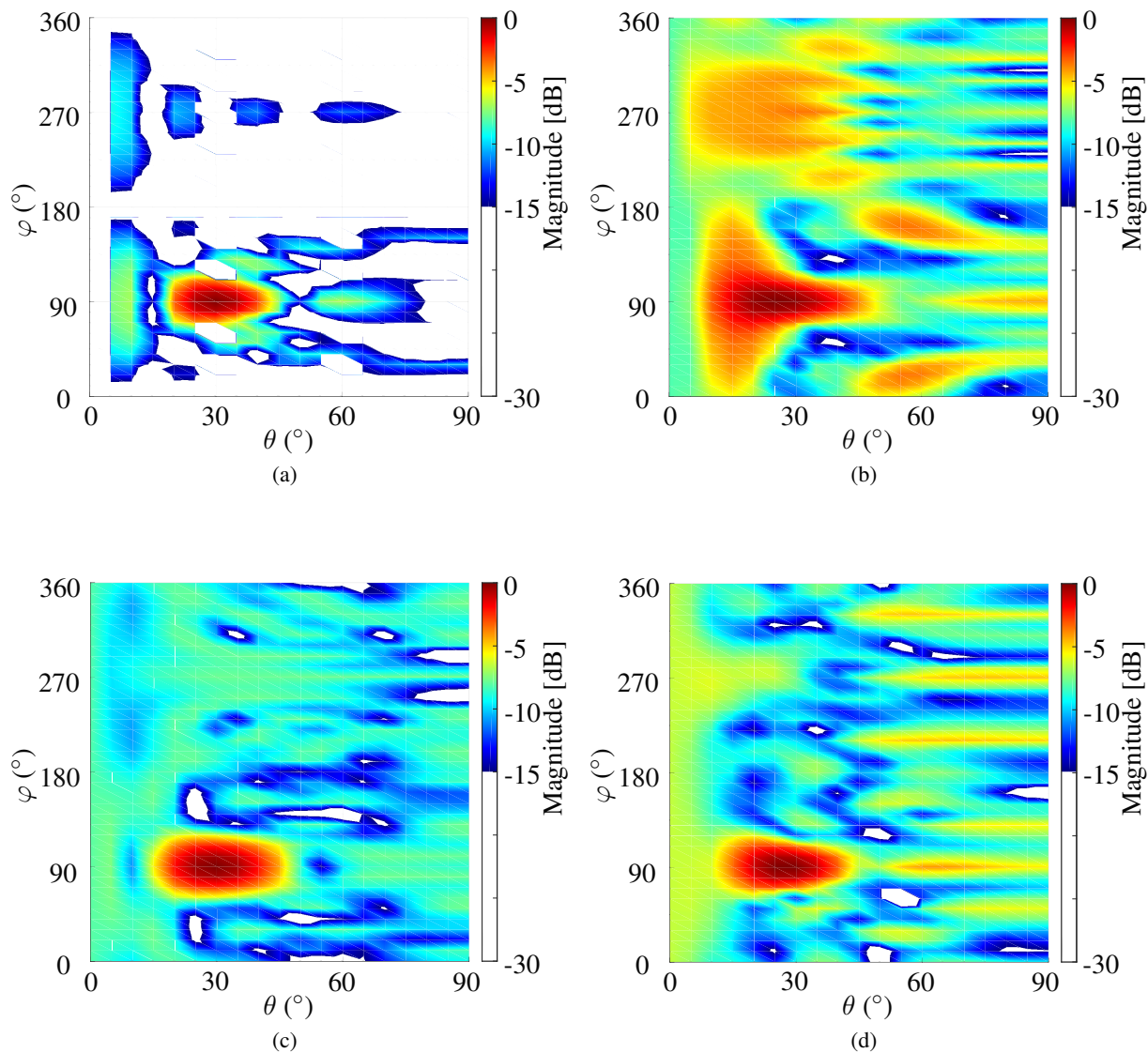
Figure 5.19: Array factor of the multi-beam hologram (a) Ideal array factor. (b) Real array factor.



Source: Own authorship.

variable creates some values greater than one, during the optimization procedure. These values must then be corrected to one again, to accord with the antenna model. These results are exhibited in Fig. 5.20-5.21, for a pointing direction of $(\theta, \varphi) = (30^\circ, 90^\circ)$.

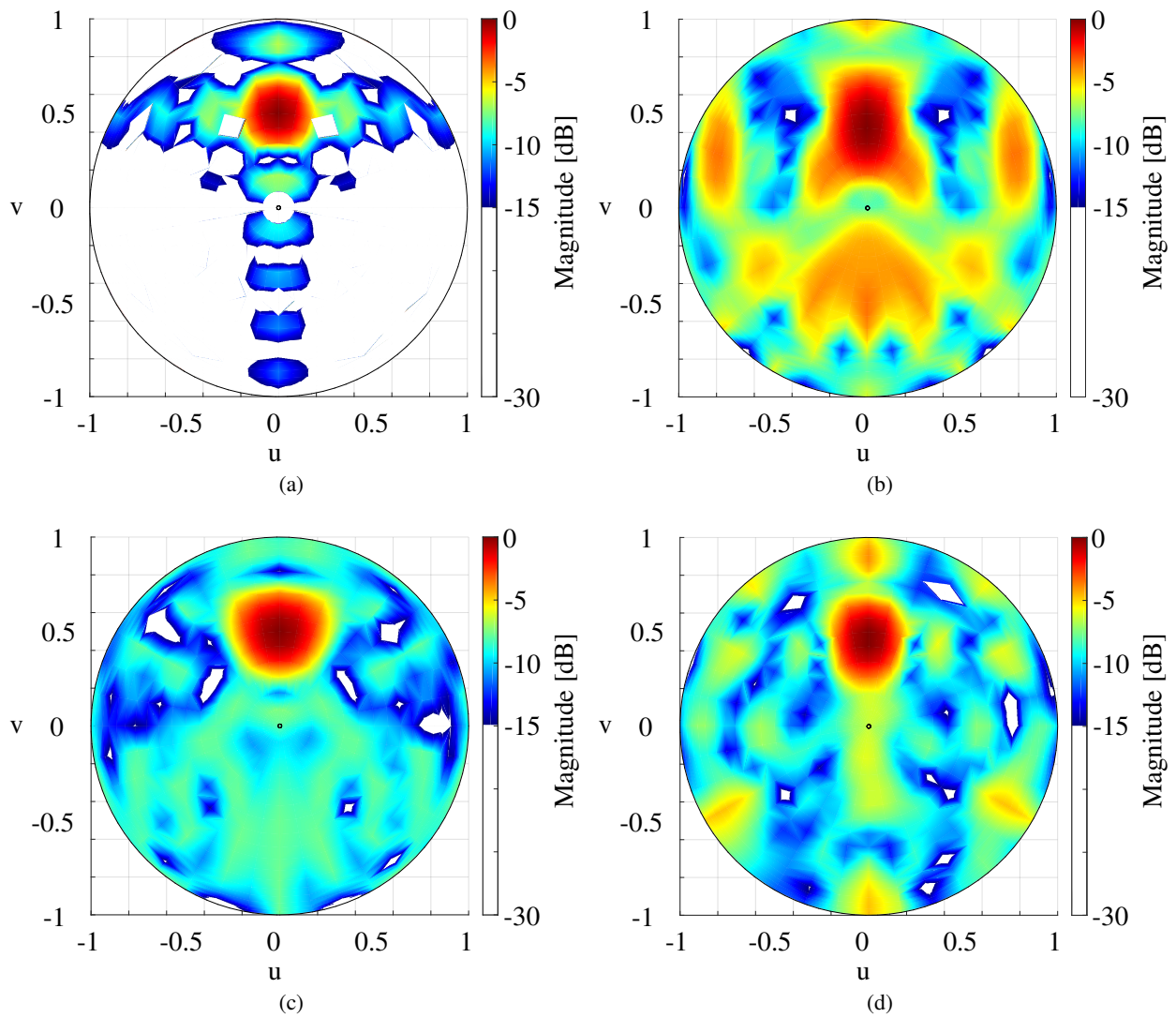
Figure 5.20: Array factor after the convex optimization process of a beam in $(\theta, \varphi) = (30^\circ, 90^\circ)$ (a) Ideal array factor. (b) Array factor from the holographic procedure. (c) Array factor from the optimization process. (d) Array factor after rounding the optimization mask.



Source: Own authorship.

Observing the results presented in Figs. 5.20-5.21, it is possible to see a reduction at the sidelobe level, increased the fir with the desired radiation field.

Figure 5.21: Array factor after the convex optimization process of a beam in $(\theta, \varphi) = (30^\circ, 90^\circ)$ in sine space (a) Ideal array factor. (b) Array factor from the holographic procedure. (c) Array factor from the optimization process. (d) Array factor after rounding the optimization mask.



Source: Own authorship.

6 CONCLUSIONS AND FUTURE WORK

The use of the holography technique in beamforming opens a new set of tools to be exploited in the spatial multiple division market. This technique employs simple procedures from optical holography, such as record and reconstructs the information of the desired radiation pattern in holograms. The object wave using beam projection over the aperture creates the holograms that are nearer to the desired radiation pattern. Additionally, while performing a parametric sweep over the phase threshold, the value of 90° also brings the higher gain.

The metasurface antenna technology is an important apparatus to implement this technique, once it permits to perform the control of the surface antenna resonance in a simple manner. The surface wave created by the coaxial monopole can also be created by an end-launched connector, but the symmetry of the problem is lost in this scenery.

The reconfigurable capability enhances the set of possible applications of this proposal, once it can act as a software-defined antenna. The PIN diode makes this process simple, since it is enough just changing the bias at its terminals. However, the bias network adds some complexity to the metasurface antenna and can be a problem when the structure is scaled for large antenna arrays.

The results achieved show a good fit between the desired array factors and the array factor from the holographic procedure. Nonetheless, the results present a noteworthy sidelobe level in comparison to the desired array factor.

The convex optimization procedure can handle this problem, reducing the sidelobe level. During this calculation, the minimization of the mixed ℓ_1 and ℓ_∞ norms demonstrate a good trade-off between the sparse and binary solution. However, in some cases, the minimization of the ℓ_∞ creates low sidelobes, once it does not restrict the number of pixels at ON state.

Furthermore, the proposed antenna showed that implementing multibeam array factors is a simple task, with the use of the holographic technique. However, great values of phase threshold can make the beam direction diverge from the desired radiation pattern.

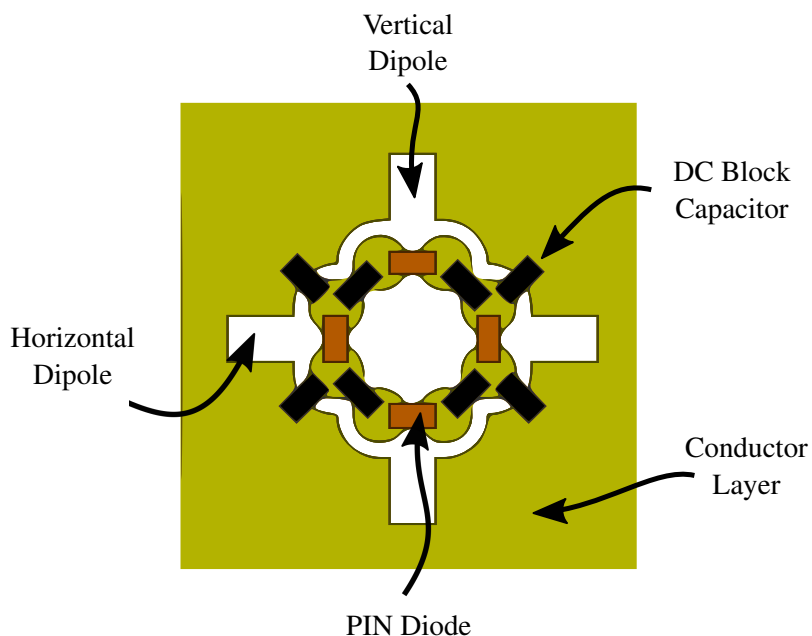
6.1 FUTURE WORK

Possible future works that can be carried out are, for example, use bowtie and hourglass slot dipole antennas, instead of simple slot dipoles. This type of antenna exhibits a broadband behavior and can be used to implement high-performance antenna array systems.

Another improvement that can be performed is to use Cross Slot Dipole Antennas (CSDA). An example of implementation of this proposal is depicted in Fig. 6.1. In this antenna, two dipoles are placed orthogonally. The operating mechanism of this antenna is the same as the simple SDA. Nevertheless, the biasing network needs to be modified to incorporate additional

PIN diodes, to permit the creation of a conductor path in both SDA. To do this, two PIN diodes are placed in each SDA. Two via pads and through-hole vias must be added to allow bias each PIN diode individually. As in the SDA, capacitors must be added to create a path for the surface current.

Figure 6.1: Top view of the active cross-slot dipole antenna cell. The PIN diode works like a ON-OFF switch, changing the effective length of the slot. The capacitor acts like DC blocks to isolate the bias signal in the pads.

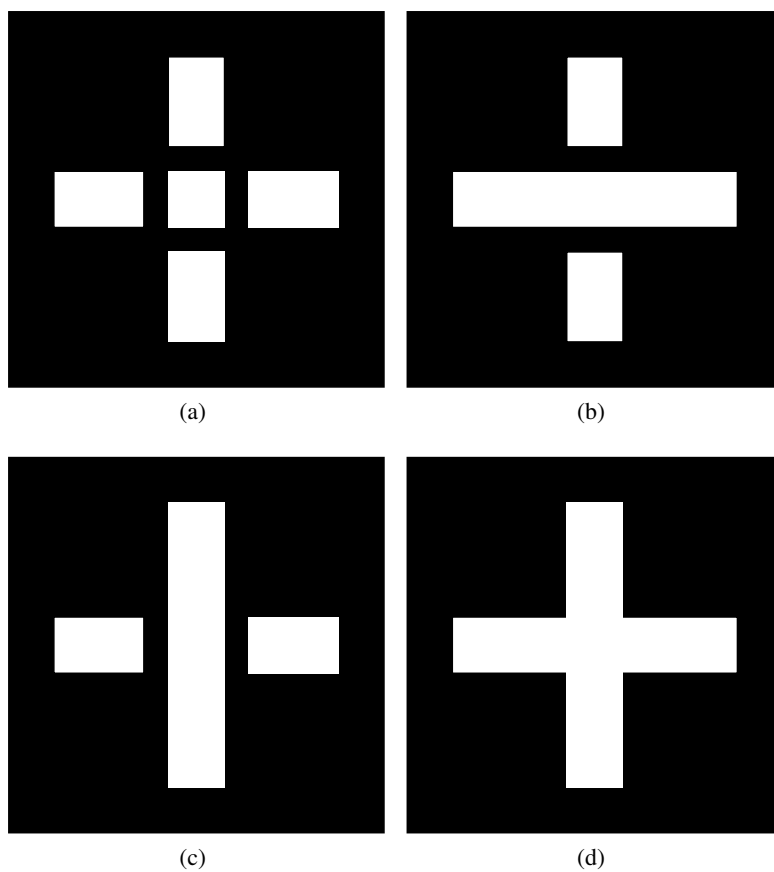


Source: Own autorship.

The CSDA can assume four different states, and they are shown in Fig. 6.2. The CSDA can exhibit one OFF state, and three ON states. The three irradiating states differ in the polarization of the propagating wave. This state can propagate linear vertical, linear horizontal, and circular polarization.

Another approach that can be carried out is to use machine learning techniques to calculate the hologram of the shape of the radiation pattern.

Figure 6.2: Representation of electric path of the four states of the cross slot dipole antenna (a) Off state. (b) Vertical polarization. (c) Horizontal polarization. (d) Circular polarization.



Source: Own authorship.

BIBLIOGRAPHY

- ACKERMANN, G. K.; EICHLER, J. *Holography - A Practical Approach*. GE, Weinheim: Wiley-VCH, 2007.
- BAHL, I. J. *Lumped Elements for RF and Microwave Circuits*. first. Norwood, MA: Artech House, 2003.
- BALANIS, C. A. *Antenna Theory - Analysis and Design*. NJ, Hoboken: John Wiley and Sons, 2005.
- BALANIS, C. A. *Advanced Engineering Electromagnetics*. second. Hoboken, NJ: John Wiley and Sons, 2012.
- BHATTACHARYYA, A. K. *Phased Array Antennas Floquet Analysis, Synthesis, BFNs, and Active Array Systems*. Hoboken, NJ: John Wiley and Sons, Inc., 2006.
- BILY, A.; DALLAS, J.; HANNIGAN, R. J.; KUNDTZ, N.; NASH, D. R.; STEVENSON, R. A. *SURFACE SCATTERING ANTENNA IMPROVEMENTS*. 2014.
- BLACK, E. J. *Holographic Beam Forming and MIMO Holographic Beam Forming and MIMO*. [S.l.], 2017.
- BLASS, J. Multi-directional antenna - a new approach to stacked beams. *IRE Nat. Conv. Record.*, p. 48–50, 1960.
- BODEHOU, M.; GONZÁLEZ-OVEJERO, D.; CRAEYE, C.; HUYNEN, I. Method of moments simulation of modulated metasurface antennas with a set of orthogonal entire-domain basis functions. *IEEE Transactions on Antennas and Propagation*, v. 67, n. 2, p. 1119 – 1130, feb 2019.
- BOOKER, H. G. Slot aeriels and their relation to complementary wire aeriels (babinet's principle). *Proceedings of the IEE (London)*, v. 93, n. 4, p. 620–626, may 1946.
- BOSILJEVAC, M.; CASALETTI, M.; CAMINITA, F.; SIPUS, Z.; MACI, S. Non-uniform metasurface luneburg lens antenna design. *IEEE Transactions on Antennas and Propagation*, v. 60, n. 9, p. 4065 – 4073, jul 2012.
- BOYD, S.; VANDENBERGHE, L. *Convex Optimization*. Cambridge, United Kingdom: Cambridge University Press, 2004.
- BROWN, A. D. *Electronically Scanned Arrays - MATLAB Modeling and Simulation*. FL, Boca Raton: CRC Press, 2012.
- BROWN, A. D. *Engineering Electronically Scanned Arrays MATLAB - Modeling and Simulation*. Boca Raton, FL: CRC Press, 2012.
- BUTLER, J. L. Microwave scanning antennas,. In: _____. [S.l.]: Academic Press, 1966. III, cap. 3 - Digital, Matrix and Intermediate-Frequency Scanning.
- BUTLER, J. L.; LOWE, R. Beam forming matrix simplifies design of electronically scanned antennas. *Electronic Design*, v. 9, p. 170–173, apr 1961.
- CALOZ, C.; ITOH, T.; RENNINGS, A. Crlh metamaterial leakywave and resonant antennas. *IEEE Antennas and Propagation Magazine*, v. 50, p. 25–39, 2008.

CERVENY, M.; FORD, K. L.; TENNANT, A. Metasurface synthesis using susceptibility tensors and holographic technique. *Loughborough Antennas & Propagation Conference*, nov 2017.

CHALOUN, T.; ZIEGLER, V.; MENZEL, W. Design of a dual-polarized stacked patch antenna for wide-angle scanning reflectarrays. *IEEE TRANSACTIONS ON ANTENNAS AND PROPAGATION*, VOL. 64, NO. 8, AUGUST 2016, v. 64, n. 8, p. 3380–3390, aug 2016.

CHEN, H. T.; PADILLA, W. J.; CICH, M. J.; AZAD, A. K.; AVERITT, R. D.; TAYLOR, A. J. A metamaterial solid-state terahertz phase modulator. *Nature Photonics*, v. 3, p. 148–151, 2009.

CHENG, Y.; YANG, H.; XIAO, Z. C. B. A planar polarization-insensitive metamaterial absorber. *Photonics and Nanostructures Fundamentals and Applications*, v. 9, p. 8–14, 2011.

CHIPENGO, U.; SLIGAR, A.; CARPENTER, S. High fidelity physics simulation of 128 channel mimo sensor for 77ghz automotive radar. *IEEE Access*, v. 8, p. 160643–160652, sep 2020.

CHOU, H.-T.; CHANG, C.-Y. Application of rotman lens beamformer for relatively flexible multibeam coverage from electrically large-phased arrays of antennas. *IEEE TRANSACTIONS ON ANTENNAS AND PROPAGATION*, v. 67, n. 5, p. 3058–3066, may 2019.

DJERAFI, T.; FONSECA, N. J. G.; WU, K. Planar -band 4 4 nolen matrix in siw technolog. *IEEE TRANSACTIONS ON MICROWAVE THEORY AND TECHNIQUES*, v. 58, n. 2, p. 259–266, feb 2010.

DOHERTY, W. E.; JOOS, R. D. *The Pin Diode Circuit Designers' Handbook*. MA, Watertown: Microsemi Corp, 1998.

EBADI, S.; DRISCOLL, T.; SMITH, D. Visual illustrations of microwave holographic beamforming using a modulated surface-impedance metamaterial. *2013 IEEE Antennas and Propagation Society International Symposium*, jul 2013.

ELMANSOURI, M. A.; BOSKOVIC, L. B.; FILIPOVIC, D. S. Compact wideband dual-polarized in-band full-duplex antenna subsystem. *IEEE Transactions on Antennas and Propagation*, 2021.

EPSTEIN, A.; WONG, J. P. S.; ELEFTHERIADES, G. V. Cavity-excited huygens' metasurface antennas for near-unity aperture illumination efficiency from arbitrarily large apertures. *Nature Communications*, v. 7, n. 10360, jan 2016.

ESMAN, R.; FRANKEL, M.; PARENT, M. True time-delay fiber-optic control of a phased-array transmitter with three-octave bandwidth. *Proceedings of 1995 IEEE MTT-S International Microwave Symposium*, p. 1111–1114, 1995.

ETTORRE, M.; MANZILLO, F. F.; MEMBER, S.; CASALETTI, M.; SAULEAU, R.; COQ, L. L.; CAPET, N. Continuous transverse stub array for ka-band applications. *IEEE TRANSACTIONS ON ANTENNAS AND PROPAGATION*, VOL. 63, NO. 11, NOVEMBER 2015, v. 63, n. 11, p. 4792–4800, nov 2015.

FAENZI GABRIELE MINATTI, D. G.-O. F. C. E. M. C. D. G. M.; MACI, S. Metasurface antennas: New models, applications and realizations. *Scientific Reports*, v. 9, jul 2019.

FENN, A. J. *Adaptive Antennas and Phased Arrays for Radar and Communications*. [S.l.]: Artech House, 2008.

FERESIDIS, A. P.; GOUSSETIS, G.; WANG, S.; VARDAXOGLU, J. C. Artificial magnetic conductor surfaces and their application to lowprofile high-gain planar antennas. *IEEE Transactions Antennas and Propagation*, v. 53, p. 209–215., 2005.

FERRANDO-ROCHER, M.; HERRANZ-HERRUZO, J. I.; VALERO-NOGUEIRA, A.; RODRIGO, V. M. Circularly polarized slotted waveguide array with improved axial ratio performance. *IEEE TRANSACTIONS ON ANTENNAS AND PROPAGATION*, v. 64, n. 9, p. 4144–4148, sep 2016.

FLEURY, R.; MONTICONE, F.; ALÙ, A. Invisibility and cloaking: Origins, present, and future perspectives. *PHYSICAL REVIEW APPLIED*, v. 4, jul 2015.

FONG, B. H.; COLBURN, J. S.; OTTUSCH, J. J.; VISHER, J. L.; SIEVENPIPER, D. F. Scalar and tensor holographic artificial impedance surfaces. *IEEE Transactions on Antennas and Propagation*, v. 58, n. 10, p. 3212 – 3221, oct 2010.

FRANKEL, M. Y.; ESMAN, R. D. True time-delay fiber-optic control of an ultrawideband array transmitted receiver with multibeam capability. *IEEE TRANSACTIONS ON MICROWAVE THEORY AND TECHNIQUES*, v. 43, n. 9, p. 2357–2394, sep 1995.

FUCHS, B. Synthesis of sparse arrays with focused or shaped beampattern via sequential convex optimizations. *IEEE TRANSACTIONS ON ANTENNAS AND PROPAGATION*, v. 60, n. 7, jul 2012.

FUCHS, B.; RONDINEAU, S. Array pattern synthesis with excitation control via norm minimization. *IEEE Transactions on Antennas and Propagation*, v. 64, n. 10, 2016.

GARBOR, D. A new microscopic principle. *Nature*, v. 161, p. 777–778, may 1948.

GENT, H. The bootlace aerial. *Royal Radar Establishment Journal*, p. 47–57, oct 1957.

GNU. *GLPK (GNU Linear Programming Kit)*. 2012. Disponível em: <<https://www.gnu.org/software/glpk/#introduction>>.

GRANT, M.; BOYD, S. *CVX: Matlab Software for Disciplined Convex Programming, version 2.1*. 2014. <<http://cvxr.com/cvx>>.

GUROBI. *Mixed-Integer Programming (MIP) – A Primer on the Basics*. 2021.

HANSEN, R. C. *Phased Array Antennas*. Neew York, NY: John Wiley and Sons, Inc., 2001.

HARIHARAN, P. *Basics of Holography*. [S.l.]: Cambridge University Press, 2002.

HARIHARAN, P. *Basics of Interferometry*. [S.l.]: Academic Press, 2007.

HASHEMI, S. M.; TRETYAKOV, S. A.; SOLEIMANI, M.; SIMOVSKI, C. R. Dual polarized angularly stable high-impedance surface. *IEEE Transactions Antennas and Propagation 2013;61:4101–8.*, v. 61, p. 4101–4108., 2013.

HOLOGRAPHY. 2020. Disponível em: <<http://hyperphysics.phy-astr.gsu.edu/hbase/optmod/holog.html>>.

HONG, J. G.; LANCASTER, M. J. *Microstrip Filters for RF/Mi-crowave Applications*. first. [S.l.]: John Wiley and Sons, 2001. ., 1st ed. , 2001.

HONG, J. S. Couplings of asynchronously tuned coupled microwave resonators. *IEE Proceedings - Microwave, Antennas and Propagation*, v. 147, n. 5, p. 354–358, oct 2000.

HONG, J. S.; LANCASTER, M. J. Canonical microstrip filter us-ing square open-loop resonators. *Electronics Letters*, v. 31, n. 23, p. 2020–2022, 1995.

HUNT, J.; GOLLUB, J.; DRISCOLL, T.; LIPWORTH, G.; MROZACK, A.; REYNOLDS, M. S.; BRADY, D. J.; SMITH, D. R. Metamaterial microwave holographic imaging system. *Journal of the Optical Society of America A*, v. 31, n. 10, p. 2109–2119, oct 2014.

IBM. *cplexbilpex*. 2019. Disponível em: <https://www.ibm.com/support/knowledgecenter/SSSA5P_12.9.0/ilog.odms.cplex.help/refmatlabcpex/html/cplexbilp-m.html>.

IPC STANDARDS. *Qualification and Performance Specification for High Fre-quency (Microwave) Printed Boards*. 2016.

JUPYTER. *Binary quadratic problems*. 2021. Disponível em: <<https://nbviewer.jupyter.org/github/MOSEK/Tutorials/blob/master/binary-quadratic/binquad.ipynb>>.

KHORASANINEJAD, M.; AIETA, F.; KANHAIYA, P.; KATS, M. A.; GENEVET, P.; ROUSSO, D.; CAPASSO, F. Achromatic metasurface lens at telecommunication wavelengths. *Nano Letters*, v. 16, p. 5235–5240, jul 2016.

KIM, Y.-D.; KIM, H.-J.; BAE, K.-U.; PARK, J.-H.; MYUNG, N.-H. A hybrid utd-acgf technique for doa finding of receiving antenna array on complex environment. *IEEE TRANSACTIONS ON ANTENNAS AND PROPAGATION, VOL. 63, NO. 11, NOVEMBER 2015*, v. 63, n. 11, p. 5044–5055, nov 2015.

KUESTER, E. F. *Theory of Waveguides and Transmission Lines*. first. Boca Raton, FL: CRC Press, 2021.

KYMETA. *METAMATERIAL-SURFACE FLAT-PANEL ANTENNA TECHNOLOGY*. [S.l.], 2019.

LEE, J.; SIEVENPIPER, D. F. Patterning technique for generating arbitrary anisotropic impedance surfaces. *IEEE Transactions on Antennas and Propagation*, v. 64, n. 11, p. 4725 – 4732, nov 2016.

LESUR, B.; MAATIA, A.; THEVENOT, M.; MENUDIER, C.; ARNAUD, E.; MONEDIERE, T.; MELLE, C.; CHAIMBAULT, D.; KARAS, A. A large antenna array for ka-band satcom-on-the-move applications—accurate modeling and experimental characterization. *IEEE TRANSACTIONS ON ANTENNAS AND PROPAGATION*, v. 66, n. 9, p. 4586–4595, sep 2018.

LI, A.; SINGH, S.; SIEVENPIPER, D. Metasurfaces and their applications. *De Gruyter Nanophotonics*, v. 7, n. 6, p. 989–1011, mar 2018.

LI, Y. B.; CAI, B. G.; CUI, T. J. Two-dimensional spoof surface plasmon polaritons for designing holographic metasurfaces. *2014 8th International Congress on Advanced Electromagnetic Materials in Microwaves and Optics*, aug 2014.

LI, Y. B.; CUI, T. J. Frequency multi-beam scanning in one diemnsion and two dimensions governed by holographic metasurfaces. *2015 International Workshop on Antenna Technology*, p. 16–17, may 2015.

LI, Y. B.; WAN, X.; CAI, B. G.; CHENG, Q.; CUI, T. J. Frequency-controls of electromagnetic multi-beam scanning by metasurfaces. *Scientific Reports*, v. 4, n. 6941, 2014.

LI, Y. B.; WU, R. Y.; WU, W.; SHI, C. B.; CHENG, Q.; CUI, T. J. Dual-physics manipulation of electromagnetic waves by system-level design of metasurfaces to reach extreme control of radiation beams. *Advanced Materials Technologies*, 2016.

LIM, S.; CALOZ, C.; ITOH, T. Metamaterial-based electronically controlled transmission-line structure as a novel leaky-wave antenna with tunable radiation angle and beamwidth. *IEEE Transactions on Microwave Theory and Technique*, v. 53, n. 1, p. 161 – 173, jan 2015.

LIM, W.; CHAN, K. Generation of multiple simultaneous beams with a modified blass matrix. *2009 Asia Pacific Microwave Conference*, p. 1557–1560, 2009.

LIPWORTH, G.; CAIRA, N. W.; LAROUCHE, S.; SMITH, D. R. Phase and magnitude constrained metasurface holography at w-band frequencies. *Optics Express*, v. 24, n. 17, p. 19372–19387, aug 2016.

LIPWORTH, G.; MROZACK, A.; HUNT, J.; MARKS, D. L.; DRISCOLL, T.; BRADY, D.; SMITH, D. R. Metamaterial apertures for coherent computational imaging on the physical layer. *Journal Optical Society of America*, v. 30, n. 08, p. 1603–1612, aug 2013.

LIU, Y.; ZHANG, W.; JIA, Y.; WU, A. Low rcs antenna array with reconfigurable scattering patterns based on digital antenna units. *IEEE TRANSACTIONS ON ANTENNAS AND PROPAGATION*, VOL. 69, NO. 1, JANUARY 2021, v. 69, n. 1, p. 572–577, jan 2021.

LIZUKA keigo. *Engineering Optics*. [S.l.]: Springer, 2008.

LUDWIG, R.; BRETCHKO, P. *RF Circuit Design Theory and Applications*. NJ,Piscataway: Prentice-Hall, 2000.

MACI G. MINATTI, M. C. S.; BOSILJEVAC, M. Metasurfing: Addressing waves on impenetrable metasurfaces. *IEEE ANTENNAS AND WIRELESS PROPAGATION LETTERS*, v. 10, p. 1499–1502, 2011.

MACI, S.; MINATTI, G.; CASALETTI, M.; BOSILJEVAC, M. Metasurfing: Addressing waves on impenetrable metasurfaces. *IEEE Antennas and Wireless Propagation Letters*, v. 10, p. 1499 – 1502, 2011.

MACOM. *GaAs Flip Chip PIN*. [S.l.], 2020.

MACOM-TECHNOLOGIES-SOLUTIONS. Application Note, *Desgin with PIN Diodes*.

MAILLOUX, R. J. *Phased Array Antenna Handbook*. MA,Norwood: Artech House, 2005.

MAILLOUX, R. J. *Electronically Scanned Arrays*. [S.l.]: Morgan and Claypool, 2007.

MAKHORIN, A. *Modeling Language GNU MathProg*. [S.l.], 2016.

MARTIN, N.; NANDAGOPAL, D.; KARA, M.; TRAN, V.; HAMILTON, S. Body fixed antenna options for seekers. *92 International Conference on Radar*, p. 272–275, 1992.

MATOS, S. A.; LIMA, E. B.; SILVA, J. R. C. J. S.; FERNANDES, C. A.; FONSECA, N. J. G.; MOSIG, J. R. High gain dual-band beam-steering transmit array for satcom terminals at ka-band. *IEEE TRANSACTIONS ON ANTENNAS AND PROPAGATION*, v. 65, n. 7, p. 3528–3539, jul 2017.

MINATTI, G.; CAMINITA, F.; MARTINI, E.; SABBADINI, M.; MACI, S. Synthesis of modulated-metasurface antennas with amplitude, phase, and polarization control. *IEEE Transactions on Antennas and Propagation*, v. 64, n. 9, p. 3907 – 3919, sep 2016.

MINATTI, G.; FAENZI, M.; MARTINI, E.; CAMINITA, F.; VITA, P. D.; GONZÁLEZ-OVEJERO, D.; SABBADINI, M.; MACI, S. Modulated metasurface antennas for space: Synthesis, analysis and realizations. *IEEE Transactions on Antennas and Propagation*, v. 63, n. 4, p. 1288 – 1300, apr 2015.

MOHAN, S. S.; HERSHENSON, M. del M.; BOYD, S. P.; LEE, T. H. Simple accurate expressions for planar spiral inductances. *IEEE JOURNAL OF SOLID-STATE CIRCUITS*, v. 34, n. 10, p. 1419–1424, oct 1999.

MOROTE, M. E.; DÍAZ, J. S. G.; CARRIER, J. P. Sinusoidally modulated graphene leaky-wave antenna for electronic beamscanning at thz. *IEEE Transactions on Terahertz Science and Technology*, v. 4, n. 1, p. 116 – 122, jan 2014.

MOVAHHEDI, M.; KARIMIPOUR, M.; KOMJANI, N. Multibeam bidirectional wideband/wide-scanning-angle holographic leaky-wave antenna. *IEEE Antennas and Wireless Propagation Letters*, v. 18, n. 7, p. 1507 – 1511, jul 2019.

- NOLEN, J. N. *Synthesis of Multiple Beam Networks for Arbitrary Illuminations*. Tese (Doutorado) — Bendix Corporation, Radio Division, Baltimore, apr 1965.
- OLINER, A. A.; HESSEL, A. Guided waves on sinusoidally-modulated reactance surfaces. *IRE Transactions on Antennas and Propagation*, p. 201–208, dec 1959.
- ORFANIDIS, S. J. *Electromagnetic Waves and Antennas*. NJ, Piscataway: Rutgers University, 2016.
- OVEJERO, D. G.; MACI, S. Gaussian ring basis functions for the analysis of modulated metasurface antennas. *IEEE Transactions on Antennas and Propagation*, v. 63, n. 9, p. 3982 – 3993, sep 2015.
- PALAZZI, V.; ALIMEN, F.; MEZZANOTTE, P.; ROSELLI, L. Novel magnitude and phase reconfigurable 1 x 4 rf power distribution network. *IEEE TRANSACTIONS ON MICROWAVE THEORY AND TECHNIQUES*, v. 69, n. 1, p. 29–42, jan 2021.
- PANDI, C. A. B. S.; BIRTCHER, C. R. Design of scalar impedance holographic metasurfaces for antenna beam formation with desired polarization. *IEEE TRANSACTIONS ON ANTENNAS AND PROPAGATION*, v. 63, n. 7, p. 3016–3024, jul 2015.
- PANDI, S.; BALANIS, C. A. Antenna beam forming using holographic artificial impedance surface. *2014 16th International Symposium on Antenna Technology and Applied Electromagnetics*, 2014.
- PFEIFFER, C.; GRBIC, A. Cascaded metasurfaces for complete phase and polarization control. *Applied Physics Letters*, v. 102, 2013.
- PFEIFFER, C.; GRBIC, A. Millimeter-wave transmitarrays for wavefront and polarization control. *IEEE Transaction Microwave Theory and Technique*, v. 61, p. 4407–4417, 2013.
- PRESSMAN, A. I. *Switching Power Supply Design*. second. [S.l.]: Mcgraw-Hill, 1998.
- RADI, Y.; SIMOVSKI, C.; TRETAKOV, S. Thin perfect absorbers for electromagnetic waves: Theory, design, and realizations. *PHYSICAL REVIEW APPLIED*, v. 3, mar 2015.
- RAHMAT-SAMII, Y.; HUANG, J.; LOPEZ, B.; LOU, M.; IM, E.; DURDEN, S. L.; BAHADORI, K. Advanced precipitation radar antenna: Array-fed offset membrane cylindrical reflector antenna. *IEEE TRANSACTIONS ON ANTENNAS AND PROPAGATION*, v. 53, n. 8, p. 2503–2515, aug 2005.
- RAMALINGAM, S.; BALANIS, C. A.; BIRTCHER, C. R. Polarization reconfigurable holographic artificial impedance surfaces. *2018 IEEE International Symposium on Antennas and Propagation & USNC/URSI National Radio Science Meeting*, jul 2018.
- REN, H.; ZHANG, H.; JIN, Y. G. Y.; ARIGONG, B. A novel 2-d 3 x 3 nolen matrix for 2-d beamforming applications. *IEEE TRANSACTIONS ON MICROWAVE THEORY AND TECHNIQUES*, v. 67, n. 11, p. 4622–4631, nov 2019.
- RIZZI, P. A. *Microwave Engineering: Passive Circuit*. first. Englewood Cliffs, NJ: Prentice Hall, 1987.
- ROTMAN, W.; TURNER, R. F. Wide-angle microwave lens for line source applications. *Trans. IEEE*, Ap-11, p. 623–632, nov 1963.
- RUSCH, C.; SCHAFFER, J.; GULAN, H.; PAHL, P.; ZWICK, T. Holographic mmw-antennas with te₀ and tm₀ surface wave launchers for frequency-scanning fmcw-radars. *IEEE Transactions on Antennas and Propagation*, v. 63, n. 4, p. 1603 – 1613, apr 2015.
- SANTANA, M. P.; BARBOSA, E. V. S.; RONDINEAU, S. R. M. J. Design of ku-band filters and diplexer for a heterodyne transceiver using coupled open-loop resonator cells. *2020 Workshop on Communication Networks and Power Systems (WCNPS)*, nov 2020.

SIEVENPIPER, D.; SCHAFFNER, J.; LOO, R.; TANGONAN, G.; ONTIVEROS, S.; HAROLD, R. A tunable impedance surface performing as a reconfigurable beam steering reflector. *IEEE Transactions on Antennas and Propagation*, v. 50, n. 3, p. 384 – 390, mar 2002.

SIEVENPIPER, D.; SCHAFFNER, J.; SONG, H.; LOO, R.; TANGONAN, G. Two-dimensional beam steering using an electrically tunable impedance surface. *IEEE Transactions on Antennas and Propagation*, v. 51, n. 10, p. 2713 – 2722, oct 2003.

SIEVENPIPER, D.; ZHANG, L.; BROAS, R. F. J.; ALEXOPOLOUS, N. G.; YABLONOVITCH, E. High-impedance electromagnetic surfaces with a forbidden frequency band. *IEEE Transaction Microwave Theory and Technique*, v. 47, p. 2059–2074, 1999.

SIEVENPIPER, D. F. Forward and backward leaky wave radiation with large effective aperture from an electronically tunable textured surface. *IEEE Transactions Antennas and Propagation*, v. 53, p. 236–247, 2005.

SINGH, K.; AFZAL, M. U.; KOVALEVA, M.; ESSELLE, K. P. Controlling the most significant grating lobes in two-dimensional beam-steering systems with phase-gradient metasurfaces. *IEEE TRANSACTIONS ON ANTENNAS AND PROPAGATION*, v. 68, n. 3, p. 1389–1401, mar 2020.

SINGH, P. K.; HOPWOOD, J.; SONKUSALE, S. Metamaterials for remote generation of spatially controllable two dimensional array of microplasma. *Scientific Reports*, v. 4, p. 1–5, aug 2014.

SMITH, D. R.; PENDRY, J. B.; WILTSHIRE, M. C. K. Metamaterials and negative refractive index. *Science*, v. 305, p. 788–792, aug 2004.

SOUNAS, D. L.; FLEURY, R. Unidirectional cloaking based on metasurfaces with balanced loss and gain. *PHYSICAL REVIEW APPLIED*, v. 4, jul 2015.

STEVENSON, R.; SAZEGAR, M.; BILY, A.; JOHNSON, M.; KUNDTZ, N. Metamaterial surface antenna technology: Commercialization through diffractive metamaterials and liquid crystal display manufacturing. *10th International Congress on Advanced Electromagnetic Materials in Microwaves and Optics – Metamaterials 2016*, p. 349–351, sep 2016.

STMICROELECTRONICS. *Application note: LED array drivers*. [S.l.], 2012. Rev. 1.

STMICROELECTRONICS. *Low voltage 16-bit constant current LED sink driver*. [S.l.], 2017. Rev. 6.

STUTZMAN, W. L.; THIELE, G. L. *Antenna Theory and Design*. MA, Danvers: John Wiley and Sons, 2013.

TAI, C.-T. *Dyadic Green Functions in Electromagnetic Theory*. NJ, Piscataway: IEEE PRESS, 1994.

TAN, Y.; JI, W.; LI, L. Analysis of frequency-controlled beam scanning based on holographic metasurface. *2015 Asia-Pacific Microwave Conference (APMC)*, dec 2015.

TOLIN, E.; LITSCHKE, O.; BRUNI, S. Compact extended scan range antenna array based on rotman lens. *IEEE TRANSACTIONS ON ANTENNAS AND PROPAGATION*, v. 67, n. 12, p. 7356–7367, dec 2019.

TSOKOS, C.; MYLONAS, E.; GROUMAS, P.; KATOPODIS, V.; GOUNARIDIS, L.; TIMENS, R. B.; OLDENBEUVING, R. M.; ROELOFFZEN, C. G. H.; AVRAMOPOULOS, H.; KOULOUMENTAS, C. Analysis of a multibeam optical beamforming network based on blazed matrix architecture. *JOURNAL OF LIGHTWAVE TECHNOLOGY, VOL. 36, NO. 16, AUGUST 15, 2018*, v. 36, n. 16, p. 3354–3372, aug 2018.

VERMA, Y. K. Design challenges of realizing an active radar seeker at ka-band. *2017 IEEE MTT-S International Microwave and RF Conference (IMaRC)*, p. 172–175, 2017.

VIGANO, M. C.; RÍO, D. L. del; BONGARD, F.; VACCARO, S. Sparse array antenna for ku-band mobile terminals using 1 bit phase controls. *IEEE Transactions on Antennas and Propagation*, v. 62, n. 4, p. 1723 – 1730, apr 2014.

WANG, X.; CALOZ, C. Spread-spectrum selective camouflaging based on time-modulated metasurface. *IEEE TRANSACTIONS ON ANTENNAS AND PROPAGATION*, v. 69, n. 1, p. 286–295, jan 2021.

WHITE, J. F. *Microwave Semiconductor Engineering*. NY, New York: Van Nostrand Reinhold Company, 1982.

WU, Y. F.; CHENG, Y. J.; HUANG, Z. X. Ka-band near-field-focused 2-d steering antenna array with a focused rotman lens. *IEEE TRANSACTIONS ON ANTENNAS AND PROPAGATION*, v. 66, n. 10, p. 5204–5213, oct 2018.

YU, H.; DING, X.; ZHANG, K.; WU, Q. Beam reconfigurable antenna based on holographic metasurfaces. *2018 IEEE International Symposium on Antennas and Propagation & USNC/URSI National Radio Science Meeting*, p. 485–486, jul 2018.

YU, Y.; HONG, W.; JIANG, Z. H.; ZHANG, H. A hybrid radar system with a phased transmitting array and a digital beamforming receiving array. *IEEE Transactions on Antennas and Propagation*, p. 1–12, 2020.

YUAN, Q.; CHEN, Q.; SAWAYA, K. Accurate doa estimation using array antenna with arbitrary geometry. *IEEE TRANSACTIONS ON ANTENNAS AND PROPAGATION*, v. 53, n. 4, p. 1352–1357, apr 2005.

YURDUSEVEN, O.; MARKS, D. L.; GOLLUB, J. N.; SMITH, D. R. Design and analysis of a reconfigurable holographic metasurface aperture for dynamic focusing in the fresnel zone. *IEEE Access*, v. 5, p. 15055–15065, 2017.

YURDUSEVEN, O.; SMITH, D. R. Dual-polarization printed holographic multibeam metasurface antenna. *IEEE ANTENNAS AND WIRELESS PROPAGATION LETTERS*, v. 16, p. 2738–2741, 2017.

ZHANG, C.; DENG, L.; ZHU, J.; LI, S. F.; WANG, L.; HONG, W.; LIU, L.; WANG, H. J.; WANG, X. X.; ZENG, T. A circularly polarized metasurface antenna based on holographic method. *2019 International Conference on Microwave and Millimeter Wave Technology (ICMMT)*, 2019.

ZHANG, X.; ZHANG, Q.; CHEN, C.; CHEN, W.; LIU, B.; CAI, J. Design of holographic metasurface for antenna beam steering based on liquid crystal technology. *2018 Asia-Pacific Microwave Conference*, p. 1372–1374, oct 2018.

ZHENG, D.; LYU, Y.-L.; WU, K. Transversely slotted siw leaky-wave antenna featuring rapid beam-scanning for millimeter-wave applications. *IEEE TRANSACTIONS ON ANTENNAS AND PROPAGATION*, v. 68, n. 6, p. 4172–4185, jun 2020.

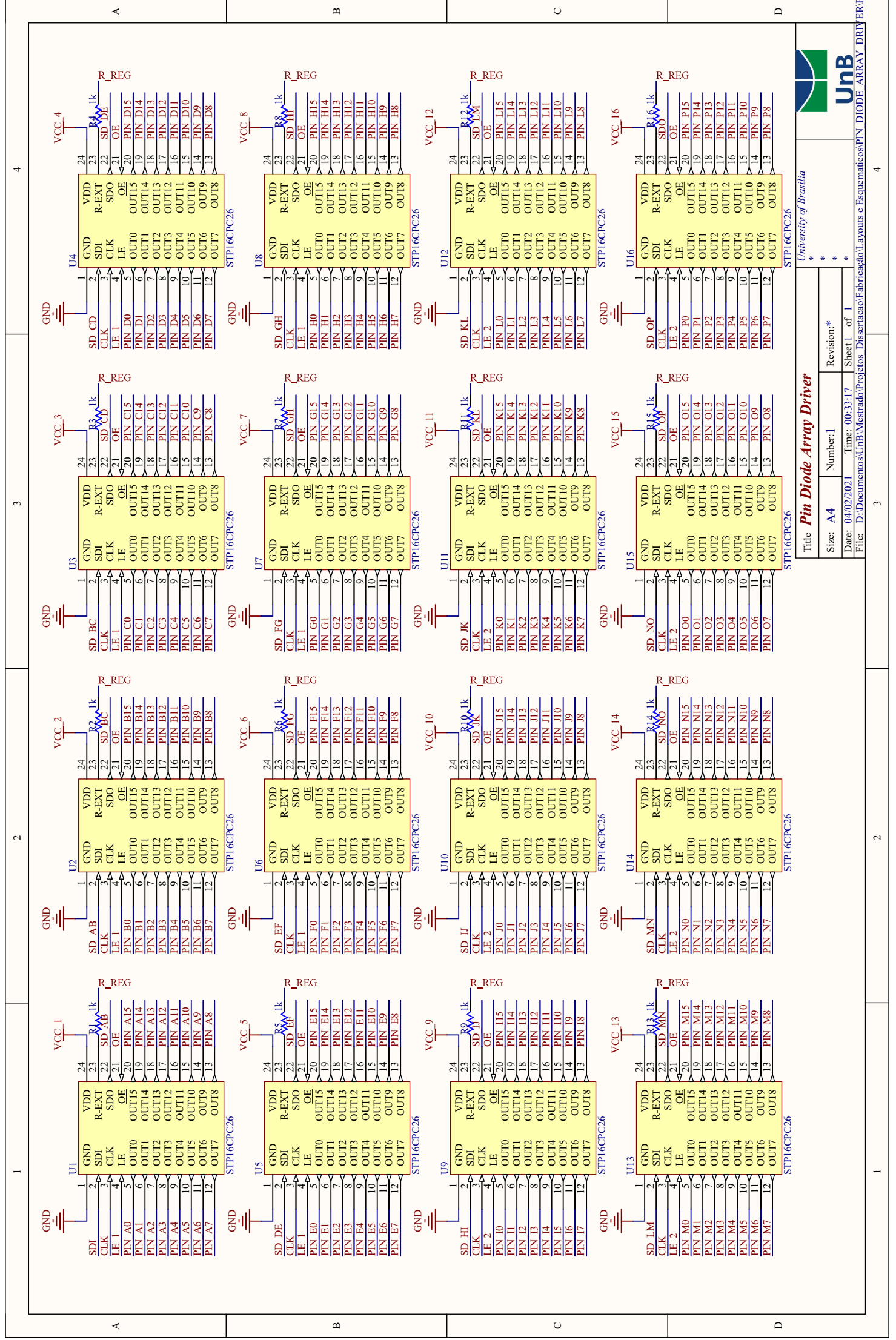
ZHENG, Z.; FU, M.; WANG, W.-Q.; SO, H. C. Symmetric displaced coprime array configurations for mixed near- and far-field source localization. *IEEE TRANSACTIONS ON ANTENNAS AND PROPAGATION*, v. 69, n. 1, p. 465–, jan 2021.

ZHU, B.; WANG, Z.; HUANG, C.; ZHAO, Y. F. J.; JIANG, T. Polarization insensitive metamaterial absorber with wide incident angle. *Progress In Electromagnetics Research*, v. 101, p. 231–239, 2010.

APPENDICES

I. 16-BIT CONSTANT CURRENT LED SINK DRIVER - CONTROL CIRCUIT

I.1 CIRCUITS SCHEMATICS



Title Pin Diode Array Driver
Size: A4
Number: 1
Date: 04/02/2021
Time: 00:33:17
File: D:\Documentos\UnB\Mestrado\Projetos Dissertacao\Fabricacao\Layouts e Esquemáticos\PIN_DIODE_ARRAY_DRIVER.PIN



University of Brasilia
 *
 *
 *
 *

Revision:*	Sheet 1 of 1

4

3

2

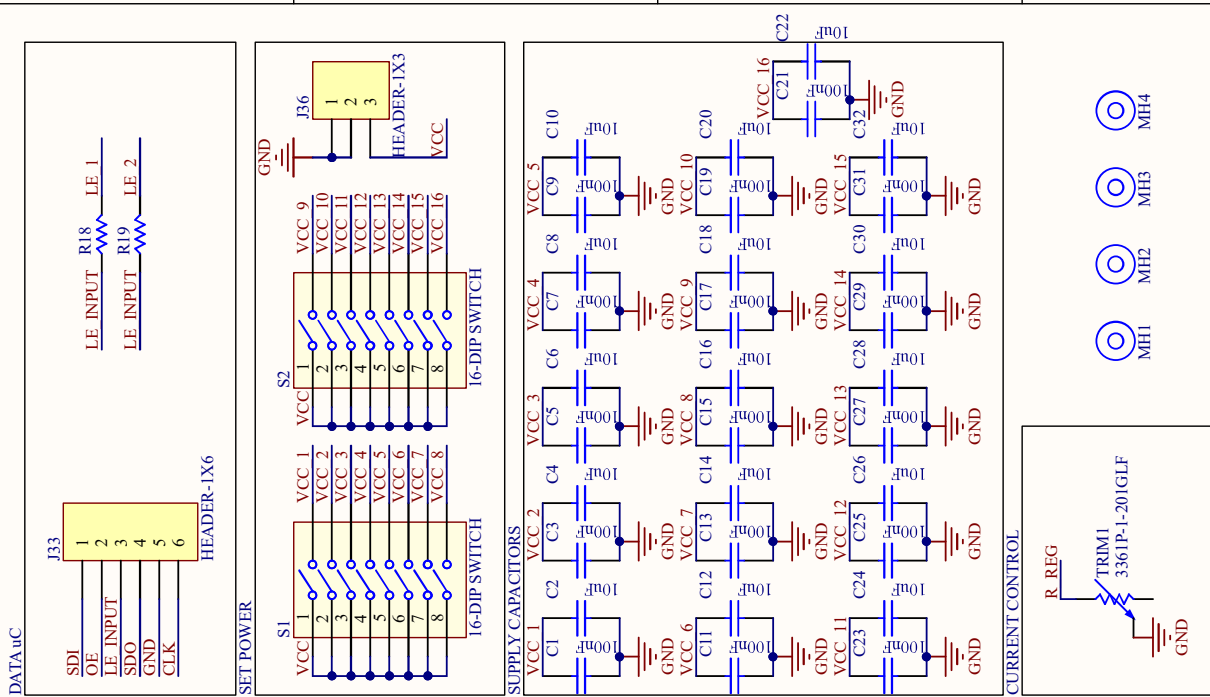
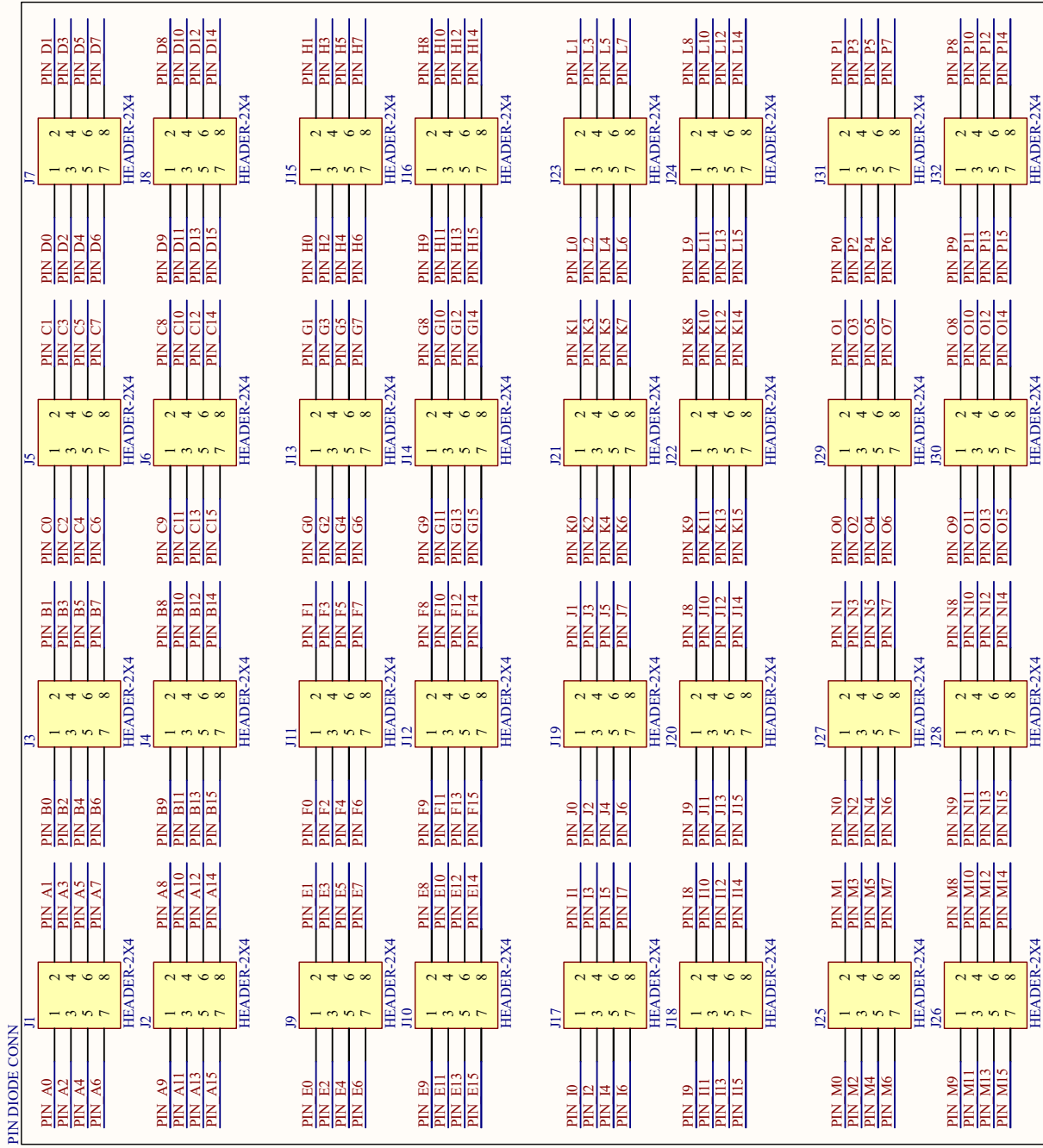
1

4

3

2

1



Connectors and Headers

University of Brasilia

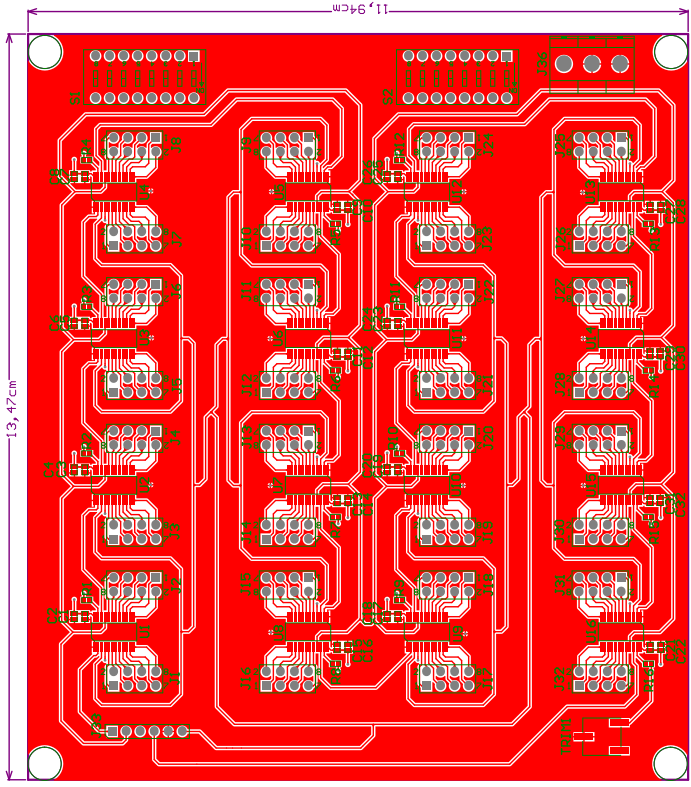
Title	Connectors and Headers
Size:	A4
Number:	2
Date:	04/02/2021
Time:	00:33:18
Revision:	*
Sheet 1 of 1	*
File:	D:\Documentos\UnB\Mestrado\Projetos Dissertacao\Fabricacao\Layouts e Esquematicos\CONN_SchDoc

I.2 PCB LAYOUT

PCB SPECIFICATIONS

DATE:	Rev: 1.0 mm A-100
LAYERS:	Double Layer PCB 2 copper layers
TOP FINISHING:	<input type="checkbox"/> HAS (Not for solder coating) - PC-1000 <input checked="" type="checkbox"/> HAS (Business related Innovation gold) <input type="checkbox"/> HAS (Not for EN) - 1000 mm μm (Au) - PC-1000
CAD FILE MAP:	
SUPPLIER:	
W. PAPER:	<input checked="" type="checkbox"/> A4 <input type="checkbox"/> A3 <input type="checkbox"/> A2 <input type="checkbox"/> Project
NOTES (PLEASE CHANGE SECTION):	

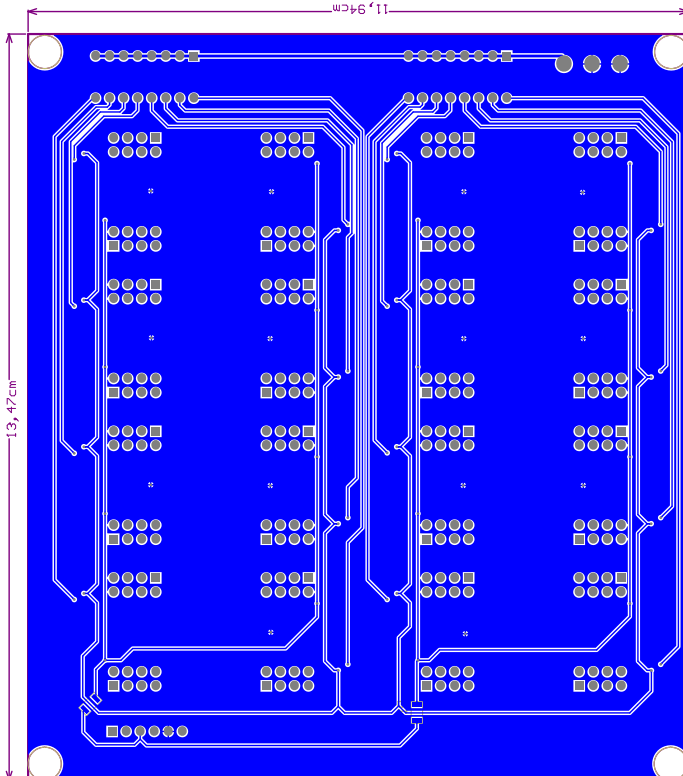
Layer Name	Material	Thickness	Constant
Top Overlay	SI-001	0,025mm	4
Top Solder	Copper	0,035mm	
Top Layer	FR-4	1,600mm	4, 3
Dielectric 1	Copper	0,035mm	
Bottom Layer	SI-001	0,025mm	4
Bottom Solder			
Bottom Overlay			



DATE:	Rev: 1.0 mm A-100	Project:	Project	Layer:	Layer 3	Unit:	Unit
DESIGNER:		Company:	Company	Rev:	Rev: 1	Page:	Page 2
ETCHER:		Date:	07/05/2009				
DRIVER:							

PCB SPECIFICATIONS	
DATE:	Rev: 1.0 mm / 1-100
LAYERS:	Design: PCB 2 - 2024-0001
DESIGN:	<input type="checkbox"/> No Plating <input checked="" type="checkbox"/> HAS (has a Silver coating) - PC-1050 <input checked="" type="checkbox"/> HAS (has a Gold Immersion) - 2024-0001 - 100mm - 100mm - PC-1050
DESIGN MGR:	
DESIGNER:	
W. PAGES:	<input checked="" type="checkbox"/> Top <input type="checkbox"/> Bottom <input type="checkbox"/> Project
NOTES (PLEASE CHANGE SECTION)	

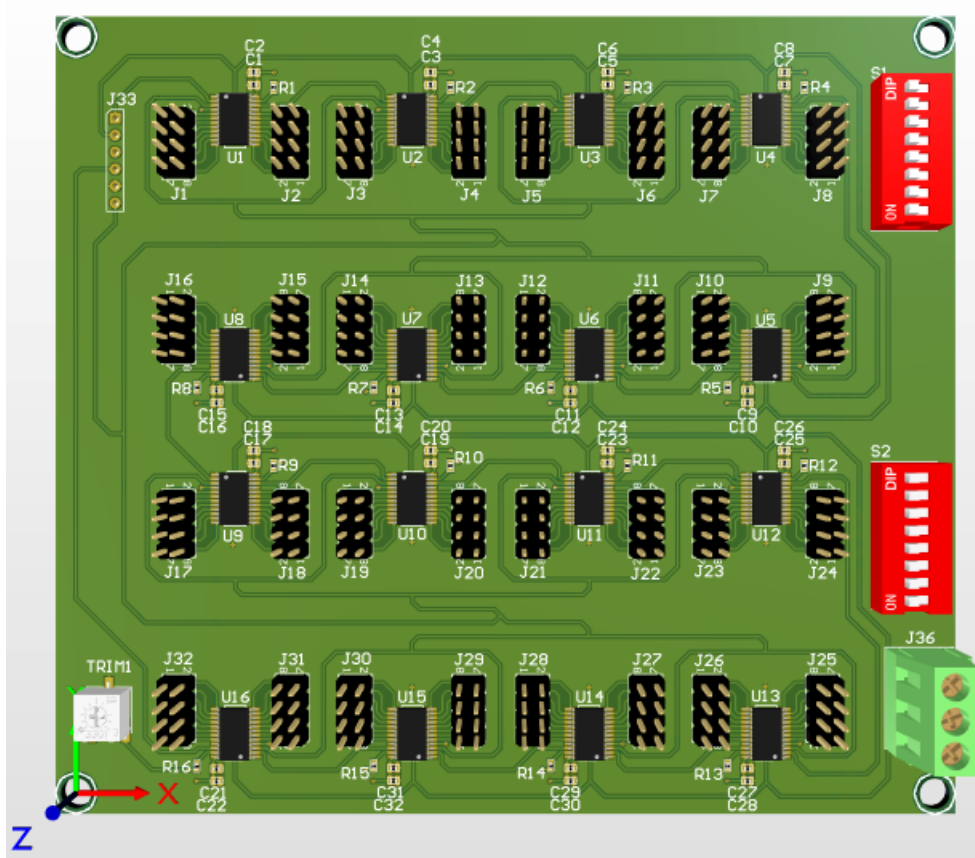
Layer Name	Material	Thickness	Constant
Top Overlay	SM-001	0,025mm	4
Top Solder	Copper	0,035mm	
Top Layer	FR-4	1,600mm	4, 3
Dielectric 1	Copper	0,035mm	
Bottom Layer	SM-001	0,025mm	4
Bottom Solder			
Bottom Overlay			



COMPANY:	DATE:	DESIGNER:	PROJECT:	DATE:	REV:	DESCRIPTION:	DATE:	REV:	DESCRIPTION:
STAVROPOULOS	07/02/2024	STAVROPOULOS	PCB 2 - 2024-0001	07/02/2024	1	Initial Design	07/02/2024	1	Initial Design
STAVROPOULOS		STAVROPOULOS	PCB 2 - 2024-0001		2	Final Design		2	Final Design
STAVROPOULOS		STAVROPOULOS	PCB 2 - 2024-0001		3	Manufacturing		3	Manufacturing
STAVROPOULOS		STAVROPOULOS	PCB 2 - 2024-0001		4	Assembly		4	Assembly
STAVROPOULOS		STAVROPOULOS	PCB 2 - 2024-0001		5	Testing		5	Testing
STAVROPOULOS		STAVROPOULOS	PCB 2 - 2024-0001		6	Delivery		6	Delivery
STAVROPOULOS		STAVROPOULOS	PCB 2 - 2024-0001		7	Support		7	Support
STAVROPOULOS		STAVROPOULOS	PCB 2 - 2024-0001		8	Archive		8	Archive

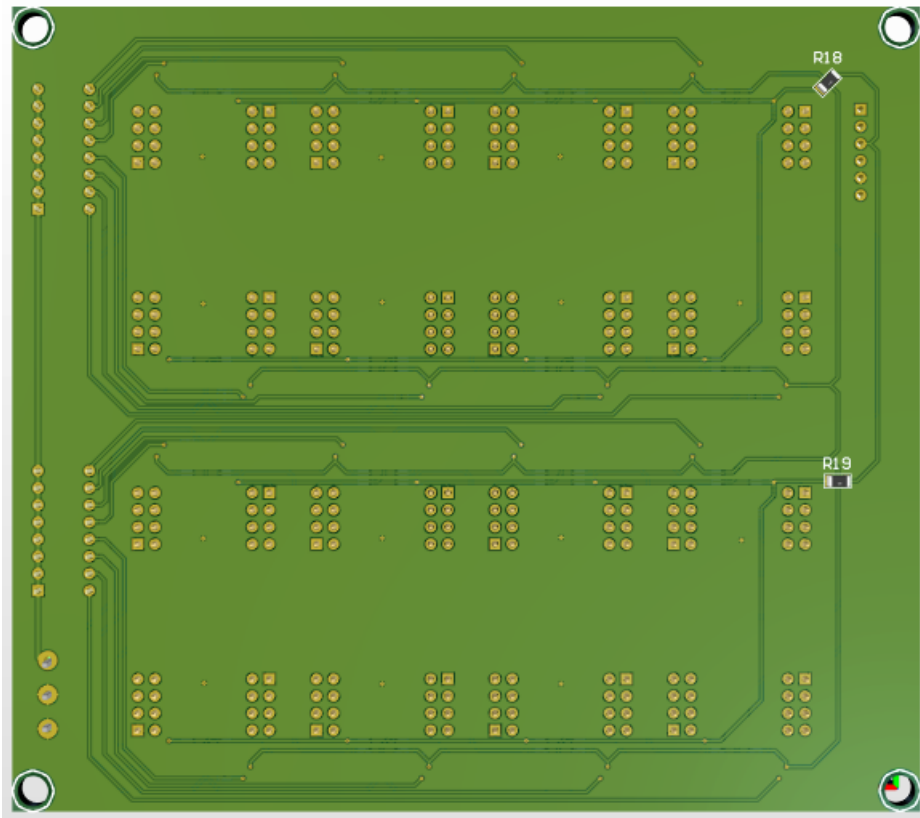
I.3 CIRCUIT 3D VIEWS

Figure I.1: 16-bit constant current LED sink driver control circuit 3D top view.



Source: Own authorship.

Figure I.2: 16-bit constant current LED sink driver control circuit 3D bottom view.

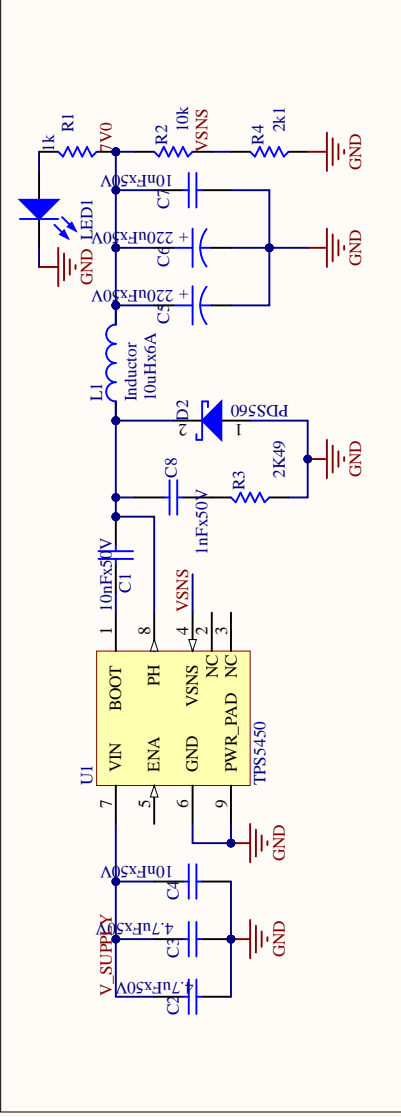


Source: Own authorship.

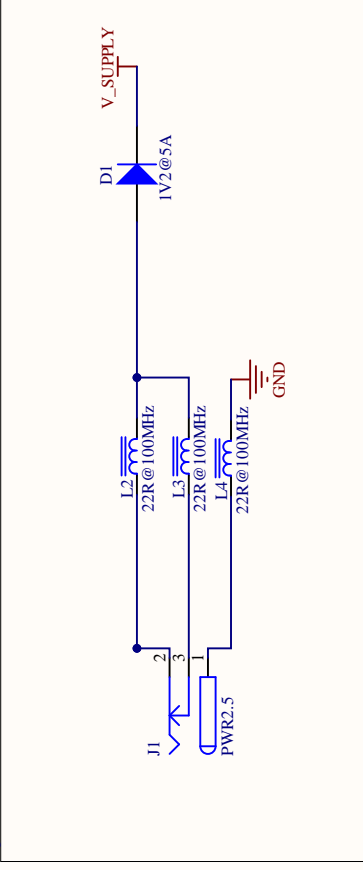
II. POWER SUPPLY BOARD

II.1 CIRCUITS SCHEMATICS

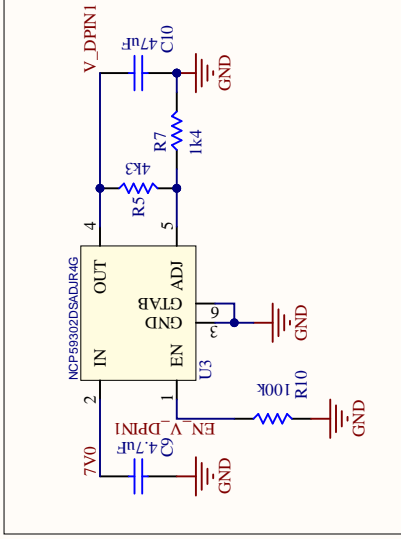
Buck Source 7V0



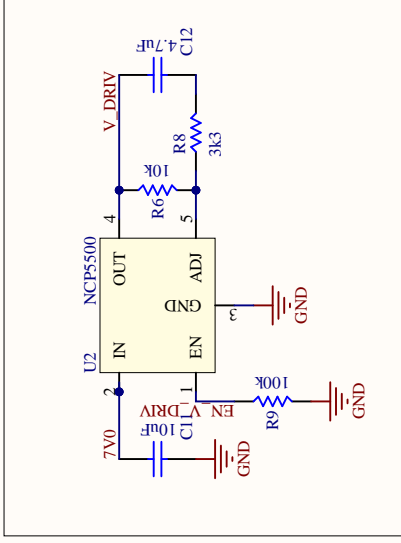
Input Connector



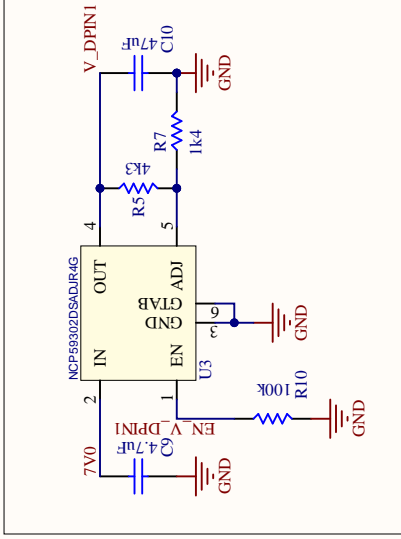
LDO DPIN1 5V0



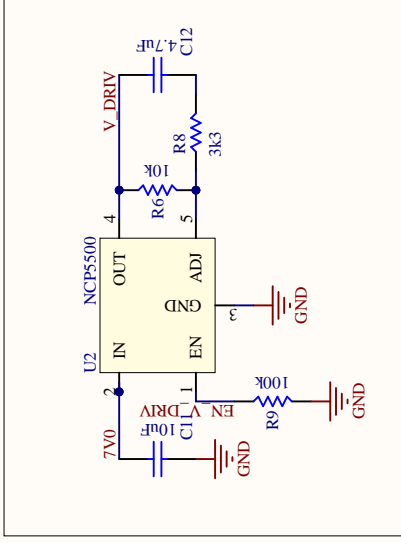
LDO DRIV 5V0



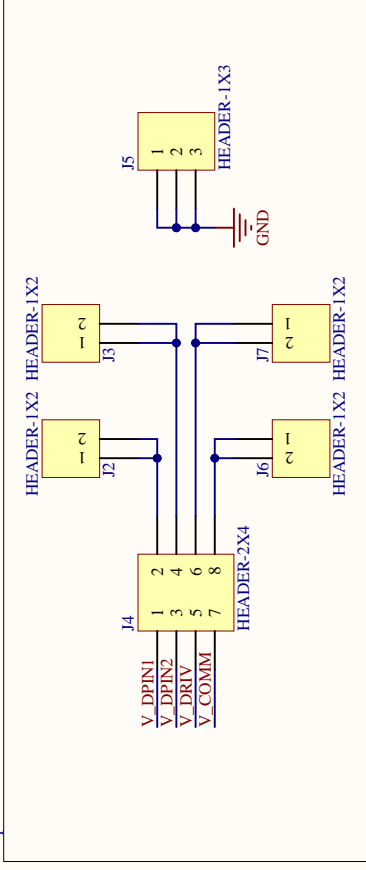
LDO DPIN2 5V0



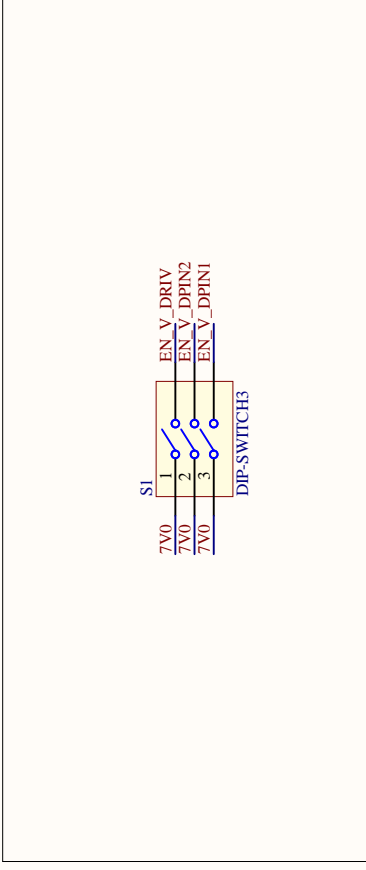
LDO COMM 3V3



Output Connector



Enable



LDO DPIN2 5V0



LDO COMM 3V3



Title Step-Down Conv. and LDOs

University of Brasilia



Size: A4	Number: 1	Revision: Matheus P.
Date: 05/02/2021	Time: 23:58:49	Sheet 1 of 2
File: D:\Documentos\UnB\Mestrado\Projetos_Dissertacao\Fabricacao\Layouts e Esquemáticos\POWER_SUPPLY_BOARD\DOWN		*

II.2 PCB LAYOUT

PCB SPECIFICATIONS

DATE: 11/18/2024

DESIGNER: [Name]

DATE: 11/18/2024

PROJECT: [Project Name]

VERSION: 1.0

REVISIONS:

NO.	DESCRIPTION	DATE
1	Initial Release	11/18/2024

NOTES:

1. All dimensions are in millimeters unless otherwise specified.

2. Tolerances are as per IPC standards.

3. All materials must be UL94V-0 flame retardant.

4. All components must be RoHS compliant.

5. All components must be lead-free.

6. All components must be halogen-free.

7. All components must be REACH compliant.

8. All components must be WEEE compliant.

9. All components must be CE compliant.

10. All components must be FCC compliant.

11. All components must be EMC compliant.

12. All components must be ESD compliant.

13. All components must be IEC compliant.

14. All components must be ISO compliant.

15. All components must be JIS compliant.

16. All components must be MIL compliant.

17. All components must be NEMA compliant.

18. All components must be NFPA compliant.

19. All components must be OSHA compliant.

20. All components must be ANSI compliant.

21. All components must be ASME compliant.

22. All components must be ASTM compliant.

23. All components must be AWS compliant.

24. All components must be ASCE compliant.

25. All components must be AIAA compliant.

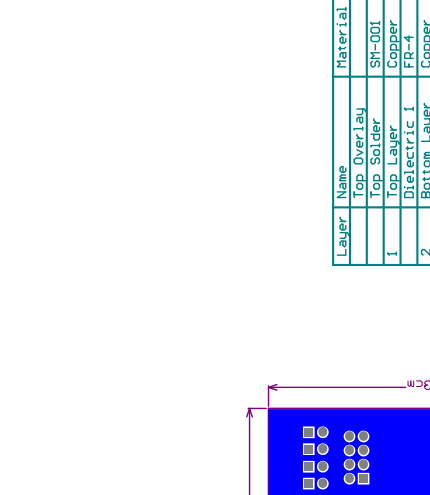
26. All components must be AIA compliant.

27. All components must be AIAA compliant.

28. All components must be AIAA compliant.

29. All components must be AIAA compliant.

30. All components must be AIAA compliant.



Layer	Name	Material	Thickness	Constant	Board Layer Stack
	Top Overlay	SH-001	0,025mm	4	FR4
	Top Solder	Copper	0,035mm		FR4
1	Top Layer	FR-4	1,600mm	4,3	FR4
	Dielectric 1	Copper	0,035mm		FR4
2	Bottom Layer	SH-001	0,025mm	4	FR4
	Bottom Solder	Copper	0,035mm		FR4
	Bottom Overlay	SH-001	0,025mm	4	FR4

PCB SPECIFICATIONS

DATE: 11/18/2024

DESIGNER: [Name]

DATE: 11/18/2024

PROJECT: [Project Name]

VERSION: 1.0

REVISIONS:

NO.	DESCRIPTION	DATE
1	Initial Release	11/18/2024

NOTES:

1. All dimensions are in millimeters unless otherwise specified.

2. Tolerances are as per IPC standards.

3. All materials must be UL94V-0 flame retardant.

4. All components must be RoHS compliant.

5. All components must be lead-free.

6. All components must be halogen-free.

7. All components must be REACH compliant.

8. All components must be WEEE compliant.

9. All components must be CE compliant.

10. All components must be FCC compliant.

11. All components must be EMC compliant.

12. All components must be ESD compliant.

13. All components must be IEC compliant.

14. All components must be ISO compliant.

15. All components must be JIS compliant.

16. All components must be MIL compliant.

17. All components must be NEMA compliant.

18. All components must be NFPA compliant.

19. All components must be OSHA compliant.

20. All components must be ANSI compliant.

21. All components must be ASME compliant.

22. All components must be ASTM compliant.

23. All components must be AWS compliant.

24. All components must be ASCE compliant.

25. All components must be AIAA compliant.

26. All components must be AIA compliant.

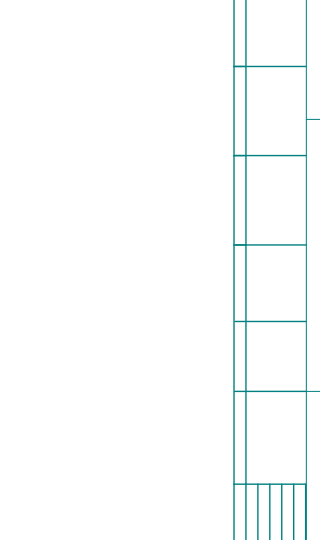
27. All components must be AIAA compliant.

28. All components must be AIAA compliant.

29. All components must be AIAA compliant.

30. All components must be AIAA compliant.

Layer	Name	Material	Thickness	Constant	Board Layer Stack
	Top Overlay	SH-001	0,025mm	4	FR4
	Top Solder	Copper	0,035mm		FR4
1	Top Layer	FR-4	1,600mm	4,3	FR4
	Dielectric 1	Copper	0,035mm		FR4
2	Bottom Layer	SH-001	0,025mm	4	FR4
	Bottom Solder	Copper	0,035mm		FR4
	Bottom Overlay	SH-001	0,025mm	4	FR4



PCB SPECIFICATIONS

DATE: 11/18/2024

DESIGNER: [Name]

DATE: 11/18/2024

PROJECT: [Project Name]

VERSION: 1.0

REVISIONS:

NO.	DESCRIPTION	DATE
1	Initial Release	11/18/2024

NOTES:

1. All dimensions are in millimeters unless otherwise specified.

2. Tolerances are as per IPC standards.

3. All materials must be UL94V-0 flame retardant.

4. All components must be RoHS compliant.

5. All components must be lead-free.

6. All components must be halogen-free.

7. All components must be REACH compliant.

8. All components must be WEEE compliant.

9. All components must be CE compliant.

10. All components must be FCC compliant.

11. All components must be EMC compliant.

12. All components must be ESD compliant.

13. All components must be IEC compliant.

14. All components must be ISO compliant.

15. All components must be JIS compliant.

16. All components must be MIL compliant.

17. All components must be NEMA compliant.

18. All components must be NFPA compliant.

19. All components must be OSHA compliant.

20. All components must be ANSI compliant.

21. All components must be ASME compliant.

22. All components must be ASTM compliant.

23. All components must be AWS compliant.

24. All components must be ASCE compliant.

25. All components must be AIAA compliant.

26. All components must be AIA compliant.

27. All components must be AIAA compliant.

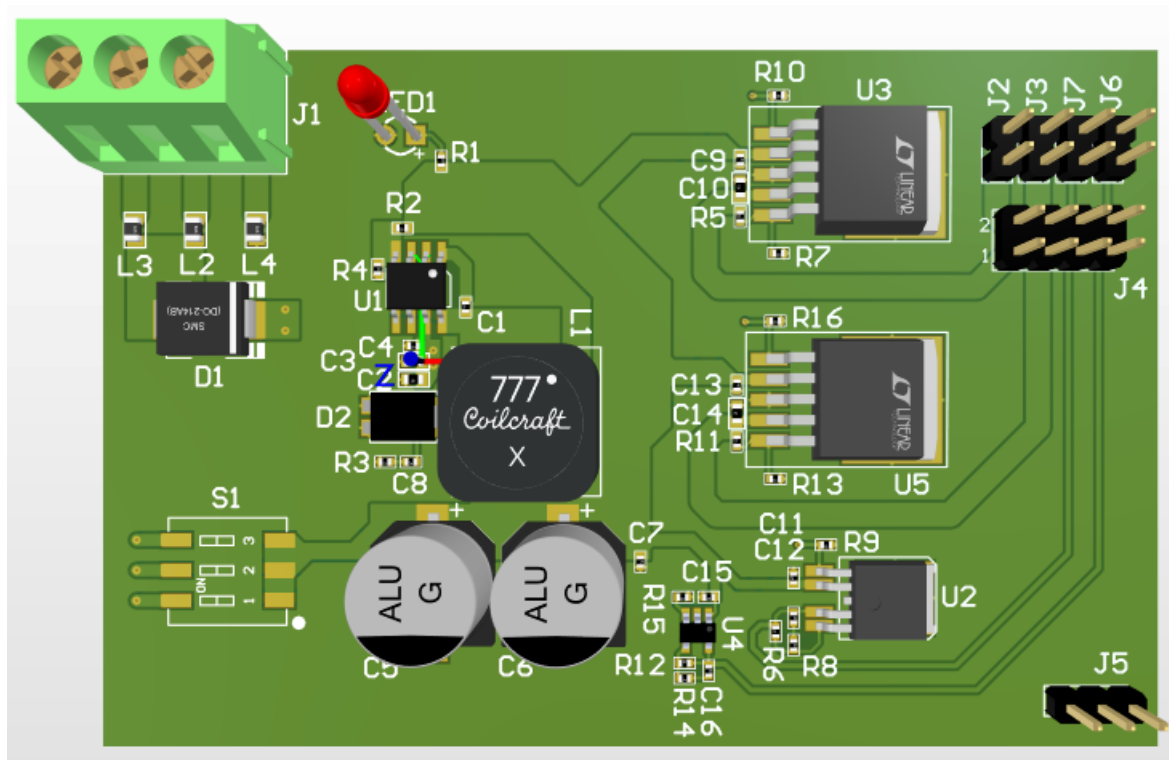
28. All components must be AIAA compliant.

29. All components must be AIAA compliant.

30. All components must be AIAA compliant.

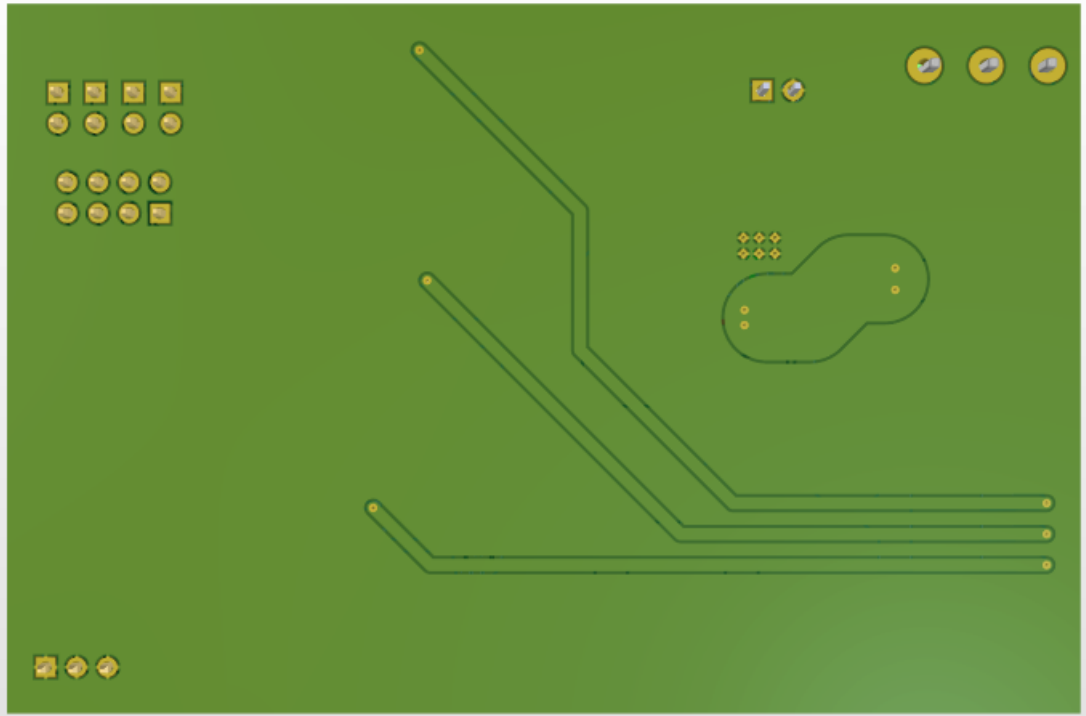
II.3 CIRCUIT 3D VIEWS

Figure II.1: 16-bit constant current LED sink driver control circuit 3D top view.



Source: Own authorship.

Figure II.2: 16-bit constant current LED sink driver control circuit 3D bottom view.



Source: Own authorship.

III. MATLAB CODES

III.1 HOLOGRAPHIC PROCEDURE

```
1 %%
2 % Program: Hologram_Generation.m;
3 % Type: Script;
4 % Function: Calculate the hologram to create the array factor with one beam;
5 % Author: Matheus Pereira Santana.
6
7 %%
8 clear all;
9 close all;
10 clc;
11
12 %%
13 % Variables
14
15 N = 16; % Number of elements in X-axis.
16 M = 16; % Number of elements in Y-axis.
17 f = 12e9; % Frequency.
18 c = 3e8; % Light velocity.
19 lambda = c/f; % Free-space wavelength.
20 er = 4.5; % Dielectric constant of the medium.
21 lambda_g = lambda/sqrt(er); % Guided wavelength.
22 dx = lambda_g/2; % Inter-space elements in X-axis.
23 dy = lambda_g/2; % Inter-space elements in Y-axis.
24
25 %%
26 % Space Coordinates
27
28 theta0 = 0:pi/36:pi; % Elevation
29 phi0 = 0:pi/18:2*pi; % Azimuth
30 [phi,theta] = meshgrid(phi0,theta0); % Coordinate mesh.
31 sinU = sin(theta).*cos(phi); % U-sine space.
32 sinV = sin(theta).*sin(phi); % V-sine space.
33
34 %%
35 % Antenna position
36
37 Px = -(N-1)/2:1:(N-1)/2; % Position index in X-axis.
38 Py = -(M-1)/2:1:(M-1)/2; % Position index in Y-axis.
39 Px2d = dx*meshgrid(Px); % Array of positions.
40 Py2d = dy*meshgrid(Py)'; % Array of positions.
41
42 %%
43 % Excitation array
```



```

44
45 theta_p = 20; % Desired elevation direction.
46 phi_p = 60; % Desired Azimuth direction.
47
48 S_w = ones(N,M); % Amplitude array.
49 S_phase = ((2*pi/lambda)*Px2d*sind(theta_p)*cosd(phi_p)
50 + (2*pi/lambda)*Py2d*sind(theta_p)*sind(phi_p)); % Phase array.
51
52 S = S_w.*exp(-1i*S_phase); % Excitation array.
53
54 %%
55 % Cavity phase
56
57 P_r = sqrt(Px2d.^2+Py2d.^2); % Array of radius.
58 P_phase = atan2d(Py2d,Px2d); % Array of phases.
59
60 Hx = besselh(0,1,(2*pi/lambda_g)*P_r).*cosd(P_phase); % Magnetic field - ...
    X-component - Zero order hankel function of the first kind.
61 Hy = besselh(0,1,(2*pi/lambda_g)*P_r).*sind(P_phase); % Magnetic field - ...
    Y-component - Zero order hankel function of the first kind.
62
63 %%
64 % Hologram calculation - Array pattern synthesis
65
66 phase_threshold = 90; % Phase threshold.
67
68 Hologram_phase = 180*S_phase/pi+180*angle(Hy)/pi; % Hologram phase recording.
69 Hologram = zeros(N,M); % Hologram array
70
71 n_ant = 0;
72
73 for n = 1:1:N
74     for m = 1:1:M
75         if abs(Hologram_phase(n,m)) <= phase_threshold % Applaing phase threshold.
76             Hologram(n,m) = 1; % Hologram recording.
77             n_ant = n_ant+1;
78         else
79             continue;
80         end
81     end
82 end
83
84 %%
85 % Hologram calculation - Beam projection
86
87 D = (max(max(P_r))*2); % Maximum dimension of the array.
88
89 rho = 2*(D*D)/lambda; % Radius of projection
90
91 x0 = rho*sind(theta_p)*cosd(phi_p); % X-projection.
92 y0 = rho*sind(theta_p)*sind(phi_p); % Y-projection.
93 z0 = rho*cosd(theta_p); % Z-projection.

```

```

94
95 r_line = [x0 y0 z0]; % .
96 beam_projection = zeros(N,M); % Projection array creation.
97
98 for n = 1:N
99     for m = 1:M
100         % Beam projection using spheric wave.
101         beam_projection(n,m) = exp(1i*(2*pi/lambda)*norm([Px2d(n,m) Py2d(n,m) ...
102                 0]-r_line))/norm([Px2d(n,m) Py2d(n,m) 0]-r_line);
103     end
104 end
105 beam_phase = angle(beam_projection)*180/pi;% Beam projection phase
106
107 %%
108 % Hologram recording using beam projection
109
110 Hologram_phase_2 = beam_phase-180*angle(Hy)/pi; % Hologram phase recording.
111
112 Hologram2 = zeros(N,M); % Hoograma array.
113 n_ant_2 = 0;
114
115 for n = 1:1:N
116     for m = 1:1:M
117         if abs(Hologram_phase_2(n,m)) ≤ phase_threshold % Applying phase ...
118             threshold.
119             Hologram2(n,m) = 1; % Hologram recording.
120             n_ant_2 = n_ant_2+1;
121         else
122             continue;
123         end
124     end
125 end
126 %%
127 % Ideal array factor calculation
128
129 af = zeros(length(theta0),length(phi0)); % AF array.
130
131 for n = 1:1:N
132     for m =1:1:M
133         af =af+S(n,m)*exp((1i*2*pi/lambda)*(Px2d(n,m)*sinU+Py2d(n,m)*sinV));% ...
134         Ideal array factor calculation
135     end
136 end
137
138
139 %%
140 % Array pattern synthesis array factor
141
142 S_APS = Hologram.*exp(1i*angle(Hy)); % APS excitation

```

```

143 af_APS = zeros(length(theta0),length(phi0)); % APS array.
144
145 for n = 1:1:N
146     for m =1:1:M
147         af_APS =af_APS + S_APS(n,m).*exp((1i*2*pi/lambda)*(Px2d(n,m)*sinU + ...
148             Py2d(n,m)*sinV)); % APS array calculation
149     end
150 end
151 %%
152 % % BP Hologram array factor
153
154 S_BP = (Hologram2).*exp( 1i*angle(Hy)); % BP excitation
155 af_BP = zeros(length(theta0),length(phi0)); % BP array.
156
157 for n = 1:1:N
158     for m =1:1:M
159         af_BP =af_BP + S_BP(n,m).*exp((1i*2*pi/lambda)*(Px2d(n,m)*sinU + ...
160             Py2d(n,m)*sinV));% BP array calculation.
161     end
162 end

```

III.2 CONVEX OPTIMIZATION METHOD

```

1 %%
2 % Program: Hologram_Generation.m;
3 % Type: Script;
4 % Function: Calculate the hologram to create the array factor with one beam;
5 % Author: Matheus Pereira Santana.
6
7 %%
8 clear all;
9 close all;
10 clc;
11
12 %%
13 % Variables
14
15 N = 16; % Number of elements in X-axis.
16 M = 16; % Number of elements in Y-axis.
17 f = 12e9; % Frequency.
18 c = 3e8; % Light velocity.
19 lambda = c/f; % Free-space wavelength.
20 er = 4.5; % Dielectric constant of the medium.
21 lambda_g = lambda/sqrt(er); % Guided wavelength.
22 dx = lambda_g/2; % Inter-space elements in X-axis.
23 dy = lambda_g/2; % Inter-space elements in Y-axis.
24
25 %%

```

```

26 % Antenna position
27
28 Px = -(N-1)/2:1:(N-1)/2; % Position index in X-axis.
29 Py = -(-(M-1)/2:1:(M-1)/2); % Position index in Y-axis.
30 Px2d = dx*meshgrid(Px); % Array of positions.
31 Py2d = dy*meshgrid(Py)'; % Array of positions.
32
33 %%
34 % Space Coordinates
35
36 theta0 = 0:pi/36:pi; % Elevation
37 phi0 = 0:pi/18:2*pi; % Azimuth
38 [phi,theta] = meshgrid(phi0,theta0); % Coordinate mesh.
39 sinU = sin(theta).*cos(phi); % U-sine space.
40 sinV = sin(theta).*sin(phi); % V-sine space.
41 Ux = reshape(kron(Px3d(:),sinU)',length(theta),length(phi),length(Px3d(:))); % ...
    Reshape(X*sinU)
42 Vy = reshape(kron(Py3d(:),sinV)',length(theta),length(phi),length(Py3d(:))); % ...
    Reshape(Y*sinV)
43
44 %%
45 % Cavity phase
46
47 P_r = sqrt(Px2d.^2+Py2d.^2); % Array of radius.
48 P_phase = atan2d(Py2d,Px2d); % Array of phases.
49
50 Hx = besselh(0,1,(2*pi/lambda_g)*P_r).*cosd(P_phase); % Magnetic field - ...
    X-component - Zero order hankel function of the first kind.
51 Hy = besselh(0,1,(2*pi/lambda_g)*P_r).*sind(P_phase); % Magnetic field - ...
    Y-component - Zero order hankel function of the first kind.
52
53 %%
54 % Excitation array
55
56 theta_p = 20; % Desired elevation direction.
57 phi_p = 60; % Desired Azimuth direction.
58
59 S_w = ones(N,M); % Amplitude array.
60 S_phase = ((2*pi/lambda)*Px2d*sind(theta_p)*cosd(phi_p) + ...
    (2*pi/lambda)*Py2d*sind(theta_p)*sind(phi_p)); % Phase array.
61
62 S = S_w.*exp(-1i*S_phase); % Excitation array.
63
64 %%
65 % Hologram calculation - Array pattern synthesis
66
67 phase_threshold = 90; % Phase threshold.
68
69 Hologram_phase = 180*S_phase/pi+180*angle(Hy)/pi; % Hologram phase recording.
70 Hologram = zeros(N,M); % Hologram array
71
72 n_ant = 0;

```

```

73
74 for n = 1:1:N
75     for m = 1:1:M
76         if abs(Hologram_phase(n,m)) ≤ phase_threshold % Appliaing phase threshold.
77             Hologram(n,m) = 1; % Hologram recording.
78             n_ant = n_ant+1;
79         else
80             continue;
81         end
82     end
83 end
84
85
86
87 S1d = reshape(S(:,1,1,length(S(:))),length(S(:))); % Reshape(S) - 1D.
88 af = sum(S1d.*exp((1i*2*pi/lambda)*(Ux+Vy)),3)'; % Array factor.
89
90
91 Sreal = Holo.*exp(1i*angle(Hy)); % Hologram excitation.
92 Sreal1d = reshape(Sreal(:,1,1,length(Sreal(:))),length(Sreal(:))); % Reshape(Sreal) - 1D.
93 af_r = sum(Sreal1d.*exp((1i*2*pi/lambda)*(Ux+Vy)),3)'; % Hologram array factor.
94
95 %%
96 % Convex Optimization
97
98 theta_x = theta_p; % Desired direction
99 phi_x = phi_p; % Desired direction
100 gamma = 5; % Poiting direction margin
101 Δ = 30; % Gap between the beam direction and the sidelobe region
102
103 % Elevation points:
104
105 theta_0 = (pi/180)*linspace(theta_x-gamma,theta_x+gamma,5); % At the desired ...
    direction
106 theta_l = (pi/180)*linspace(0,90,45); % Under the desired azimuth
107 theta_u = (pi/180)*linspace(0,90,45); % Above the desired azimuth
108 theta_i = (pi/180)*linspace(theta_x+2*gamma,90,45); % Above the desired elevation
109
110 phi_0 = (pi/180)*linspace(phi_x-gamma,phi_x+gamma,5); % At the desired direction
111 phi_l = (pi/180)*linspace(0,phi_x-Δ,60); % Under the desired azimuth
112 phi_u = (pi/180)*linspace(phi_x+Δ,360,60); % Above the desired azimuth
113 phi_i = (pi/180)*linspace(phi_x-Δ,phi_x+Δ,20); % Second margin
114
115 % Meshgrids
116
117 [phi_grid_0,theta_grid_0] = meshgrid(phi_0,theta_0);
118 [phi_grid_l,theta_grid_l] = meshgrid(phi_l,theta_l);
119 [phi_grid_u,theta_grid_u] = meshgrid(phi_u,theta_u);
120 [phi_grid_i,theta_grid_i] = meshgrid(phi_i,theta_i);
121
122 sinU_0 = sin(theta_grid_0).*cos(phi_grid_0); % U-sine space.
123 sinV_0 = sin(theta_grid_0).*sin(phi_grid_0); % V-sine space.

```

```

124 sinU_l = sin(theta_grid_l).*cos(phi_grid_l); % U-sine space.
125 sinV_l = sin(theta_grid_l).*sin(phi_grid_l); % V-sine space.
126 sinU_u = sin(theta_grid_u).*cos(phi_grid_u); % U-sine space.
127 sinV_u = sin(theta_grid_u).*sin(phi_grid_u); % V-sine space.
128 sinU_i = sin(theta_grid_i).*cos(phi_grid_i); % U-sine space.
129 sinV_i = sin(theta_grid_i).*sin(phi_grid_i); % V-sine space.
130
131 %%
132 % Array factors
133
134 U_0 = ...
    reshape(kron(Px3d(:), sinU_0)', length(theta_0), length(phi_0), length(Px3d(:))); ...
    % Reshape(X*sinU).
135 V_0 = ...
    reshape(kron(Py3d(:), sinV_0)', length(theta_0), length(phi_0), length(Py3d(:))); ...
    % Reshape(Y*sinV).
136 exp_0 = exp((1i*2*pi/lambda)*(U_0+V_0));
137 U_l = ...
    reshape(kron(Px3d(:), sinU_l)', length(theta_l), length(phi_l), length(Px3d(:))); ...
    % Reshape(X*sinU).
138 V_l = ...
    reshape(kron(Py3d(:), sinV_l)', length(theta_l), length(phi_l), length(Py3d(:))); ...
    % Reshape(Y*sinV).
139 exp_l = exp((1i*2*pi/lambda)*(U_l+V_l));
140 U_u = ...
    reshape(kron(Px3d(:), sinU_u)', length(theta_u), length(phi_u), length(Px3d(:))); ...
    % Reshape(X*sinU).
141 V_u = ...
    reshape(kron(Py3d(:), sinV_u)', length(theta_u), length(phi_u), length(Py3d(:))); ...
    % Reshape(Y*sinV).
142 exp_u = exp((1i*2*pi/lambda)*(U_u+V_u));
143 U_i = ...
    reshape(kron(Px3d(:), sinU_i)', length(theta_i), length(phi_i), length(Px3d(:))); ...
    % Reshape(X*sinU).
144 V_i = ...
    reshape(kron(Py3d(:), sinV_i)', length(theta_i), length(phi_i), length(Py3d(:))); ...
    % Reshape(Y*sinV).
145 exp_i = exp((1i*2*pi/lambda)*(U_i+V_i));
146
147 Hy1d = reshape(Hy(:), 1, 1, length(Hy(:))); % Reshape(Hy) - 1d.
148
149
150
151
152 epsilon = 10;
153 lim_dB_u = max(max(10*log10(abs(af_r))))-10;
154 lim_u = 10^(lim_dB_u/10);
155 lim_dB_l = max(max(10*log10(abs(af_r))))-10;
156 lim_l = 10^(lim_dB_l/10);
157 lim_0_db = max(max(10*log10(abs(af_r)))));
158 lim_0 = 10^(lim_0_db/10);
159 lim_dB_i = max(max(10*log10(abs(af_r))))-10;

```

```

160 lim_i = 10^(lim_dB_i/10);
161
162 cvx_begin
163     variable x(N,M) nonnegative
164     xcvx = Holo+abs(Holo-1).*x;
165     %xcvx = x;
166     %minimize (norm(xcvx,1)+1000*M*N*norm(xcvx-0.5,inf))
167     minimize (norm(xcvx,1)+N*M*norm(xcvx-0.5,inf))
168     subject to
169         abs(sum(a_u.*repmat(reshape(xcvx(:),1,1,length(xcvx(:))),length(theta_u),
170             length(phi_u)),3)) <= lim_u
171         abs(sum(a_l.*repmat(reshape(xcvx(:),1,1,length(xcvx(:))),length(theta_l),
172             length(phi_l)),3)) <= lim_l
173         abs(sum(a_i.*repmat(reshape(xcvx(:),1,1,length(xcvx(:))),length(theta_i),
174             length(phi_i)),3)) <= lim_i
175         abs(sum(a_0.*repmat(reshape(xcvx(:),1,1,length(xcvx(:))),length(theta_0),
176             length(phi_0)),3)-lim_0) <= epsilon
177 cvx_end
178
179 Scvx = xcvx.*exp(1i*angle(Hy)); %Convex excitation array.
180 x3dcvx = reshape(Scvx(:),1,1,length(Scvx(:))); % Reshape(Scvx) - 1D.
181 afcvx = sum(x3dcvx.*exp((1i*2*pi/lambda)*(Ux+Vy)),3)'; % Array factor of the ...
    convex optimization.
182
183 x_round = abs(round(xcvx));
184 max_x = max(max(abs(round(xcvx))));
185 min_x = min(min(abs(round(xcvx))));
186 x_round(x_round>2) = 1;
187 Scvx_r = abs(round(x_round)).*exp(1i*angle(Hy)); % Rounded convex excitation ...
    array.
188 x3dcvx_r = reshape(Scvx_r(:),1,1,length(Scvx_r(:))); % Reshape(Scvx_r).
189 afcvx_r = sum(x3dcvx_r.*exp((1i*2*pi/lambda)*(Ux+Vy)),3)'; % Rounded convex ...
    excitation array factor.

```